JPL PUBLICATION 83-56

Evaluation of Thermal Data for Geologic Applications

Anne B. Kahle
Frank Don Palluconi
Catherine J. LeVine
Michael J. Abrams
David B. Nash
Ronald E. Alley
John P. Schieldge

(NASA-CR-173211) EVALUATION OF THERMAL DATA FOR GEOLOGIC APPLICATIONS (Jet Propulsion Lab.) 115 p HC A06/MF A01 CSCL 08G
N84-16703
Unclas
G3/46 18205

December 1982

National Aeronautics and
Space Administration

Jet Propulsion Laboratory
California Institute of Technology
Pasadena, California

JPL PUBLICATION 83-56

Evaluation of Thermal Data for Geologic Applications

Anne B. Kahle
Frank Don Palluconi
Catherine J. LeVine
Michael J. Abrams
David B. Nash
Ronald E. Alley
John P. Schieldge

ORIGINAL CONTAINS
COLOR ILLUSTRATIONS

December 1982

NASA
National Aeronautics and
Space Administration

Jet Propulsion Laboratory
California Institute of Technology
Pasadena, California

The research described in this publication was carried out by the Jet Propulsion Laboratory, California Institute of Technology, under contract with the National Aeronautics and Space Administration.

ABSTRACT

This study is part of a program at the Jet Propulsion Laboratory to investigate the use of thermal infrared data in geologic remote sensing. The program has concentrated on developing techniques to acquire, process, interpret, and evaluate thermal data, in conjunction with other types of data, for geologic applications. Four locations at three test sites in the western U.S. were studied to determine the utility of aircraft and Heat Capacity Mapping Mission (HCMM) thermal data. The results of this investigation are:

(1) Sensitivity studies using thermal models indicated sources of errors in the determination of thermal inertia from HCMM data. Atmospheric and topographic corrections allowed more realistic calculations of thermal inertia but the cost would be prohibitive in most operational projects. Apparent thermal inertia, with only simple atmospheric radiance corrections to the measured surface temperature, would be sufficient for most operational requirements for surface thermal inertia.

(2) Thermal data does have additional information about the nature of surface material that is not available in visible and near infrared reflectance data. Color composites of daytime temperature, nighttime temperature, and albedo were often more useful than thermal inertia images alone for discrimination of lithologic boundaries. Principal component analyses were useful in increasing the separability of units.

(3) A modeling study, using the annual heating cycle, indicated the feasibility of looking for geologic features buried under as much as a meter of alluvial material. A field study using aircraft thermal data is underway.

(4) The spatial resolution of HCMM data is a major limiting factor in the usefulness of the data for geologic applications. Future thermal infrared satellite sensors should provide spatial resolution comparable to that of the Landsat data.

(5) Thermal infrared data adds a new dimension to geologic remote sensing and future satellite missions should be undertaken to allow the continued development of these data for geologic applications.

TABLE OF CONTENTS

FIGURES

PAGE iv INTENTIONALLY BLANK

PRECEDING PAGE BLANK NOT FILMED

TABLES

I. INTRODUCTION

For the past six years, a program has been underway at the Jet Propulsion Laboratory (JPL) to study the use of thermal infrared data in geologic remote sensing. The program has concentrated on developing techniques to acquire, process, interpret, and evaluate thermal data, as well as other types of supporting data, for geologic applications. Some of the elements of this program are: (1) a thermal model which describes heat transfer in geologic materials (Kahle, 1977) and which, for a given set of initial and boundary conditions, is used to compute the thermal inertia (TI) of these materials (Gillespie and Kahle, 1977); (2) development of a coupled soil moisture and thermal model (Schieldge et al., 1982); (3) development of a technique to correct TI images for topographic effects; (4) construction of the first TI images derived from albedo, day-night temperature, and topographic and meteorological data (Kahle et al., 1976); (5) acquisition of numerous data sets of thermal and visible data obtained during aircraft flights, and acquisition of digital Heat Capacity Mapping Mission (HCMM) data sets for nine clear day-night periods; (6) acquisition of meteorological observations concurrent with aircraft and HCMM overflights and also concurrent upper air (rawinsonde) data for HCMM overflights; (7) evaluation of all aircraft data sets and the construction of thermal images from the best sets of data; (8) construction from HCMM data of two sets of digital TI images--TI calculated from the JPL thermal model and apparent TI--for all nine data sets, and co-registration of all HCMM data sets, with and without topographic corrections; (9) preliminary geologic interpretation of the aircraft and HCMM TI images (Kahle et al., 1981).

The aircraft and HCMM data are measurements of visible and thermal infrared radiation received by onboard sensors. A total of 19 flights by NASA aircraft were made from March 1975 to April 1979 over four locations at three sites:

Goldfield and Ralston in the Walker Lane area of Nevada; Pisgah Crater in the Mojave Desert, California; and Death Valley, in eastern California. HCMM digital data have been obtained for nine overpass sets from May 1978 to April 1979 for all three areas. Each of these sets includes a night overpass (N), 24 hours later another night overpass, 12 hours later a day overpass (D), and 24 hours later another day overpass. Each NNDD set covers most of all three test sites. Included in this data set is one completely cloud-free nine-day period between July 15 and July 23, 1978, when field measurements were taken during the entire period and two HCMM NNDD overpass sets (eight overpasses) were obtained.

Ground truth data were collected concurrently with most of the aircraft flights and satellite overpasses in order to provide initial and boundary conditions for the thermal models, and to provide verification of results. These data consist of surface measurements of rock and soil temperatures, and vertical profiles of soil temperature and moisture measurements, all obtained at a number of different locations at each test site. Also, meteorological data consisting of in situ measurements of wind speed, dry-bulb air temperature, and wet-bulb air temperature were obtained at seven levels over an eight-meter altitude range by the JPL portable micro-meteorological system. Radiative flux densities (net as well as longwave and shortwave components) and soil heat flux densities near the surface were measured and recorded with standard, commercial instruments located near the micro-meteorological system. Surface weather data were also obtained from National Weather Service stations in the vicinity of the test sites.

The remote sensing and ground-truth data were used in the JPL thermal model as elements of a digital algorithm to compute TI values. All the aircraft and HCMM data sets were evaluated to ensure a sufficiently good ensemble of data to produce a set of high quality TI images suitable for analysis. Excessively noisy thermal or albedo data were discarded. The daytime thermal, nighttime thermal, and albedo data sets were co-registered before they were used in the model: once without topographic corrections, and in the case of the HCMM data, again with the corrections included. Topographic information (for slope azimuth and gradient), in the form of digitized values from Defense Mapping Agency (DMA) data, was added to the processing in the latter case. Initial results showed that the mismatch in resolution between the HCMM data (~500 m IFOV) and the DMA data (~60 m IFOV) reduced the effectiveness of such corrections (see Section II). Digital TI images were generated from all data sets. Finally, the HCMM data sets were also used to calculate and produce apparent TI images to compare with the TI products obtained from the more complex modeling process. These apparent TI images were constructed simply by computing the day-night temperature difference, inverting the value, and multiplying it by the value of one minus the albedo $[(1-A)/\Delta T]$.

In the previous study (Kahle et al., 1981), only a limited time was available for geologic interpretation of the TI products owing to the delay in availability of HCMM data. The objectives of the current study have been:

(1) Further geologic interpretation of the aircraft and HCMM thermal inertia images.

(2) Calculation of the effects of atmospheric attenuation on the infrared signal received by the HCMM satellite.

(3) Determination of the importance of topographic corrections (both aspect and elevation) in the calculations, and consideration of the effects of sub-pixel size topography.

(4) Additional image processing to determine the optimum computer classification and enhancement techniques for the registered data sets.

In the following section (Section II) we describe the further modeling and quantitative studies undertaken this year, including sensitivity studies of the model using HCMM data sets, the atmospheric corrections derived from the LOWTRAN 5 model, topographic corrections, the variations among the several HCMM data sets as a function of time, the development of a model based on the annual temperature variations, and an evaluation of the problems and potential of the *in situ* Thermal Inertia Meter (TIM).

Section III concentrates on interpretation of the HCMM and aircraft data for geologic applications, including surface hydrology.

The final section (Section IV) discusses our conclusions concerning the utility of aircraft and HCMM thermal data for geologic studies.

II. QUANTITATIVE STUDIES

A numerical model (the JPL thermal model) has been developed over the last several years (Kahle, 1977) in order to better understand the magnitude of the physical processes involved in surface heating, and to enable the quantitative determination of the TI of surface materials based on remotely sensed temperatures. In this section we describe our recent studies with the model and various modifications of the model undertaken to evaluate the potential of HCMM data. These include sensitivity studies with the model, atmospheric corrections applied to the data, a model for understanding the effects of sub-grid-scale (sub-pixel) topography, evaluation of the time dependence of HCMM data, a new model developed explicitly to look for subsurface geologic features using seasonal surface temperature variations, and finally, an evaluation of the instrument constructed to determine *in situ* TI values.

The basic thermal model used for computing day-night temperature differences has been described in detail elsewhere (Kahle, 1977) and will be discussed here only briefly. An explicit finite difference algorithm is used to solve the one-dimensional heat conduction equation,

$$\frac{\partial T}{\partial t} = \kappa \frac{\partial^2 T}{\partial z^2} \qquad (1)$$

where T is temperature, κ is thermal diffusivity, t is time, and z is depth. A one-centimeter vertical grid extends from the surface to a depth of 50 cm, and the temperature at each grid point is recomputed every 20 seconds. The boundary conditions are continuity of heat flux at the surface and constant temperature at the lower boundary. The surface fluxes may include solar radiation (S), longwave sky radiation (R), sensible heat transfer (H), latent heat of evaporation or condensation (L), and heat conduction into and out of the ground (G). The initial soil temperature profile is assumed to be constant and the value is estimated, based on measurements when possible. To minimize the error associated with this estimated profile, the model is initialized approximately twenty-four hours prior to the time period of interest, in this case the first pass of the satellite.

Thermal inertia images are produced as follows (Gillespie and Kahle, 1977). Daytime and nighttime temperature images are made from thermal infrared radiance data acquired with line scanners. The data are rectified to account for such systematic effects as instrument optics, viewing geometry, and platform motion. A similar procedure is followed to produce an albedo image. The images are registered to topographic maps of the region of interest so that a one-to-one correspondence is obtained between recognizable features on the map and the temperature and/or the albedo images. Then, a day-night temperature difference (ΔT) image is made by subtracting the nighttime image values from the daytime values, pixel by pixel. The JPL thermal model is run repeatedly to generate a look-up table of TI values as a function of day-night temperature difference, albedo, topographic information, and surface meteorological conditions as measured at one location in the scene. To produce a TI image, each pixel is assigned a TI value from the look-up table based on the ΔT, albedo, and topographic data (if available) for that pixel. Finally, a TI image--a black and white picture of TI values--is made from this data set.

A. Sensitivity Studies

Sensitivity studies were undertaken with the model in order to determine the magnitude of errors that could be introduced into surface TI values calculated from HCMM data, by errors in the input variables. These input "errors" were chosen to be of the order of magnitude which might be expected in the measurements. Actual error measurements are, in most cases, impossible to make.

Given the way the TI images are generated, two types of errors can be introduced. The first type depends upon measurement errors in the original image variables: day temperature, night temperature, albedo, the topographic slope, and the slope azimuth. The second type of error occurs in the determination of the various elements of the surface heat balance boundary value equation.

In order to compute the heat flux densities (S, R, H, L, and G) for the surface boundary condition, meteorological and geographic data are needed. The date, latitude, albedo, slope, slope azimuth, and surface elevation are used in the computation of the solar radiation, S. R consists of the longwave thermal radiation from both the ground and the sky. The ground is assumed to be a blackbody or a graybody so that the component of R due to surface emission is equal to $\varepsilon\sigma T_g^4$, where σ is the Stefan-Boltzmann constant, ε is emissivity (often assumed for simplicity to be equal to unity which is appropriate for a blackbody), and T_g is the ground temperature. Most soils have emissivities that range between $\varepsilon = 0.84$ and $\varepsilon = 0.95$ (Sellers, 1965). The downward sky radiation component of R is computed from an effective sky temperature using the formulation of Kondratyev (1969). We have used two different methods for the calculation of H and L, an aerodynamic method and a profile method (Kahle et al., 1982). Both require onsite measurements of air speed, temperature, and humidity. G is computed from the model as

$$G = -K \frac{\partial T}{\partial Z} \qquad (2)$$

where K is thermal conductivity.

The sensitivity tests were run with a version of the thermal model in which the effects of latent heat were ignored, using observed data as input to the model. These calculations pertain to test sites at Goldfield, Nevada; Death Valley, California; and Pisgah Crater, California.

The temperature and albedo image data are from the HCMM satellite data acquired predawn and in the afternoon of July 22, 1978. The topographic image data are from National Cartographic Information Center (NCIC) data tapes. Air temperature, windspeed, and the initial subsurface temperature profile were measured at the Goldfield test site. For Pisgah, the wind speed and air temperature values were acquired from the National Weather Service station at Daggett, California, approximately 40 km from the site. The National Park Service rangers provided meteorological data from Furnace Creek in Death Valley, California.

Using these data, TI images were created for the three test sites by the method described earlier. These images are shown in Figures 1-3. Average values of the TI and albedo over each test site were calculated and are given in Table 1. To simplify this study and reduce computing time, these values have not been corrected for atmospheric transmission effects. Such corrections, which have been made for a few cases (see Section IIB), lower the TI values by from 10 to 25%. These corrections should systematically change the image, however, and should not significantly affect this sensitivity study. New perturbed TI images were then generated, using data that had an observed quantity altered by a fixed amount (for example, 1 K was added to each pixel in the temperature difference picture). These changes were chosen to be representative of the size of error which might be typical for any of the input variables. The values in Table 2 represent the root-mean-square (RMS) difference between the original TI image and the various test images.

The technique for introducing these perturbations into the model was straightforward in most cases, being a mere substitution of the new values into the model or table look-up. More complicated procedures were required to simulate the effects of intermittent cloudiness, partial cover by vegetation, and elevation changes. Intermittent cloud cover was simulated by eliminating the direct solar heating for a short period during either the morning or early afternoon phase of the diurnal cycle. During that period, only the diffuse component of radiation incident at the surface was included in the calculation. This simulated a small cumulus cloud covering the sun for a short period, which allowed a brief cooling wave to enter the surface. This approach is necessarily simple since the inclusion of cloud effects in the model is a complex problem in cloud-atmosphere-ground radiative processes that presupposes knowledge of cloud optical properties, amount, type, etc. Moreover, it does not

ORIGINAL PAGE

BLACK AND WHITE PHOTOGRAPH

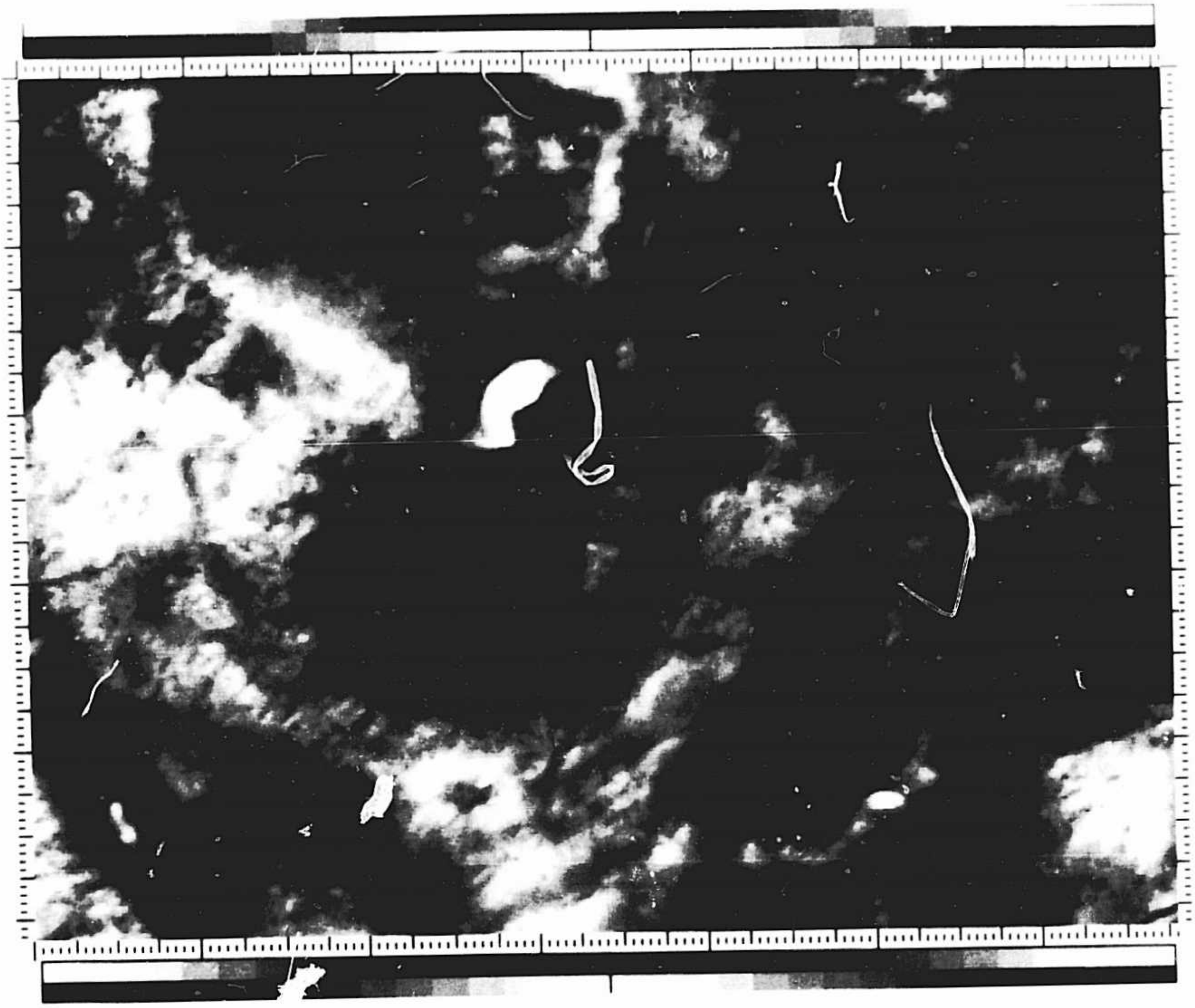

Figure 1. Thermal inertia image of the Goldfield, NV test site, July 22, 1978.

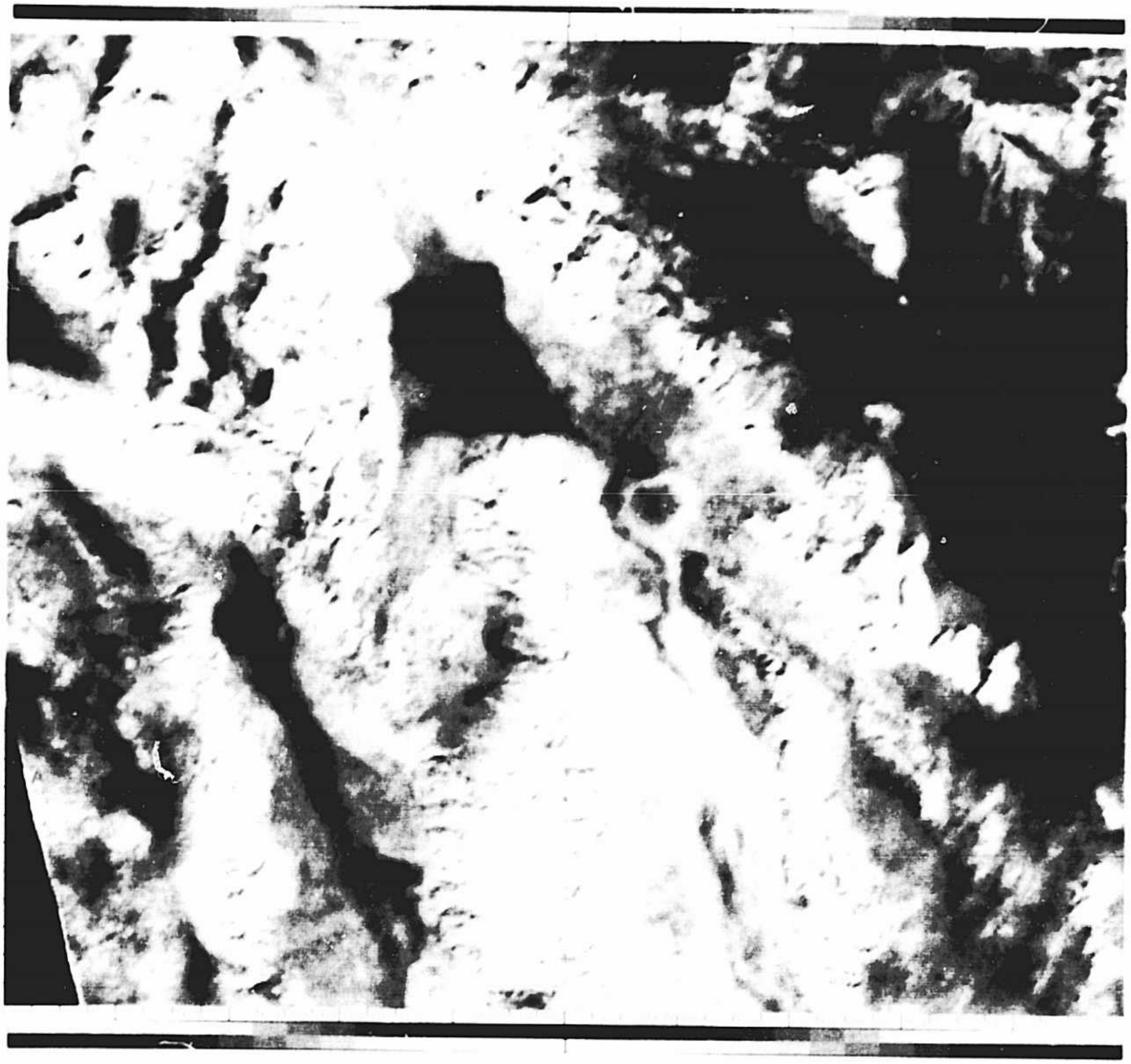

Figure 2. Thermal inertia image of the Death Valley, CA test site, July 22, 1978.

ORIGINAL PAGE
BLACK AND WHITE PHOTOGRAPH

Figure 3. Thermal inertia image of the Pisgah Crater, CA test site, July 22, 1978.

Table 1

Average Values of Thermal Inertia and Albedo from HCMM Data July 22, 1978

	Goldfield	Death Valley	Pisgah Crater
Thermal Inertia ($cal\ cm^{-2}\ sec^{-1/2}\ K^{-1}$)	.0625	.0820	.0727
Albedo (percent)	19.2	18.6	20.1

Table 2

Changes in Thermal Inertia Due to Perturbations in Input Variables, HCMM Data, July 22, 1978

Variable	Perturbation	TI Change, $cal\ cm^{-2} sec^{-1/2}\ K^{-1}$ Goldfield	Death Valley	Pisgah Crater
ΔT	1 K	.0029	.0028	.0027
ΔT	2 K	.0059	.0057	.0056
albedo	2%	.0023	.0023	.0023
slope	4°	.0012	.0015	.0011
slope azimuth	45°	.0020	.0037	.0016
elevation	200m	.0006	.0010	.0005
sky brightness temperature	20 K	.0009	.0016	.0009
sensible heat flux	+20%	.0024	.0014	.0016
solar radiation	-5%	.0034	.0034	.0034
surface emissivity	4%	.0006	.0010	.0008
partial vegetation	20%	.0083	.0071	.0086
partial cloudiness	9-10 a.m.	.0037	.0025	.0037
partial cloudiness	1-1:20 p.m.	.0081	.0085	.0086

include the effect clouds have on the nighttime surface temperature variations, although this influence might be assumed to be roughly the same as the sky radiation term in Table 2. (Sellers, 1965, states that cloud layers do not usually increase the downward sky radiation by more than 25% over the clear sky value if the atmospheric water vapor content remains unchanged.)

Vegetative cover affects the albedo, and also the near-surface microclimate and turbulent heat transfer. However, in our analysis, we have only considered the simple effect of a change in measured surface temperature, by assuming that the temperature of the vegetated area (20% coverage) is equal to that of the air temperature. This assumption is valid in a rough sense in arid and semi-arid regions if the air flow about the vegetation is well-mixed and the air temperature measurements are commensurate with the height of the plant. We have found that in fact the surface temperature of desert shrubs (measured with a Barnes PRT-5 portable, infrared thermometer) is equal to the air temperature at the plant height to within about 1 K. This result pertains to desert surfaces in the Goldfield, Pisgah, and Death Valley areas which have from 0 to 30% vegetative cover.

Modeling of a change in elevation requires changing the sensible heat transfer through the air temperature, air density, and drag calculations, and changing the solar and sky radiance terms. Implementation of these changes is discussed in detail in Section IIB.

As noted above, the initial and boundary conditions--which include factors such as local meteorological conditions, albedo, and topography--are different for each site and therefore the same change in a parameter can produce calculated effects of different size. Nonetheless, the results in Table 2 are typical, and are indicative of the relative strengths of these effects in introducing errors into analysis of thermal data.

From this table, it is apparent that the model is much more sensitive to some errors than others. For all three sites, the largest RMS difference is due to afternoon cloudiness which accounts for changes in mean values of calculated TI of more than 10%. Clouds screen direct solar radiation from the ground, and the shortwave radiative flux density at the ground is reduced by about 60%. However, the amount of solar radiation (direct and diffuse) at the ground depends directly upon the cosine of the sun's zenith angle. Therefore, the effects of clouds are more critical for small zenith angles (noon) than for large (late afternoon or early morning hours). Thus a larger cooling pulse is sent into the surface near noon than at other times of day. In addition there is not much time for the surface temperature to recover from the near-noon cloudiness prior to the HCMM afternoon overpass. Thus cloudiness just before the measurement is much more significant than cloudiness at other times. In fact, Table 2 shows that the effect of morning cloudiness is small and about equivalent to a 5% reduction in solar radiation at the top of the atmosphere.

Plant cover has an effect that rivals cloudiness in size. Our simulation constrains the 20% of surface area covered by plants to have a diurnal temperature variation like the near-surface air. In cloudless desert regions the ground is warmer than the overlying air during the day, and colder at night. This means that the day-night temperature difference is smaller for surfaces with vegetation than for those without. With all other factors equal, the smaller day-night temperature differences will result in greater values of TI. Therefore, the presence of plants increases the calculated TI of an area.

The effect of a change in elevation, while not large for the 200 m change indicated in Table 2, can obviously be much more significant in areas of high relief (see Section IIB and Hummer-Miller, 1981). Examination of TI images of areas with high relief do show large systematic changes with (uncorrected) elevation. However, in addition to the atmospheric effects considered here, there will be related systematic effects such as change of vegetation cover and change of outcrop/alluvium ratios with elevation.

The smallest RMS differences in Table 2 are associated with changes in surface emissivity and sky radiation. Changes in either factor alter the net longwave radiative emission at the ground. A 20 K change in effective sky temperature amounts to nearly a 10% change in the downward longwave radiative flux density from the atmosphere. However, neither factor produces more than about a 2% perturbation in computed TI.

A fairly substantial error (20%) in the sensible heat flux causes only a moderate error (4%) in the thermal inertia. This is fortunate because this is a difficult term to determine accurately (Kahle et al., 1981).

Possible sources of the errors in the input image data (surface temperature, surface albedo, and surface topography), their magnitude and some methods of reducing these errors are discussed in the following sections.

B. Atmospheric Corrections

1. Infrared atmospheric corrections

Aside from instrument calibration (Barnes and Price, 1980) the most important source of error in the measurement of surface temperature from the HCMM scanner is the effect of the atmosphere on the signal received. One of the primary efforts of this study has been to examine the effect of the atmosphere on HCMM TI images. We wanted to relate the day-night temperature differences inferred from the Heat Capacity Mapping Radiometer (HCMR) to the actual differences at the surface. Previously generated TI images have been based on our thermal model which predicts temperature on the earth's surface as a function of thermal inertia, albedo, meteorological conditions, and, optionally, topographic orientation. We have now produced TI images for which the day and night temperatures predicted by the thermal model have been corrected using atmospheric radiances and transmittances computed by the LOWTRAN 5 code developed at the Air Force Geophysics Laboratory (Kneizys et al., 1980).

Two changes to our TI algorithm have been incorporated for this study. The first is an adjustment which takes into account the effects of atmospheric absorption, emission, and scattering. The LOWTRAN model is used to correct each day and night temperature to the value it would have at the satellite in the following way. For each case the surface temperature predicted by the heat conduction algorithm is input to the LOWTRAN model. The upward spectral radiance at the top of the atmosphere is then computed by LOWTRAN. This includes both the emitted radiance of the surface and the upward atmospheric radiance. The blackbody temperature corresponding to the total upward radiance is the corrected temperature. The temperature difference is computed after the corrections to the day and night temperatures, and a look-up table is constructed, giving TI as a function of albedo and the corrected temperature difference. A previous experiment (Kahle et al., 1981) showed that variations in elevation must be considered for the atmospheric correction to be meaningful. This conclusion prompted the second change in the model, the addition of elevation as a parameter. The modified version of the thermal model computes temperature as a function of TI, albedo, meteorological conditions, and elevation. In order to reduce computation time we have omitted the dependence on topographic orientation represented by slope and slope azimuth data. In essence we allowed flat, rather than sloping, pixels to vary in elevation. Model runs for the possible combinations of TI and albedo were repeated at three to five different elevations selected according to the elevation range contained in a given scene. Since the temperature differences for each case were found to vary almost linearly with elevation, linear interpolation was used to expand the look-up table to ten elevations. This allowed increased resolution in elevation without a significant increase in computation time.

Geographical and meteorological data are required for the solution of the heat conduction equation and for the atmospheric correction. In addition to the parameters we normally measure, the atmospheric correction requires specification of the atmospheric profiles for temperature, pressure, moisture content, and ozone density. The moisture profile may be in the form of dew-point temperature, relative humidity, or water vapor density. The user may supply these quantities or may choose standard seasonal profiles provided in the LOWTRAN model. We obtained rawinsonde profiles for temperature, pressure, and dew-point temperature for Mercury, Nevada (which is within 150 km of all three test sites) from the National Climatic Center and selected the LOWTRAN standard ozone density profile for a midlatitude summer atmosphere.

In order to model elevation effects as completely as possible within the chosen framework, we have attempted to account for these effects in the surface temperature calculation as well as in the atmospheric correction. For the boundary conditions to reflect the variations in heat transfer associated with differences in elevation, we needed surface meteorological data for several elevations. Since the field measurements of air temperature were appropriate only for the one elevation at which they were made, we calculated the temperatures appropriate to other elevations as follows. The air temperature $T(x,t)$ was assumed to vary according to the dry adiabatic lapse rate, i.e.,

$$T(x,t) = T_o(t) - \Gamma(x - x_o) \qquad (3)$$

where $T_o(t)$ is the measured reference air temperature at elevation x_o; Γ is the lapse rate, taken to be 0.0098 K/m; t is time and x is elevation. The pressure, computed from this extrapolated temperature using the first law of thermodynamics for adiabatic processes and the equation of state for an ideal gas, is

$$p(x,t) = p_o(t) \quad \frac{T(x,t)}{T_o(t)}^{(c_p/R_a)} \qquad (4)$$

where c_p is the specific heat of dry air at constant pressure and R_a is the gas constant for dry air. The reference pressure $p_o(t)$ is extrapolated from an assumed value of 1000 mbar at sea level using Eqn. 4. The equation of state gives the air density as

$$\rho(x,t) = \rho_o(t) \quad \frac{T(x,t)}{T_o(t)}^{(c_p/R_{a-1})} \qquad (5)$$

where $\rho_o(t)$ is the reference air density at the elevation x_o. Instead of computing this reference density from the measured reference air temperature and the extrapolated reference pressure, we used a constant value for ease of calculation. The extrapolated air temperature and air density are used in the calculation of the sensible heat transfer; the pressure is needed for computing the solar radiation.

Estimating the effects of elevation on the longwave downward sky radiance was less straightforward than for solar radiation and sensible heat. In the original HCMM study the sky radiance was represented, after Kondratyev (1969), as

$$R_K = \sigma\, T_{sky}{}^4 = \sigma(255 + 5 \cos t)^4 \qquad (6)$$

where σ is the Stefan-Boltzmann constant and t is time measured from 1400 local time. T_{sky} represents an effective sky temperature which varies during the day. Because Eqn. 6 is independent of elevation, we examined two empirical formulations that account for changes in height. Brunt (1932) suggested the following expression for nocturnal sky radiation:

$$R_B = \sigma T_g^{\,4} (a+b \sqrt{e}) \tag{7}$$

in which T_g is the surface temperature in K, e is the water vapor pressure in mm Hg, and a and b are empirical constants. We used the values 0.61 and 0.050, respectively, for a and b. A profile for water vapor pressure was calculated from the dew-point temperature profile in the rawinsonde data used for the LOWTRAN atmospheric correction. Swinbank (1963) developed the formula,

$$R_S = \frac{1}{60} (a' \ \sigma T_{air}^{\,4} + b') \tag{8}$$

where T_{air} is the air temperature near the surface, σ is the Stefan-Boltzmann constant in cgs units, and a′ and b′ have the values 0.020 and -0.245, respectively. Because we wanted to retain the diurnal variation in the sky radiance we chose to modify R_K based on the decrease with elevation of R_B and R_S rather than to adopt one of the new formulations. We calculated the sky radiance from both Eqns. 7 and 8 for the altitudes of the rawinsonde observations from 0 to 5 km. Day and night data for two dates, May 14 and July 6, 1978, were used. The variation of R_B and R_S with elevation was assessed by means of a ratio,

$$d = \frac{R_o - R}{R_o} \tag{9}$$

where R_o represents the radiance at a reference level, taken to be sea level, and R the radiance at some elevation Δx, measured in kilometers above the reference level. A linear regression using day and night calculations from the Brunt and Swinbank equations gave the best fit as

$$d = 0.0955 \;\Delta x + 0.1120 \qquad (10)$$

with a correlation coefficient of 0.820. By combining Eqns. 9 and 10, we obtained

$$R = R_o \;(0.8880 - 0.0955 \;\Delta x) \qquad (11)$$

We calculated R_o, the radiance at the reference level, from Eqn. 6. Therefore, the modified sky radiance used in the model was

$$R = \sigma(255 + 5 \cos \;t)^4 \;(0.8880 - 0.955 \;\Delta x) \qquad (12)$$

TI images which included the elevation correction and the LOWTRAN atmospheric correction separately and combined were produced for the July 6, 1978 HCMM overpasses at the Death Valley and Goldfield sites. Figures 4 and 5 show the original TI at the two sites with no elevation or atmospheric radiance corrections. New TI images were calculated for elevation changes only, exclusive of the atmospheric radiance changes, and TI difference pictures were then created. These are shown in Figures 6 and 7. As one would expect, the largest differences are at the highest altitudes. Then TI images were created with both elevation and atmospheric radiance corrections. Difference pictures were created between these TI images and the previous set. These differences,

ORIGINAL PAGE
BLACK AND WHITE PHOTOGRAPH

Figure 4. Thermal inertia image of the Death Valley test site, July 6, 1978, with no elevation or atmospheric radiance corrections.

ORIGINAL PAGE
BLACK AND WHITE PHOTOGRAPH

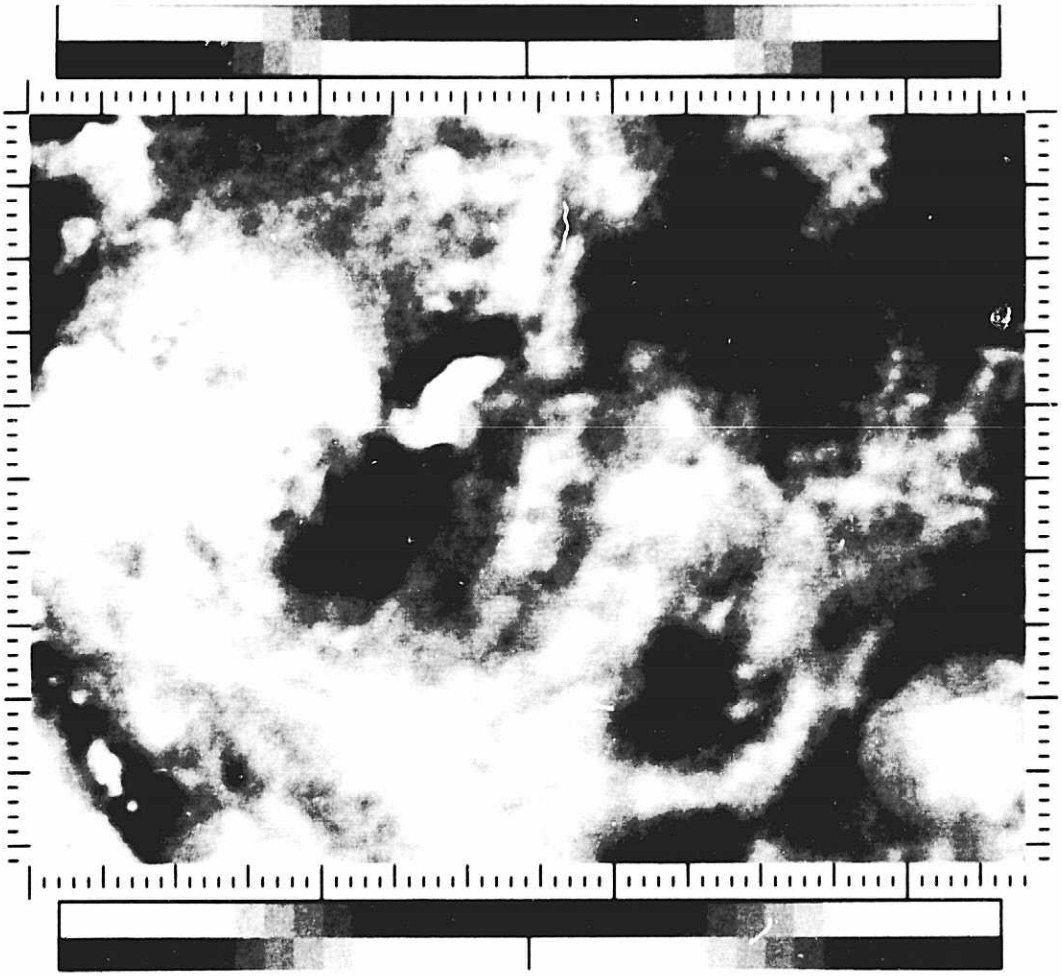

Figure 5. Thermal inertia image of the Goldfield test site, July 6, 1978, with no elevation or atmospheric radiance corrections.

ORIGINAL PAGE
BLACK AND WHITE PHOTOGRAPH

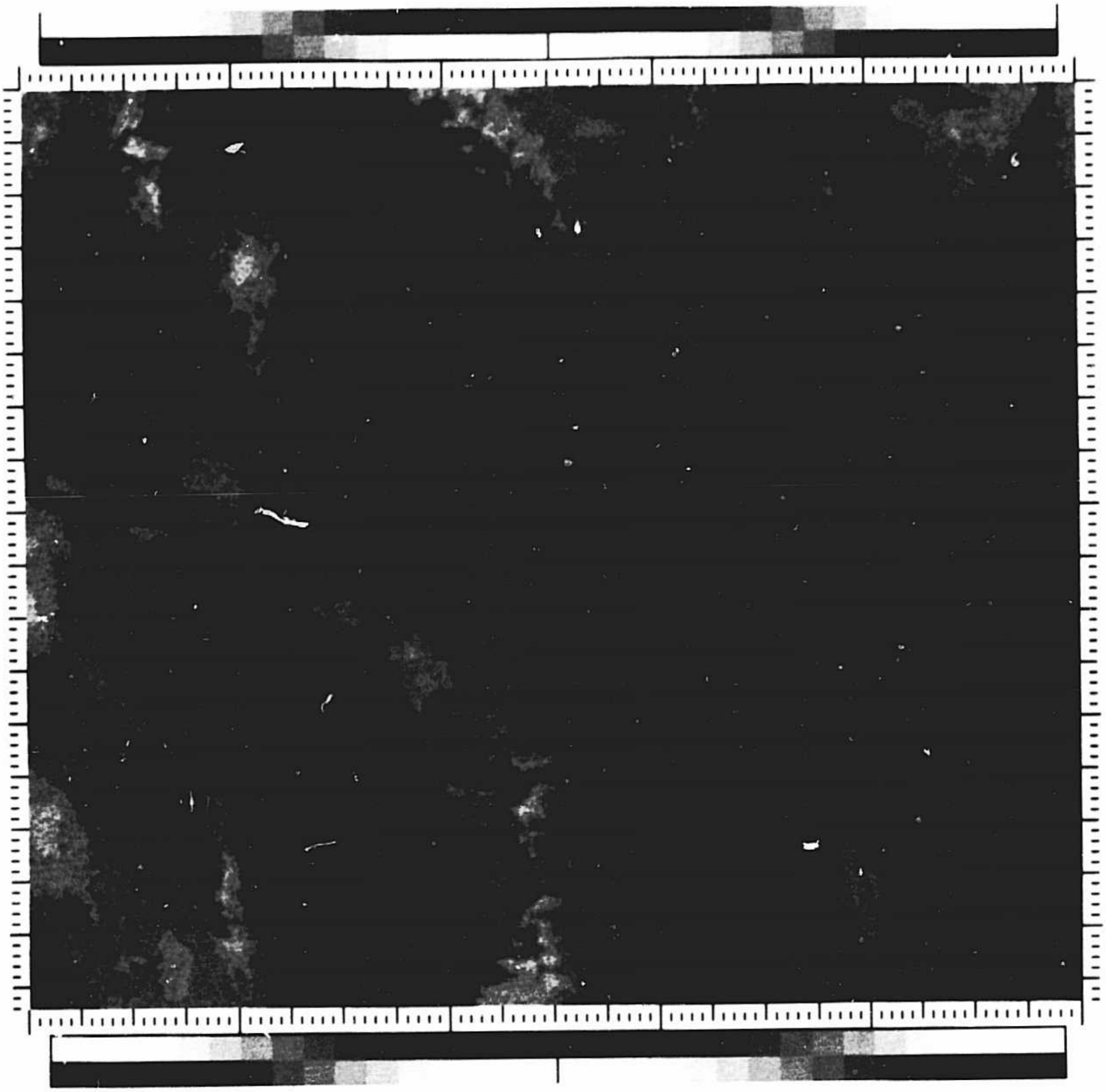

Figure 6. Difference in thermal inertia at the Death Valley test site due to elevation correction.

ORIGINAL PAGE
BLACK AND WHITE PHOTOGRAPH

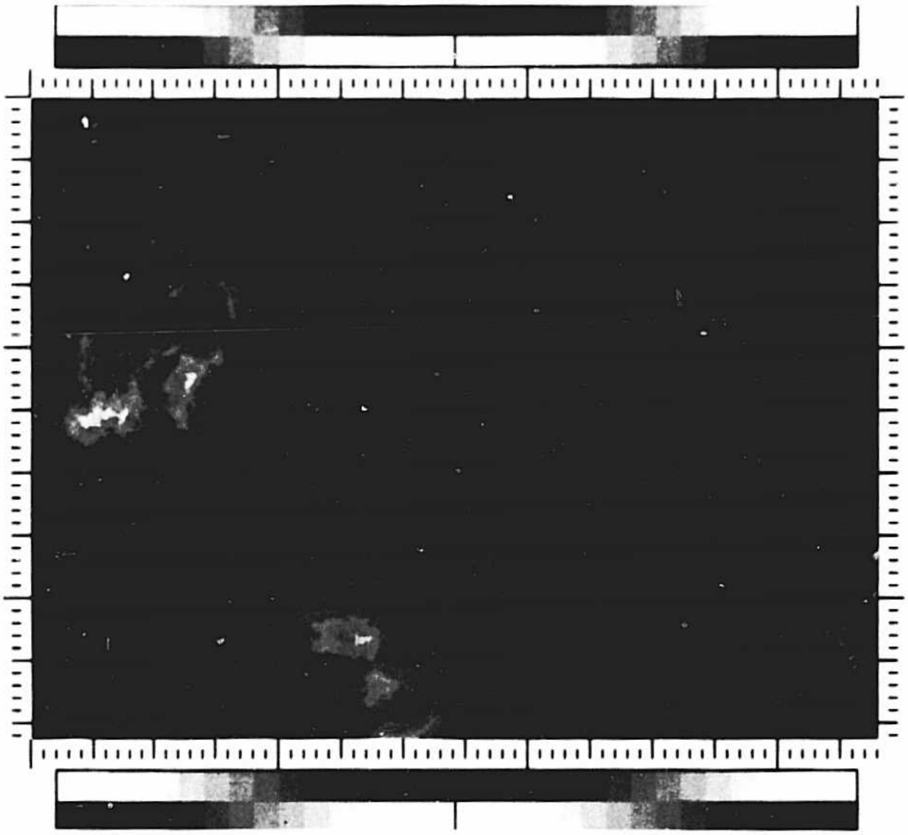

Figure 7. Difference in thermal inertia at the Goldfield test site due to elevation correction.

shown in Figures 8 and 9, illustrate the changes due to the atmospheric radiance corrections alone. Here the change is greatest at the lowest elevation, because the optical path length for radiative propagation is greater here than for higher elevations. Finally, Figures 10 and 11 illustrate the difference between the fully corrected and the original TI images.

Table 3 shows numerical values of TI, with and without the corrections, for selected areas within the images and Table 4 shows the change in TI with the corrections. As predicted from our sensitivity studies, the atmospheric radiance corrections are large, decreasing the value of the TI by 10% or more. The elevation corrections are considerably smaller, but still significant.

The final images in this section, Figures 12 and 13, show the TI images after both atmospheric radiance and elevation corrections. Because all four images have been "stretched", it is not possible to see any significant difference between these and the original uncorrected images (Figures 4 and 5), even though the corrected images represent more nearly correct TI values.
Both of these corrections are costly in computer time and analyst time. As noted earlier, the complete correction, involving slope direction as well as elevation, was deemed too expensive to perform even once for illustrative purposes. It appears that, while these corrections are informative for research purposes, for operational use of thermal data the construction of quantitatively correct TI images is probably not worth the effort and expense involved.

2. Sources of error in surface albedo estimates

The HCMR was provided with a broad visible/near-infrared channel in order to estimate the surface albedo. Since atmospheric gases and aerosols both absorb and scatter sunlight, measurements of the energy emerging at the top of the atmosphere are not direct measurements of surface albedo. In addition,

ORIGINAL PAGE
BLACK AND WHITE PHOTOGRAPH

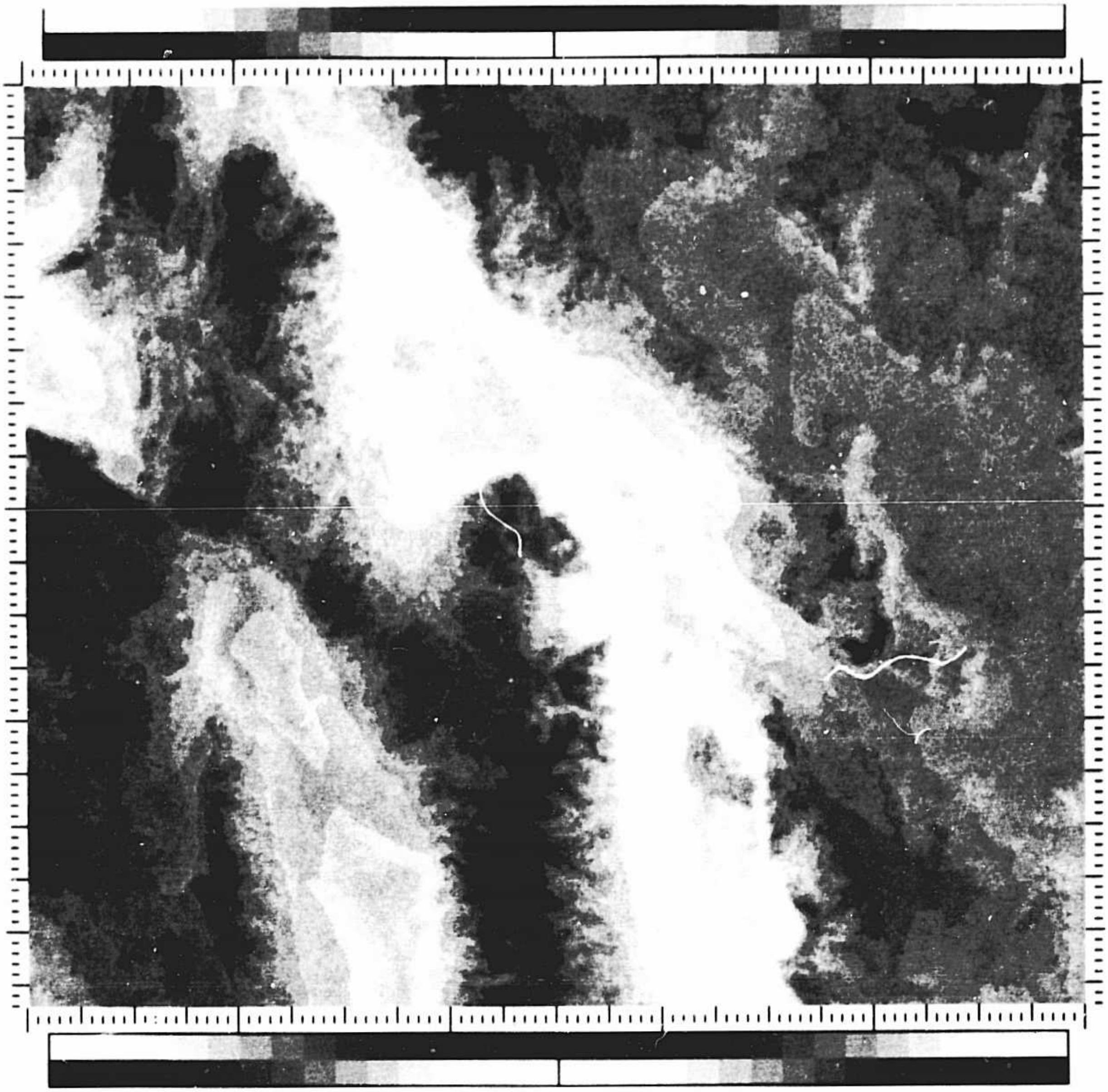

Figure 8. Difference in thermal inertia at the Death Valley test site due to atmospheric radiance correction.

ORIGINAL PAGE
BLACK AND WHITE PHOTOGRAPH

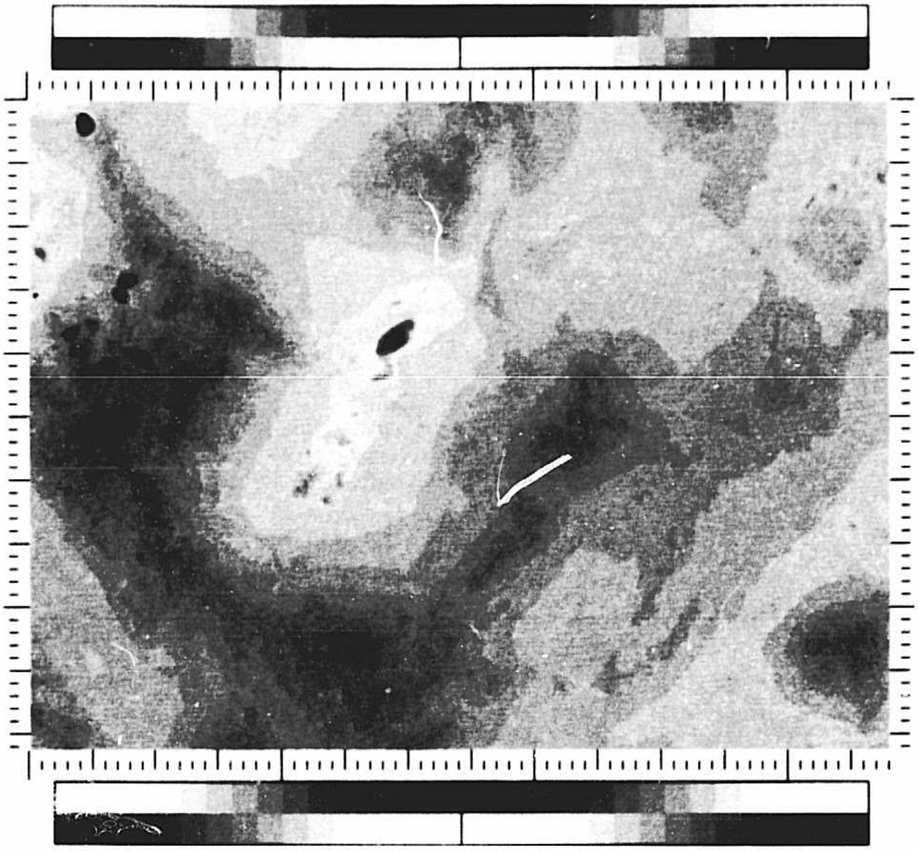

Figure 9. Difference in thermal inertia at the Goldfield test site due to atmospheric radiance correction.

ORIGINAL PAGE
BLACK AND WHITE PHOTOGRAPH

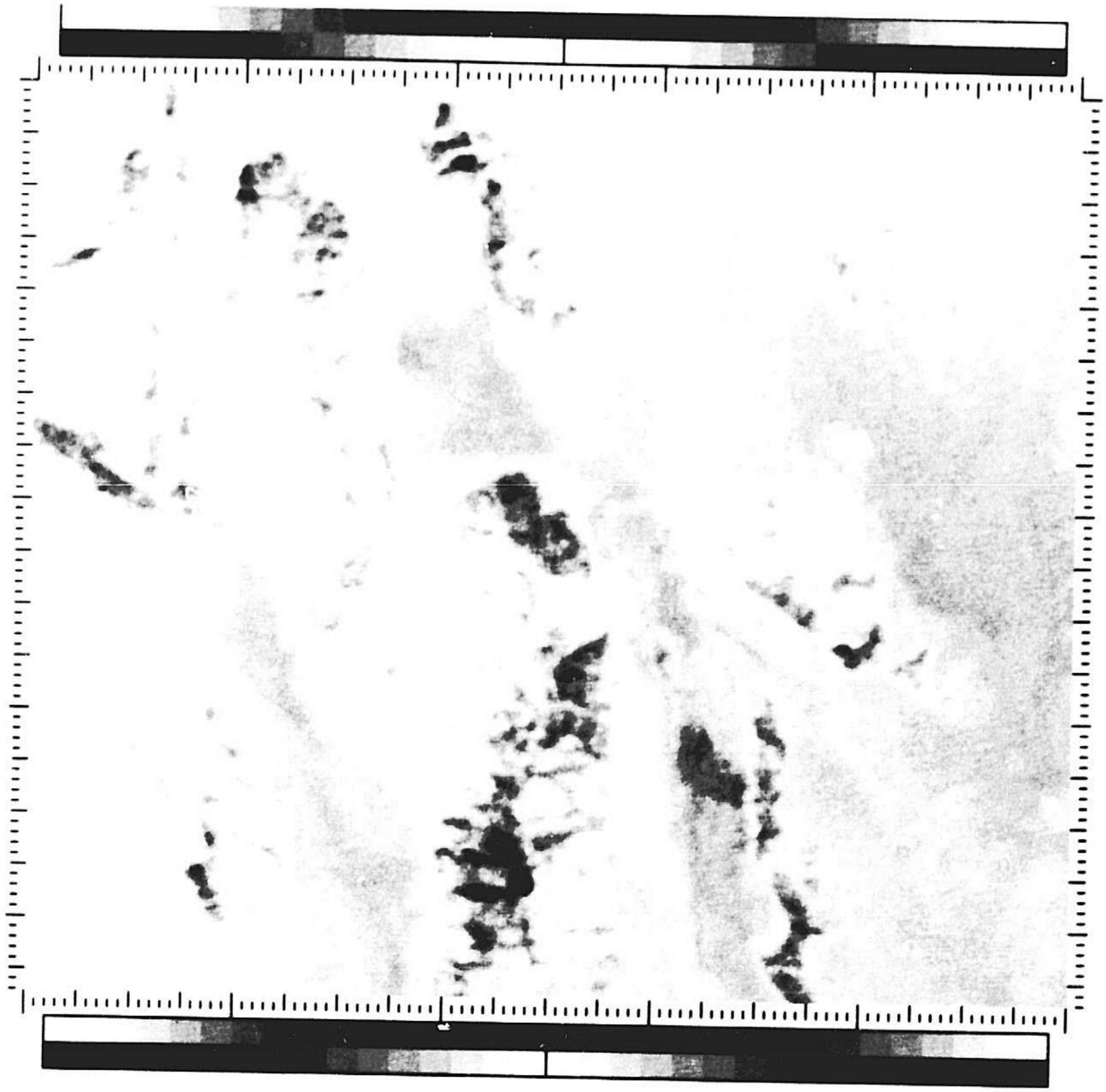

Figure 10. Difference in thermal inertia at the Death Valley test site due to both elevation and atmospheric radiance corrections.

ORIGINAL PAGE
BLACK AND WHITE PHOTOGRAPH

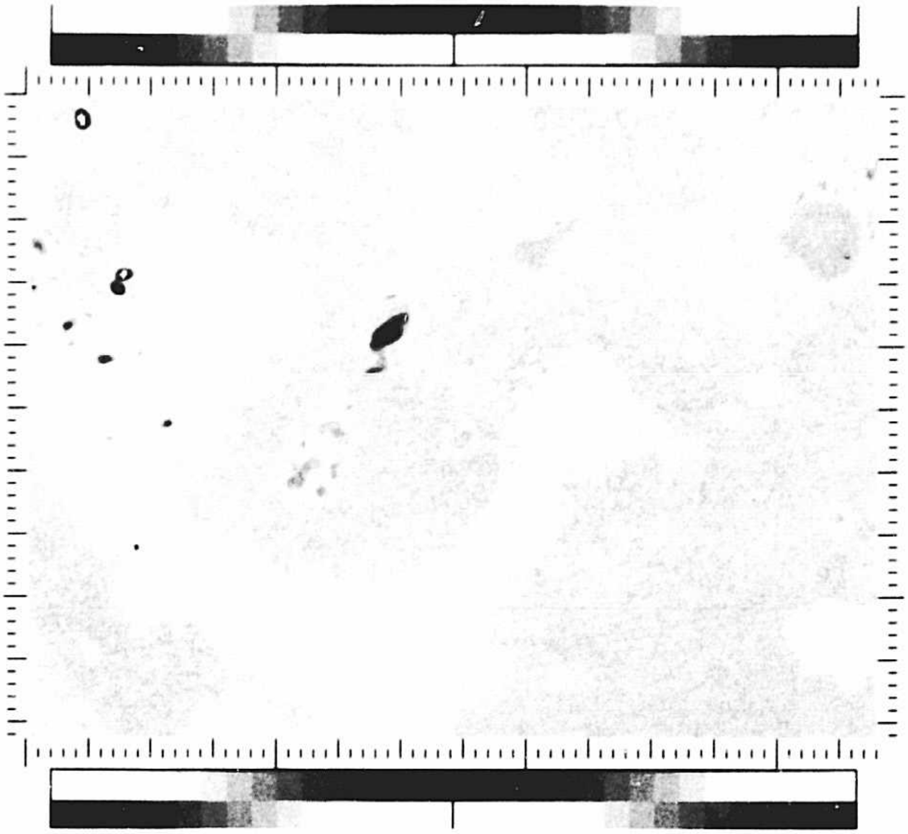

Figure 11. Difference in thermal inertia at the Goldfield test site due to both elevation and atmospheric radiance corrections.

ORIGINAL PAGE
BLACK AND WHITE PHOTOGRAPH

Figure 12. Thermal inertia image of the Death Valley test site after both elevation and atmospheric radiance corrections.

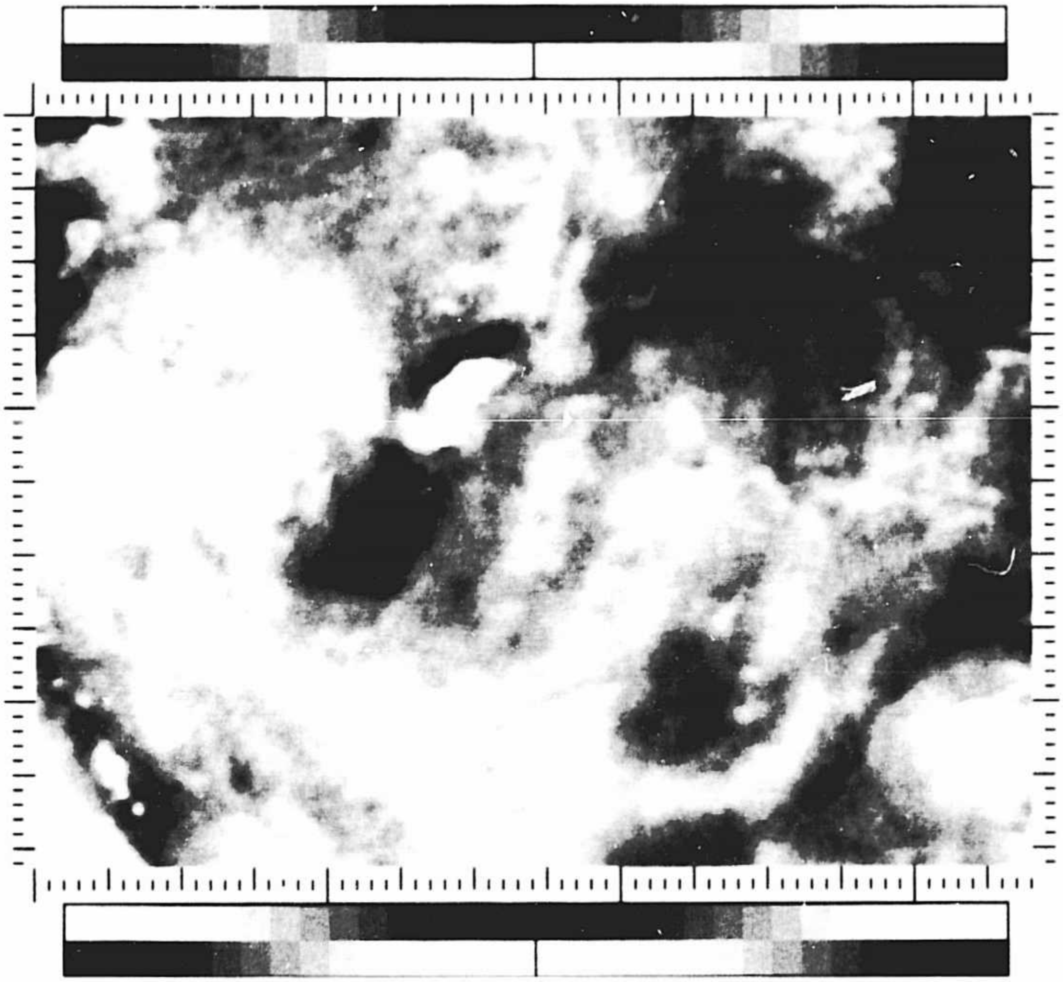

Figure 13. Thermal inertia image of the Goldfield test site after both elevation and atmospheric radiance corrections.

Table 3

Thermal Inertia at Small Test Areas with and without Elevation and Atmosphere Corrections (cal $cm^{-2} sec^{-1/2} K^{-1}$)

	Elev(km)	Uncorrected Mean	Elevation Correction Mean	Elevation and Atmosphere Correction Mean
<u>Death Valley 7-6-78</u>				
Dolomite, Quartz, Limestone	1.06-1.71	.111	.110	.101
Dolomite, Quartz, Limestone	.87-1.58	.113	.110	.102
Quartz Monzonite	1.12-2.01	.111	.107	.101
Alluvium, Pleistocene	.91-1.10	.071	.067	.057
Quaternary Lake Deposits	0	.050	.050	.038
Alluvium, Recent	.34-.67	.083	.081	.068
Sand	.58-.79	.051	.047	.038
Basalt	1.64-2.19	082	0.75	.068
<u>Goldfield 7-6-78</u>				
Playa	1.58	.021	.021	.010
Basalt	1.64-1.83	.031	.029	.019
Silicified Volcanics	1.52	.045	.044	.033
Argillically Altered Volcanics	1.74	.028	.027	.016
Unaltered Volcanics	1.71	.036	.034	.024

Table 4

Differences in Thermal Inertia Caused by Elevation and Atmosphere Corrections (cal $cm^{-2} sec^{-1/2} K^{-1}$)

	Elev(km)	Elevation Effects Mean	LOWTRAN Effects Mean	Overall Effects Mean
Death Valley 7-6-78				
Dolomite, Quartz, Limestone	1.06-1.71	.002	.009	.011
Dolomite, Quartz, Limestone	.87-1.58	.002	.008	.010
Quartz Monzonite	1.12-2.01	.003	.007	.010
Alluvium, Pleistocene	.91-1.10	.005	.010	.014
Quaternary Lake Deposits	0	.000	.012	.012
Alluvium, Recent	.34-.67	.002	.013	.015
Sand	.58-.79	.003	.010	.013
Basalt	1.64-2.19	.008	.007	.015
Goldfield 7-6-78				
Playa	1.58	.001	.011	.011
Basalt	1.64-1.83	.002	.010	.012
Silicified Volcanics	1.52	.001	.011	.012
Argillically Altered Volcanics	1.74	.002	.010	.012
Unaltered Volcanics	1.71	.002	.010	.012

neither the spectral response of the HCMR nor the spectral reflectance of surfaces of interest are gray (response or reflectance independent of wavelength). This introduces additional complexity to the translation of radiance measurements outside the atmosphere into surface albedo. As an example, the HCMR is not sensitive to radiation shorter than 0.5 μm or longer than 1.2 μm. These two wavelength regions contain 44% of the solar energy incident at the top of the atmosphere.

Errors in estimating the surface albedo translate directly into errors in the derived TI, and the size of these errors can be assessed by using the thermal model (as in Table 2). A more detailed relationship between albedo and TI for selected day-night temperature differences (Death Valley, CA, July 22, 1978) is displayed in Figure 14. As an example, if the measured day-night temperature difference is 39.25 K and the surface albedo is 0.30, the nominal value of TI would be 41×10^{-3} cal $\cdot$ cm^{-2} $\cdot$ $sec^{-1/2}$ $\cdot$ K^{-1}. If the albedo, A, is uncertain by 10%, the corresponding uncertainty in TI will be 8%. For a given percentage uncertainty in albedo, the percentage uncertainty in TI will decline with either decreasing albedo or increasing TI from the example given. That is, the relative (percentage) error is largest for bright, low-inertia surfaces and smallest for dark, high-inertia surfaces. When the albedo of a surface is low, most of the available energy is absorbed. Then a large relative error can be made in A with only a small relative error in 1-A.

<u>HCMR Visible/near-infrared channel calibrations</u>. The calibration of the HCMR has been described by Bohse et al. (1979) and Barnes and Price (1980). An integrating sphere, whose radiance could be set to any one of nine known levels, was used. The equivalent albedo was adjusted to account for differences in brightness temperature between this source and the solar spectrum outside the earth's atmosphere. The visible/near-infrared channel had no on-board

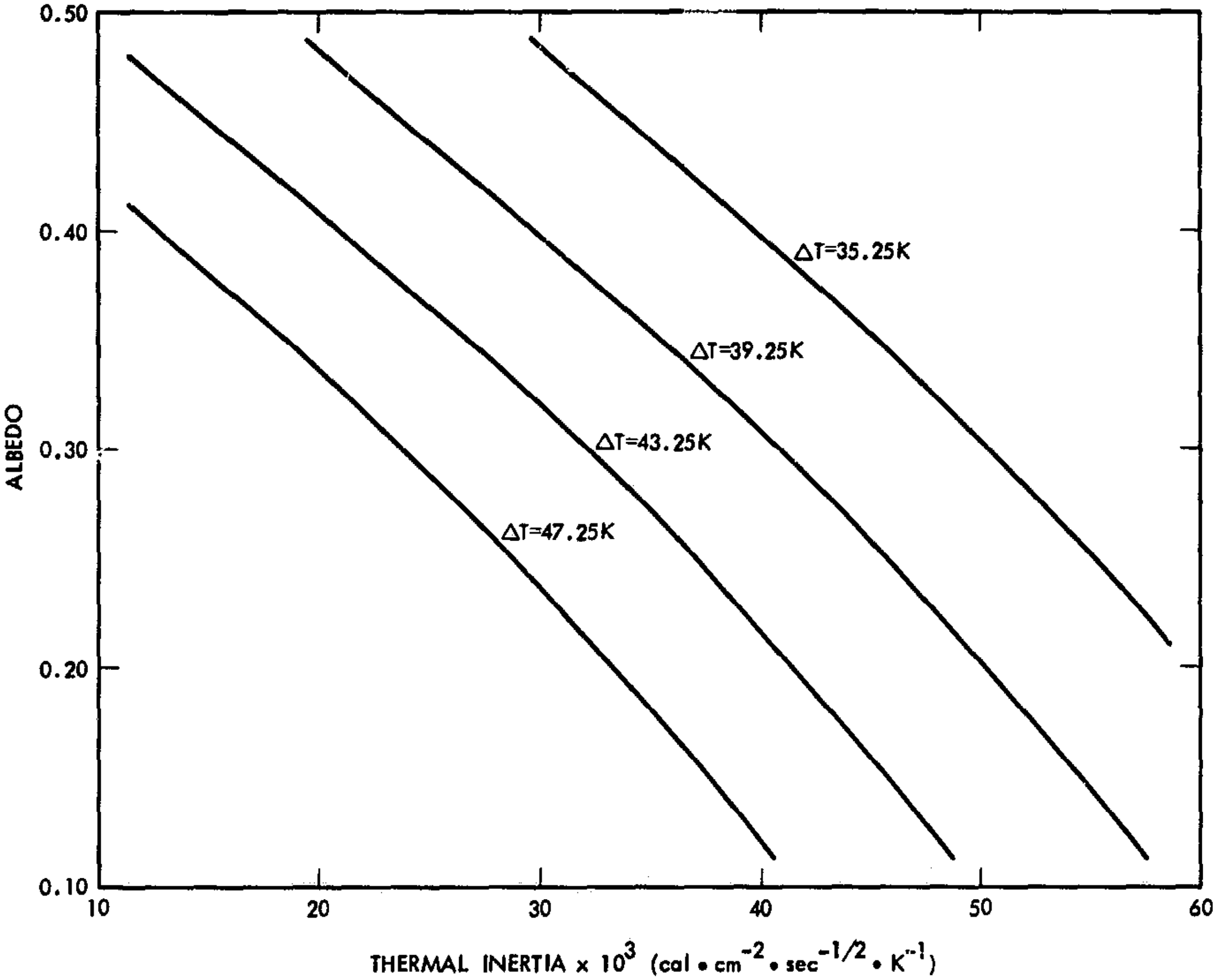

Figure 14. The relationship between albedo and thermal inertia for selected day-night temperature differences, ΔT. This example was developed for Death Valley, CA, July 22, 1978.

calibration system and corrections thus depended entirely on this pre-launch calibration. The post-launch performance never was assessed using surface data. After ground processing, the user of HCMR data is presented with an albedo for each pixel in the daylight scenes which is intended to represent the ratio of the radiance measured to the radiance expected from a perfectly reflecting Lambert surface illuminated by the sun at vertical incidence outside the atmosphere at a distance of 1 A.U. Since in general the sun will not be at zenith nor the earth at 1 A.U. from the sun, it is up to the user to correct for the solar zenith angle and earth-sun distance prior to using the HCMR albedo data.

Sources of error. The following properties of the atmosphere, instrument or surface can lead to errors in albedo measurements.

A. Absorption and scattering by atmospheric gases and aerosols.

B. Non-uniform system response of the HCMR across the solar band.

C. Colored surfaces.

In addition, changes in instrument calibration with time, or non-Lambertian surface reflectance would also be expected to lead to error in making albedo estimates. The approach taken here to look at error sources A, B, and C was to use the known HCMR spectral response (Barnes and Price, 1980), spectra of a light and a dark surface (playa and basalt spectra obtained with the JPL Portable Field Reflectance Spectrometer, PFRS), and an atmospheric model (LOWTRAN 5, Kneizys et al., 1980) to simulate the behavior of the HCMR when viewing the earth's surface through a cloud-free atmosphere. The LOWTRAN code accounts for molecular absorption and scattering and aerosal extinction. It does not account for multiple scattering events, i.e., scattering is treated as a loss mechanism capable only of removing energy from the path independent of the directional characteristics of the scattered radiation. The importance of multiple scattering in increasing the radiation available at the surface will be discussed later. Confining our interest to only the direct and reflected solar component focuses attention on how atmospheric attenuation and the spectral character of the surface and instrument affect estimates of surface albedo.

We first assumed that the surfaces of interest were Lambertian at all wavelengths. Then

$$R(\lambda) = A(\lambda)F(\lambda)/\pi \qquad (13)$$

where $R(\lambda)$ is spectral radiance ($w \cdot m^{-2} \cdot \mu m^{-1} \cdot sr^{-1}$), $A(\lambda)$ is spectral albedo (dimensionless), and $F(\lambda)$ is spectral irradiance on a horizontal surface ($w \cdot m^{-2} \cdot \mu m$). A single number ($A_1$) representing the fraction of energy reflected is given by

$$A_1 = \int_{.3}^{3} A(\lambda)H(\lambda)[\exp(-\tau_1(\lambda)\sec z)]\cos z \, d\lambda \Big/ \int_{.3}^{3} H(\lambda)[\exp(-\tau_1(\lambda)\sec z)]\cos z \, d\lambda \qquad (14)$$

where the limits of integration are given in μm and are intended to cover the range of wavelengths where sunlight is important in heating the surface; $H(\lambda)$ is the solar spectral irradiance outside the earth's atmosphere; the expression $H(\lambda)[\exp(-\tau_1(\lambda)\sec z)]$ is the spectral irradiance available at the bottom of the atmosphere with the sun at zenith angle z; and A_1 is the quantity desired. What is observed and reported can be represented by the following expression:

$$A_m = \frac{\int_{0.5}^{1.2} A(\lambda)H(\lambda)\left[\exp\left(-\tau_1(\lambda)\sec z\right)\right]\left[\exp\left(-\tau_o(\lambda)\right)\right]T(\lambda)\cos z \, d\lambda}{\int_{0.5}^{1.2} H(\lambda)T(\lambda)\cos z \, d\lambda} \qquad (15)$$

where the integration limits are set by the cutoff in system response represented by $T(\lambda)$; and $\exp(-\tau_o(\lambda))$ accounts for the attenuation of the reflected energy when the surface is viewed vertically. The differences in these two expressions result from the non-gray spectral response of the HCMR (shown in Figure 15), the atmospheric attenuation along the path from the surface to instrument, and the normalization which is made with respect to the energy available outside the earth's atmosphere rather than with respect to that available at the surface. Using LOWTRAN 5 with a midlatitude summer atmosphere with the rural-haze model (23-km meteorological range) and a solar zenith angle of 40^o, we evaluated the expressions for A_l and A_m for a perfectly reflecting Lambert surface $\left(A(\lambda) \equiv 1\right.$ for all $\left.\lambda\right)$. In this case $A_l = 1$ as required and $A_m = 0.48$. This reduction is due to atmospheric absorption and molecular and aerosol extinction along the entering path through the atmosphere to the surface (37% reduction) and the exit path from surface to satellite (28% reduction). In the absence of multiple scattering, these atmospheric effects alone would significantly reduce the albedo as measured outside the earth's atmosphere. One would expect from the form of the expression for the measured albedo, A_m, that atmospheric attenuation would have a multiplicative effect; i.e., the reduction of A_m versus A_l would be nearly independent of the value of the albedo itself. This was demonstrated using the reflectance spectra of a dark (basalt) and a bright (playa) surface (Figure 16). The atmospheric model was used to compute A_l and A_m for these surfaces. In order to complete the integral required for A_l beyond the range of reflectance measurements, the value of reflectance at the upper and lower limits were extended shortward to 0.3 μm and longward to 3 μm. The results are as follows: A_l (basalt) = 0.07, A_l (playa) = 0.48; A_m (basalt) = 0.03, A_m (playa) = 0.24. A_m is one half of A_l independent of the surface albedo. This multiplicative property of atmospheric attenuation is unlike what would be expected from a component of atmospheric multiple scattering. With multiple scattering,

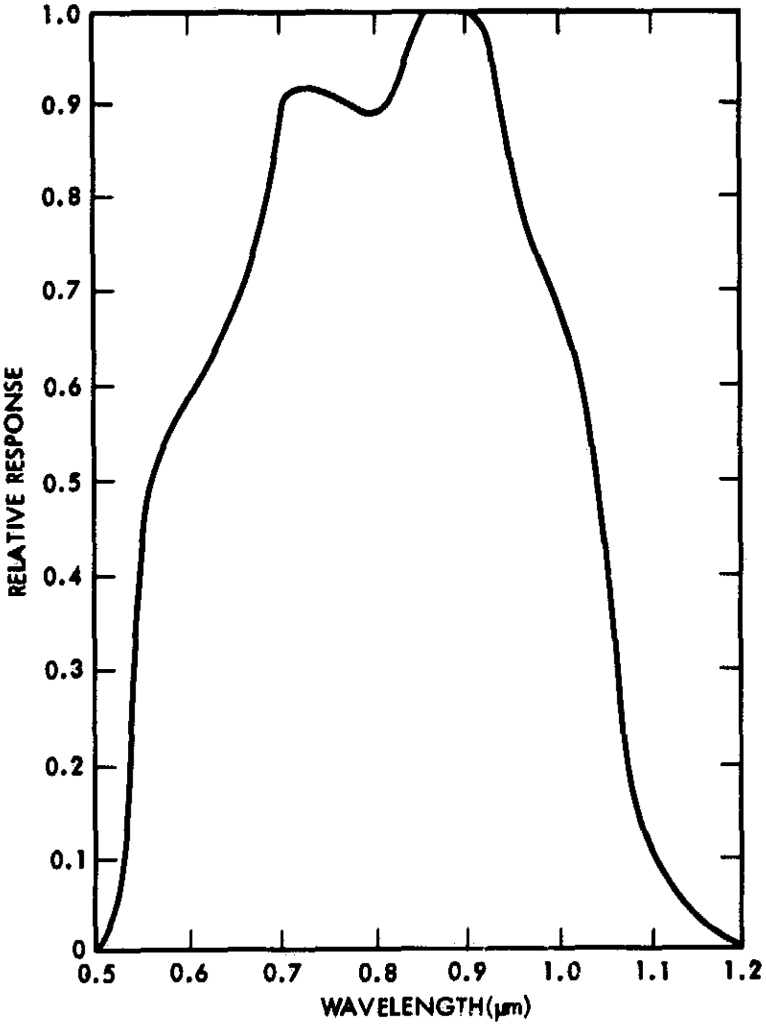

Figure 15. Heat Capacity Mapping Radiometer (HCMR) system spectral response (from Barnes and Price, 1980).

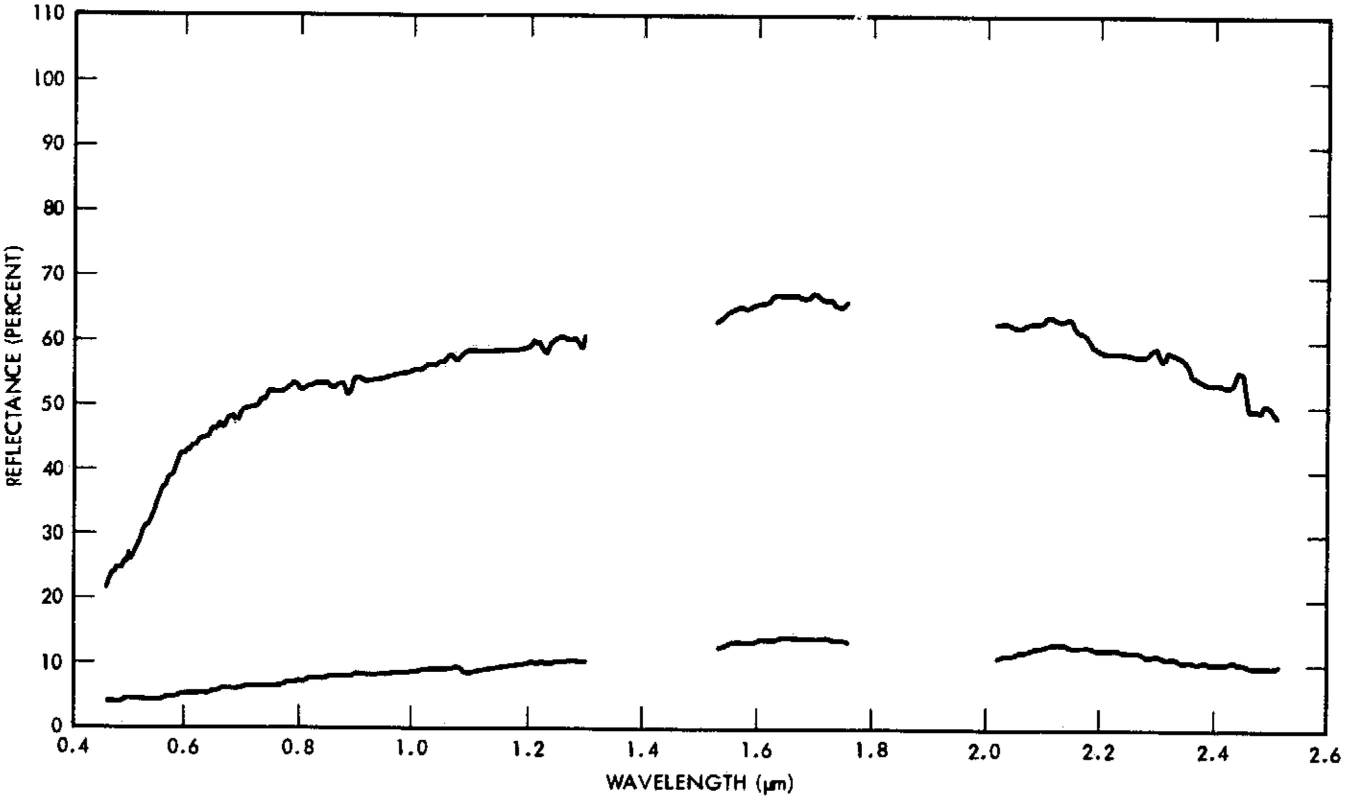

Figure 16. Reflectance spectra obtained with the JPL Portable Field Reflectance Spectrometer (PFRS) for a playa (upper curve) and basalt (lower curve).

some fraction of the photons entering the emergent beam will not have been reflected from the target area. They will add a component to the observed radiance which is independent of the target albedo.

The effect of the non-uniform system response of the HCMR can also be addressed using LOWTRAN. Consider the problem in two parts: First, what is the effect of the variation in system response within the 0.5 - 1.2 μm bandpass of the instrument?; second, how would the results differ if the measurements were made with uniform system response over the full solar band (0.3 - 3 μm)? This involved the computation of A_m, setting $T(\lambda)$ and $A(\lambda) \equiv 1$ for all wavelengths between 0.5 and 1.2 μm in the first case and extending the wavelength range in the second. The results were $A_m = 0.48$ (using the HCMR), $A_m = 0.46$ $\left(T(\lambda) \text{ and } A(\lambda) \equiv 1 \text{ from } 0.5 - 1.2\ \mu\text{m}\right)$ and $A_m = 0.38$ $\left(T(\lambda) \text{ and } A(\lambda) \equiv 1 \text{ from } 0.3 - 3\ \mu\text{m}\right)$. The conclusion is that the non-uniform HCMR system response from 0.5 - 1.2 μm has only a minor effect on the measured albedo compared with atmospheric absorbtion and scattering, and that extending the wavelength response does not improve the albedo estimate since the atmospheric attenuation outside the 0.5 - 1.2 μm band, particularly on the short wavelength side, is greater than the average inside this band.

Since the in-band system response has a minor effect on the derived albedo as shown above, spectral variations in albedo within the system bandwidth would likewise be expected to produce minor effects. An error can result if there is a significant difference between the average albedo inside and outside the bandwidth of the instrument. It is common for many materials to have a decline in reflectivity (albedo) towards shorter wavelengths. This behavior is shown by the materials whose spectral reflectivities are displayed in Figure 16. However, for the two reflectance curves shown, the solar-weighted in-band and out-of-band albedos are very nearly equal so that little error results from sampling in the 0.5 - 1.2 μm band only.

Multiple scattering by atmospheric gases and aerosols can increase the radiance observed, and thus lead to overestimates of the surface albedo. It can do this by: (1) increasing the energy incident on the surface being viewed from directions other than that of the sun (sky light); and (2) by backscattering from the atmosphere to the instrument. Direct solar and global irradiance measurements are commonly made and from these an estimate of the increase in energy available at the surface of the earth due to multiple scattering is possible. Using an example provided by Wolfe and Zissis (1978, pp. 3-39), the excess of global total irradiance over direct solar total irradiance is 7% of the global total irradiance at sea level for an air mass of 1. This percentage increases as path lengths become longer. The contribution from multiple scattering paths into the field of view of the instrument has not been evaluated but they are certainly not negligible.

In summary, through the use of specific examples, a number of sources of error in broadband albedo measurements have been evaluated. The two most important sources of error of those investigated are atmospheric attenuation and multiple scattering. Individually, either effect can be important and they produce errors of opposite sign. The non-uniform system response and limited bandwidth of the HCMR has been shown not to be a significant source of error in albedo measurement. The spectral reflectance character of surfaces outside the HCMR bandpass could lead to albedo errors of either sign, but for the two examples used the error was not found to be significant. An accurate assessment of the corrections necessary to properly account for atmospheric attenuation and scattering requires knowledge of atmospheric properties such as aerosol and water vapor content. These are normally not measured at the same time and for the same locations as the primary remotely sensed image. Because such measurements are difficult and costly to acquire, a more comprehensive treatment of the effects of the atmosphere on broadband albedo measurements would be valuable.

C. Topography

In a previous report Kahle et al. (1981) briefly discussed their method for incorporating ground slope and orientation (aspect) into the calculation of thermal inertia. The method is straightforward when the pixel size of the registered day-night pair of thermal images is the same as the pixel size of the digital topographic "image." It is unclear, however, how to incorporate sub-pixel size topographic features into the calculation of TI. An algorithm for treating such features is presented here along with an assessment of some of the effects that sub-pixel topography has on the calculated TI.

The direct and indirect effects of topography on surface temperature are numerous and complex. For example, even small topographic features may increase or decrease local wind speed and thus modify the latent and sensible heat flux. Topography may promote or obstruct the drainage of surface water and groundwater, increasing or decreasing the latent heat flux. Small topographic features may also be sufficient to cause local advective cooling or heating. Radiative heat flux between neighboring topographic features affects the local ground surface temperature (see Jakosky, 1979). All of these effects are difficult to model. It is, in some cases, difficult even to assess the relative magnitude of these effects. The present discussion is limited to a treatment of the most direct and obvious effect of topography: its influence on the duration and intensity of the insolation flux on the surface of the ground.

Kahle et al. (1981) produced TI images from registered day-night thermal images using an appropriate look-up table describing TI as a function of the day-night temperature difference, ΔT, surface albedo, A, slope azimuth, and slope. If a pixel in the thermal image represents a small enough surface area, it may be adequate to approximate the topography within the pixel area with a flat or inclined plane; however, this approximation probably is not appropriate for the 0.5 km pixel size of HCMR in many areas.

In order to incorporate sub-pixel size topography into TI calculations from HCMM day-night thermal image pairs, a separate look-up table of values of ΔT and A versus TI must be formulated for each pixel. The procedure for creating these tables is as follows:

1) Look-up tables of night (T_N) and day (T_D) surface temperatures versus TI are generated for a smooth plane surface with various surface albedos, slopes, and azimuths using a computer model such as Kahle (1977) and Nash (1983). These tables will be referred to as the first look-up tables.
2) The HCMR filter function (Figure 17) and the Planck function are used to determine the filtered exitance (M) of a blackbody at various temperatures (Figure 18). A look-up table of temperature versus M is formulated. This table will be referred to as the second look-up table.
3) The topography within the pixel is approximated with an assemblage of planar facets with various sizes, azimuths, and slopes.
4) The projected surface area of each facet is measured and used to calculate the proportional area (α_i) of the total pixel area it occupies.
5) The nighttime temperature of each facet within the pixel, T_{N_i} is determined from the first look-up tables using the appropriate slope angle and azimuth and a given value of TI and A.

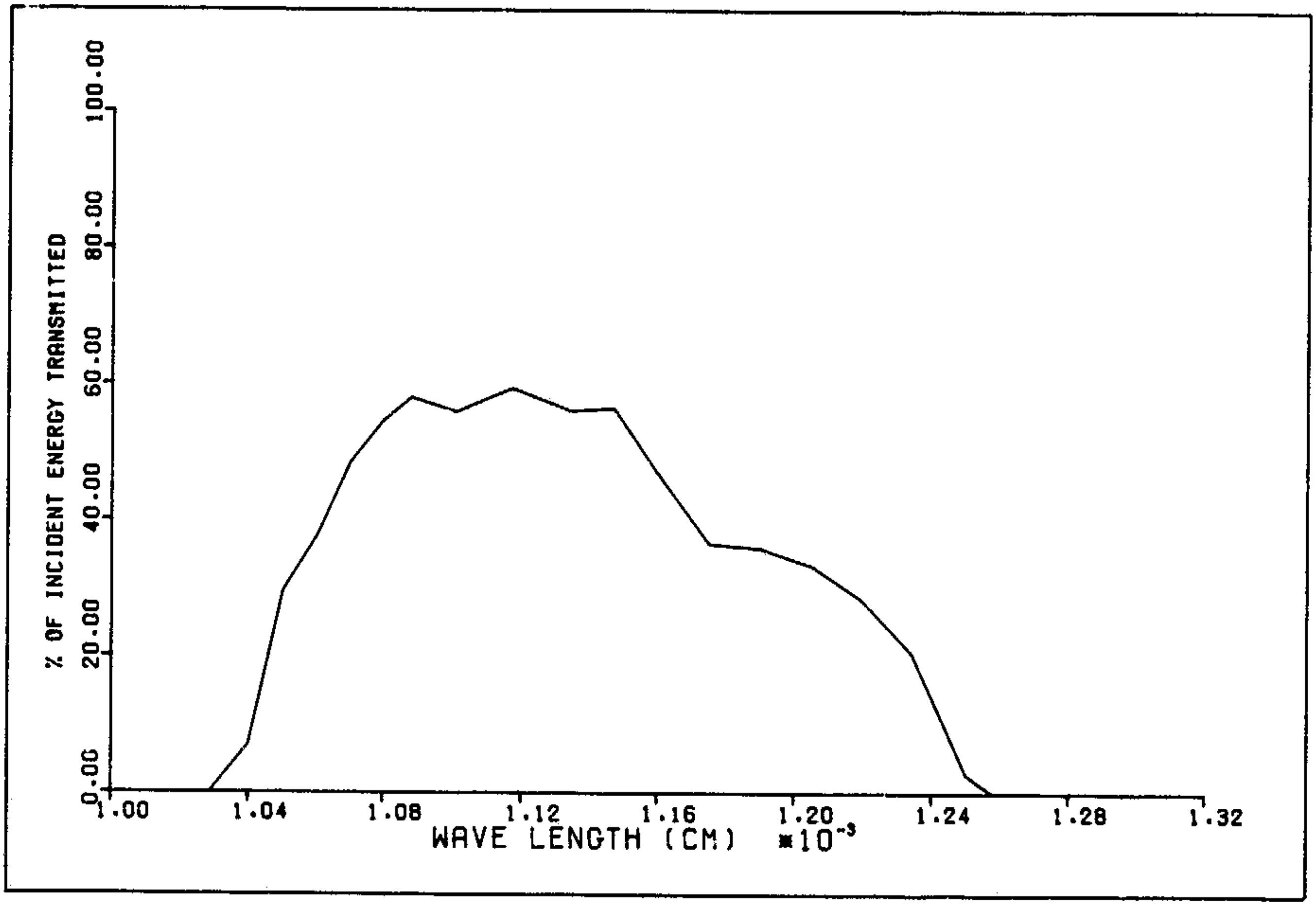

Figure 17. Filter function for HCMR.

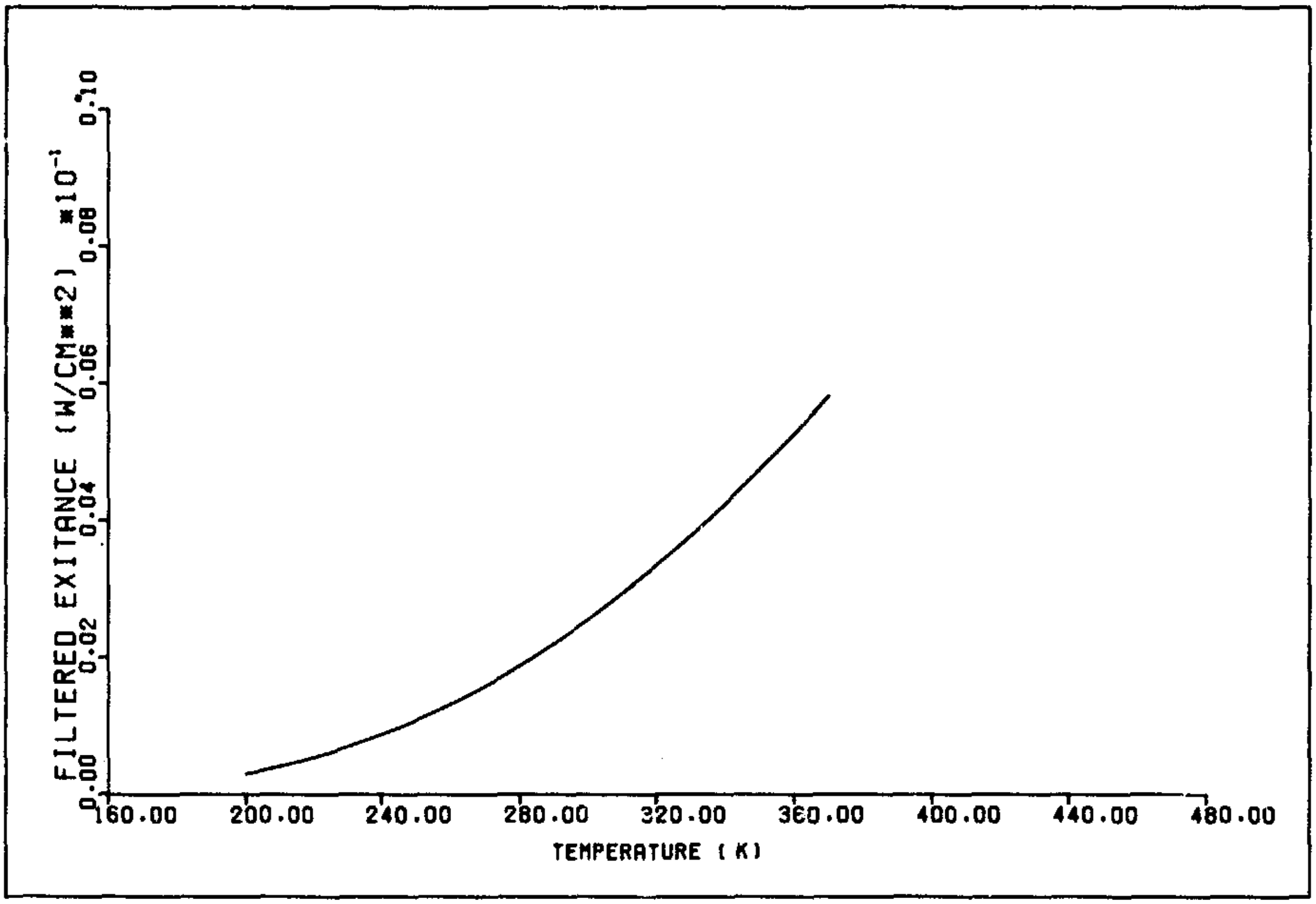

Figure 18. Temperature versus exitance curve for an ideal blackbody after passing the HCMR filtering (Figure 17).

6) Using the second look-up table, the exitance of each facet, M_i, within the pixel is determined.

7) The total nighttime exitance, M_N, is calculated:

$$M_N = \Sigma \alpha_i M_i \tag{16}$$

8) The apparent nighttime temperature, T_{N_a}, for the pixel corresponding to M_N is determined from the second look-up table.

9) Using the same values for TI and A, the apparent daytime temperature, T_{D_a}, of the pixel is determined by repeating steps 5 through 8.

10) The apparent day-night temperature difference of the pixel, ΔT_a, is calculated:

$$\Delta T_a = T_{D_a} - T_{N_a} \tag{17}$$

11) Using a range of values for TI and A, steps 5 through 10 are repeated to generate a look-up table of ΔT_a, TI, and A for the pixel.

12) Steps 3 through 11 are repeated for each pixel.

Although this algorithm is lengthy and requires the generation of a large number of separate look-up tables for areas with highly irregular topography, it is sufficiently straightforward to be readily implemented by computer. It should be noted that the algorithm does not provide for shading by adjacent topographic features which could be handled by assuming the shaded area is illuminated only by diffusely scattered sunlight (see Kahle, 1977). However, although estimation of the intensity of the diffusely scattered solar radiation is relatively simple, the determination of those areas that are shaded during each period of the day is difficult at the sub-pixel level. Shading by adjacent features should significantly affect the calculated TI only in highly irregular and steep-sided terrain.

Topography and thermal inertia. To assess the magnitude of the direct effect of sub-pixel size topography on calculated TI, portions of the algorithm described above are used on simple, idealized topographic forms with various orientations and slopes. Look-up tables of T_N (at 1:00 a.m.) and T_D (at 2:00 p.m.) for a smooth plane with various slopes and azimuths are generated using a thermal model discussed by Nash (1983) with meteorological data collected by the NOAA Environmental Data Service for Las Vegas, Nevada. Two sets of these tables are formulated: one for a surface underlain by granite (TI = 5.59×10^{-2} cal cm^{-2} sec$^{-1/2}$ K^{-1}) and another for alluvium (TI = 2.46×10^{-2} cal cm^{-2} sec$^{-1/2}$ K^{-1}) for both a winter day (January 7, 1978) and a summer day (August 15, 1978). To ascertain that an appropriate ground-temperature profile is established, the model is run for the periods January 1-7 and August 9-15 (the climatic data used in the model for these periods are shown in Figures 19 and 20). A surface albedo of 25% is assumed for all surfaces. These tables are used to calculate the apparent day-night radiant temperature difference for each topographic feature, ΔT_{T_a}, which is then ratioed with the apparent day-night radiant temperature difference for a flat plane, ΔT_{F_a}. Because the calculated value of TI will be roughly inversely proportional to ΔT_a, $\Delta T_{T_a} / \Delta T_{F_a}$ may be used to determine the magnitude of the error caused by ignoring sub-pixel size topography or by approximating the topography with a simple inclined plane.

The calculated $\Delta T_{T_a} / \Delta T_{F_a}$ of a smooth inclined surface underlain by granite for January 7, 1978, as a function of the azimuth of the normal to that surface is shown in Figure 21A. Separate curves are drawn for slopes of 10, 20, 30, 40, 50, 60, and 70 degrees to the horizontal. Figure 21B shows $\Delta T_{T_a} / \Delta T_{F_a}$ of a symmetric, two-sided "ridge" as a function of the azimuth of a normal to the

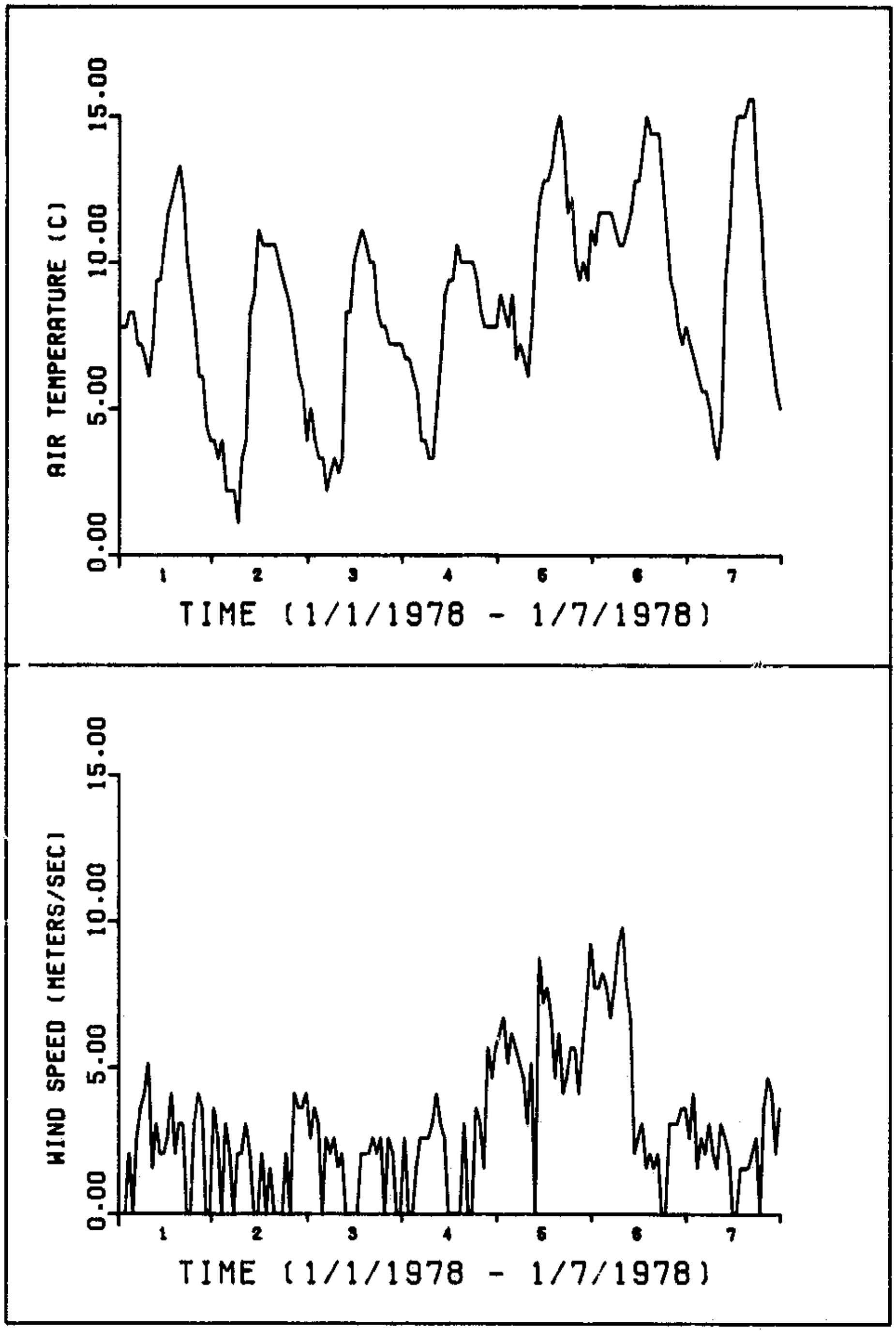

Figure 19. Hourly air temperature and wind speed as measured at the Las Vegas airport during the period from January 1, 1978, through January 8, 1978.

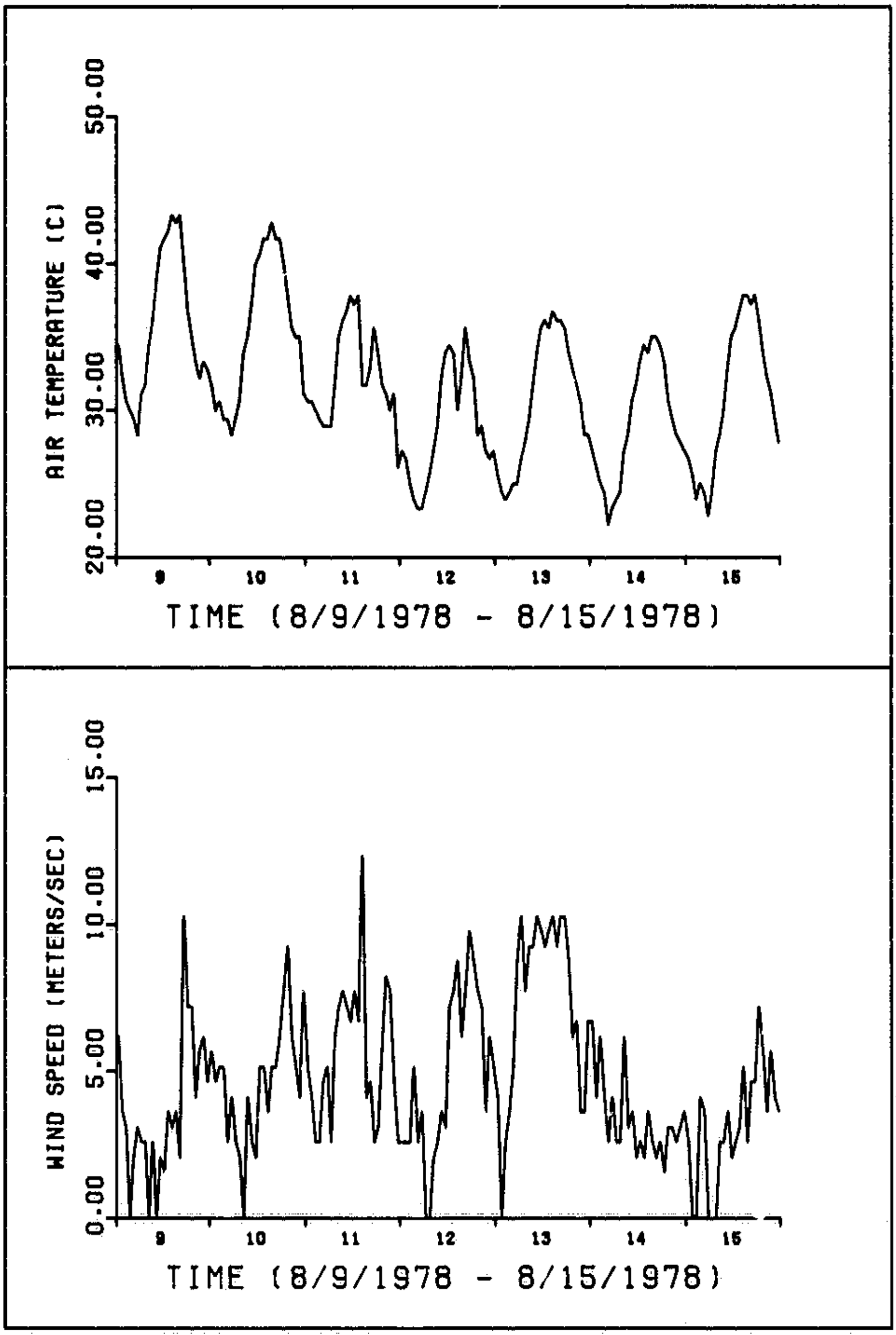

Figure 20. Hourly air temperature and wind speed as measured at the Las Vegas airport during the period from August 9, 1978, through August 15, 1978.

reference face. Similarly, Figures 21C-F are for symmetrical "pyramids" with three, four, six, and nine sides, respectively. The same set of curves for a surface underlain by alluvium is shown in Figure 22. Curves of $\Delta T_{T_a} / \Delta T_{F_a}$ on August 15, 1978, for a surface underlain by granite and by alluvium are shown in Figure 23 and Figure 24, respectively.

Figures 21-24 permit several observations to be made of the influence of sub-pixel size topography on the calculated thermal inertia:

a) $\Delta T_{T_a} / \Delta T_{F_a}$ may reach as high as 120% and as low as 10%. Completely ignoring topography will result in as much as an 83% underestimate and a 1000% overestimate of TI.

b) If topography is completely ignored, only a single south-facing plane results in a $\Delta T_{T_a} / \Delta T_{F_a}$ of over 100% and thus an underestimate of TI; all other topographic features lead to an overestimate of TI.

c) With the exception of the single inclined plane, topographic features with sides sloping at less than 20° yield a $\Delta T_{T_a} / \Delta T_{F_a}$ of greater than 95% and thus less than a 6% overestimate of TI will result from ignoring sub-pixel topography. Even rather steep features with 30° slopes result in less than a 10% overestimate of TI.

d) The most extreme values for $\Delta T_{T_a} / \Delta T_{F_a}$ result from a single inclined plane. Extreme caution should be used in fitting the sub-pixel topography by a plane for TI calculations. In many cases it will be preferable to ignore topography completely and assume a flat surface rather than to approximate a more complex topography with a simple inclined plane.

e) The number of sides of a pyramid has little effect on the resultant $\Delta T_{T_a} / \Delta T_{F_a}$ when it has four or more sides. If the sub-pixel topography has randomly oriented topography (i.e., there is no preferred "grain"

ORIGINAL PAGE IS
OF POOR QUALITY

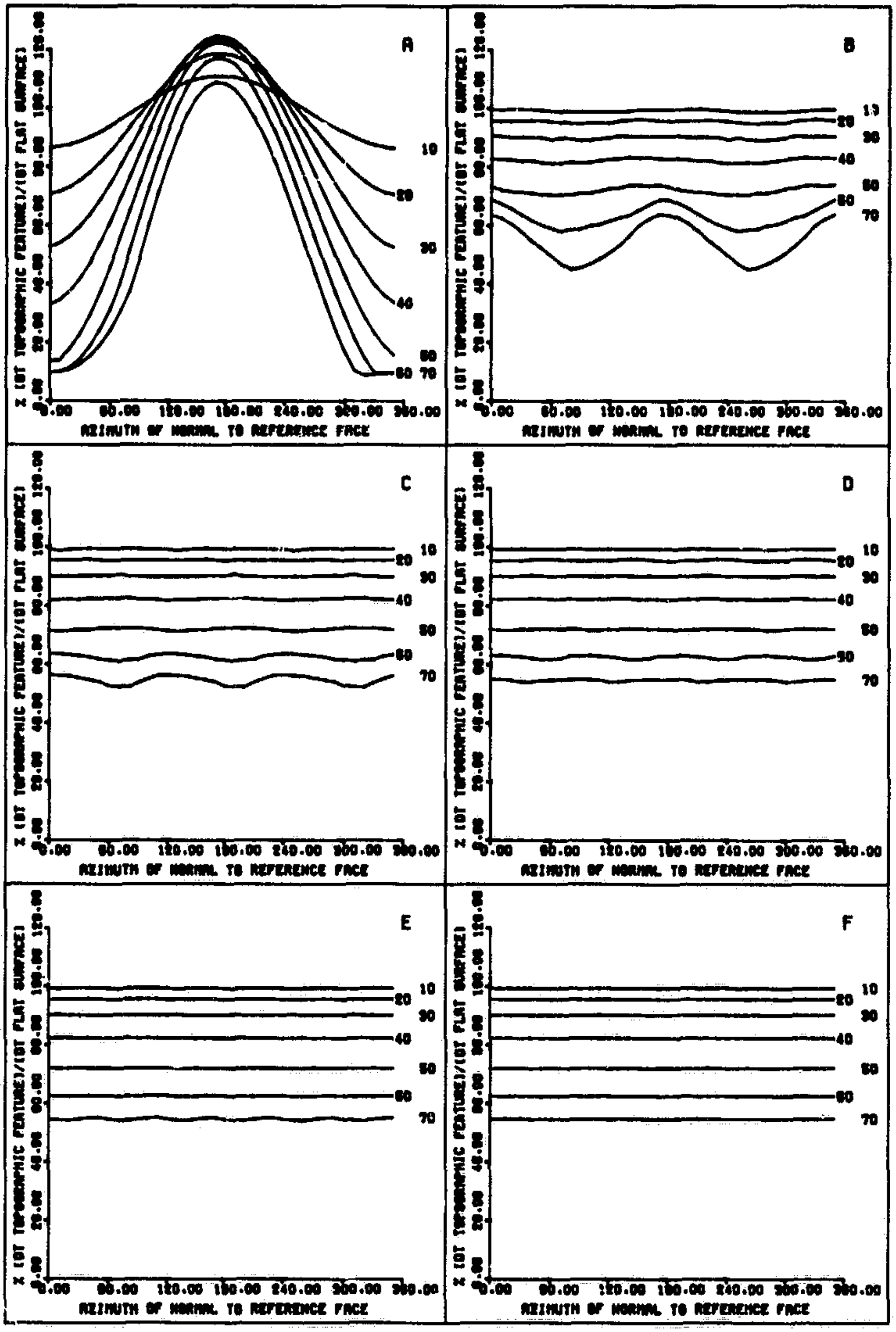

Figure 21. $\Delta T_{T_a}/\Delta T_{F_a}$ predicted for January 7, 1978 for various simple topographic forms underlain by granite: A. Simple plane; B. Two-sided ridge; C. Three-sided pyramid; D. Four-sided pyramid; E. Six-sided pyramid; F. Nine-sided pyramid. Slope in degrees is shown at right of each set of curves.

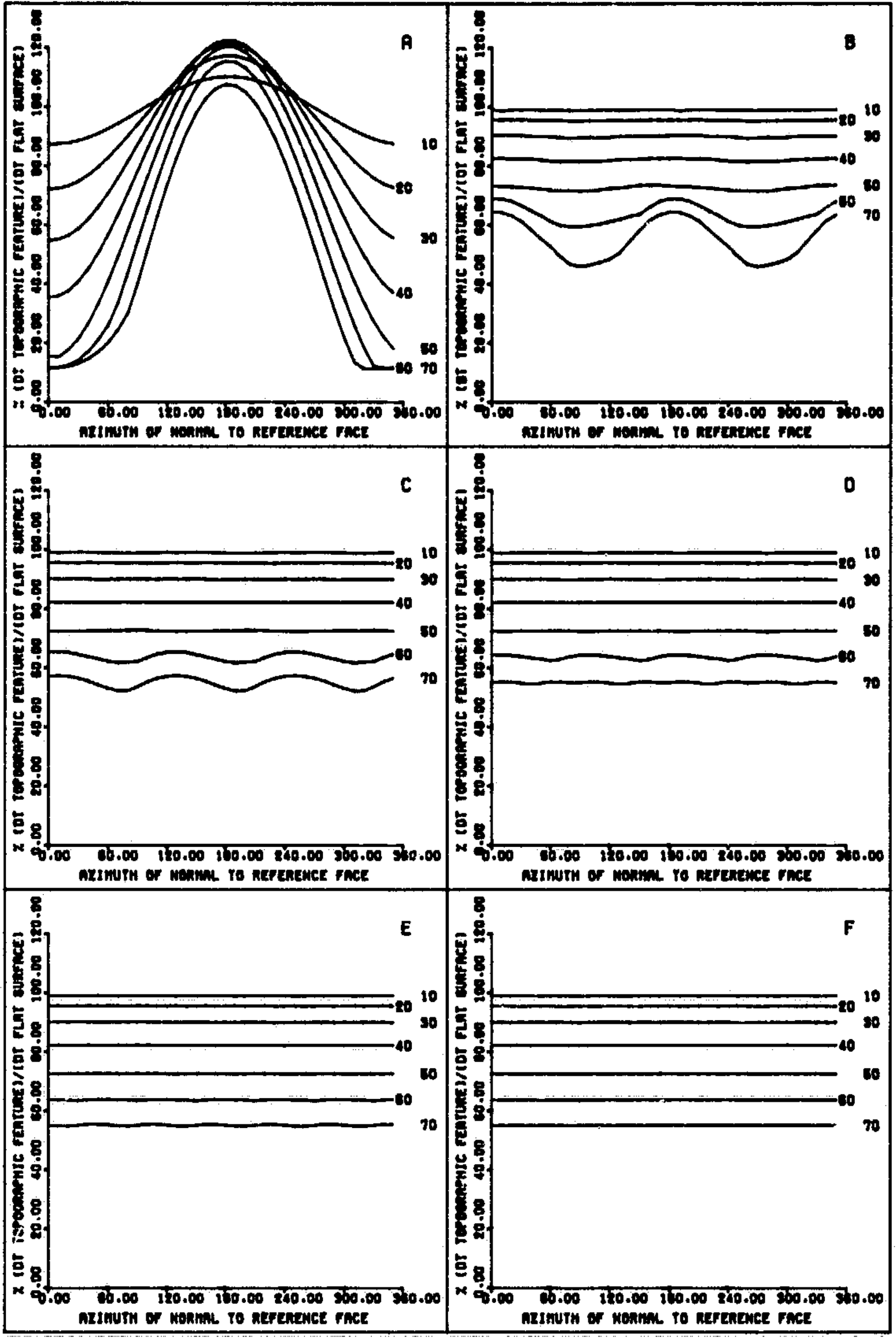

Figure 22. $\Delta T_{T_a}/\Delta T_{F_a}$ predicted for January 7, 1978, for various simple topographic forms underlain by alluvium: A. Simple plane; B. Two-sided ridge; C. Three-sided pyramid; D. Four-sided pyramid; E. Six-sided pyramid; F. Nine-sided pyramid. Slope in degrees is shown at right of each set of curves.

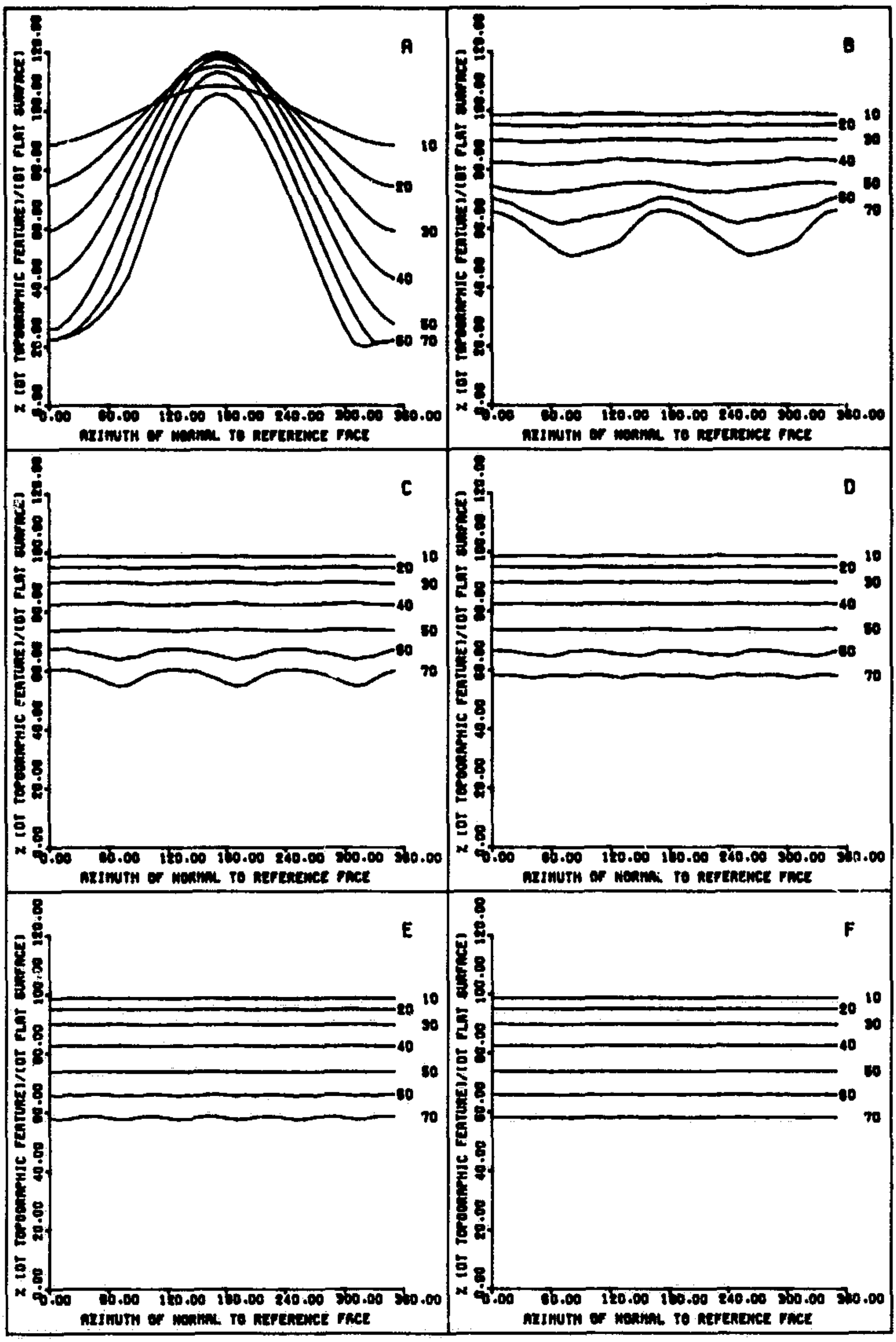

Figure 23. $\Delta T_{T_a} / \Delta T_{F_a}$ predicted for August 15, 1978, for various simple topographic forms underlain by granite: A. Simple plane; B. Two-sided ridge; C. Three-sided pyramid; D. Four-sided pyramid; E. Six-sided pyramid; F. Nine-sided pyramid. Slope in degrees is shown at right of each set of curves.

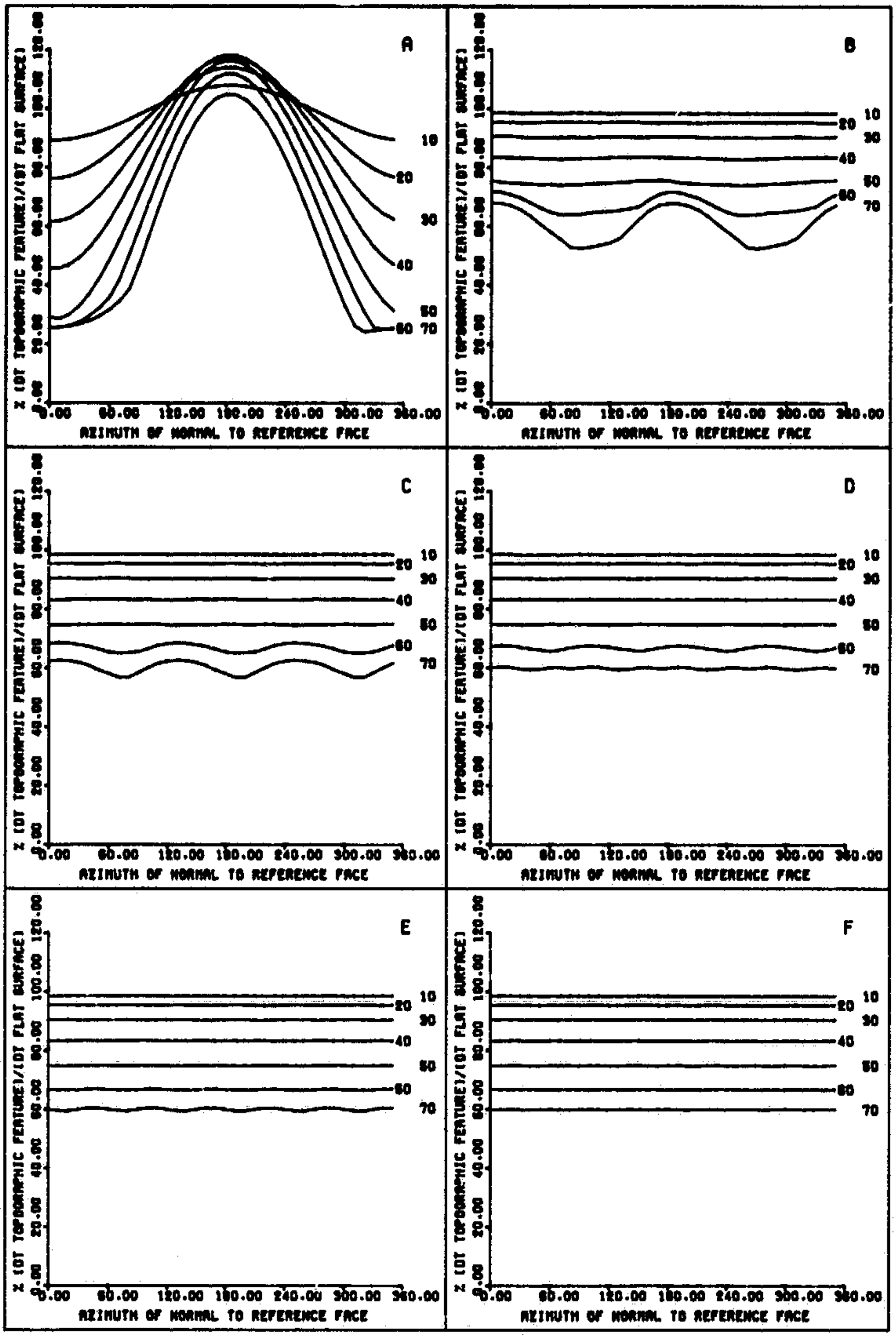

Figure 24. $\Delta T_{T_a}/\Delta T_{F_a}$ predicted for August 15, 1978, for various simple topographic forms underlain by alluvium: A. Simple plane; B. Two-sided ridge; C. Three-sided pyramid; D. Four-sided pyramid; E. Six-sided pyramid; F. Nine-sided pyramid. Slope in degrees is shown at right of each set of curves.

to the topography), little error is introduced by modeling a more complex form with a simple cone whose sides slope at the appropriate angle.

f) Topographic effects in TI values are less in winter than in summer; however, the effect is small (less than 10% increase of $\Delta T_{T_a} / \Delta T_{F_a}$).

g) The TI of the underlying material has little effect on $\Delta T_{T_a} / \Delta T_{F_a}$ calculated for a given topographic feature.

Ignoring steep-sided, complex, sub-pixel topography may result in very large overestimates of TI. Approximating such topography with inclined planes may introduce larger errors than are introduced by simply ignoring topography altogether. Because of the magnitude of its effect on calculated TI, it is recommended that:

a) An algorithm similar to the one described here be coded into a program for producing TI images of areas with irregular topographies.

b) Such a program should be used to produce an improved thermal image of a test area such as Death Valley and a cost-benefit analysis should be made on the basis of this test case.

c) Other effects of topography such as cool-air ponding, advective cooling, ponding and drainage of surface and ground water should be studied to determine the magnitude of their effect on the calculated TI.

D. Time Dependence of HCMM Data

As part of the effort to determine quantitatively correct values of TI from HCMM data we investigated the variation of HCMM data with time over our test sites. The data sets from different satellite overpasses were all co-registered, which facilitated comparisons among them. In Tables 5 and 6 we show the values of albedo and calculated TI (without atmospheric corrections)

Table 5

Albedo from HCMM Satellite Data

Test Site	Pisgah	Goldfield	Death Valley
Number of Pixels	22,400	87,040	217,500
Date			
5/14/78	.201	.180	.188
5/30/78	.207	.185	.199
7/6/78	.205	.185	.195
7/17/78	.210	.198	.207
7/22/78	.201	--	.192
8/18/78	.206	.186	.196
9/19/78	.204	--	.183
4/4/79	.190	--	--

Table 6

Thermal Inertia from HCMM Satellite Data (cal $cm^{-2}sec^{-1/2}K^{-1}$)

Test Site	Pisgah	Goldfield	Death Valley
Date			
5/14/78	0.062	--	--
5/30/78	0.063	--	0.079
7/6/78	0.061	0.048	0.075
7/17/78	0.069	0.042	0.074
7/22/78	--	0.060	--
8/18/78	0.070	0.033	--
9/19/78	0.080	0.064	--
4/4/79	0.062	--	--

for all data sets. These values are the averages over the entire test site, with the number of pixels per test site listed in Table 5. Although we have some data for all three test sites for all dates, sometimes only part of a given test site will have both day and night coverage. Albedo data are included in Table 5 only if the entire site is covered in the day overpass, and similarly, TI data are included in Table 6 only if the entire site is covered both day and night. The values of apparent TI [(1-A)/ΔT] for the same data sets are given in Table 7.

Examination of the albedo values in Table 5 indicates about a 10% change between the highest and lowest values measured. Because no atmospheric corrections were applied to these data, one might speculate that atmospheric conditions were the cause of these variations. However, on one day in particular, July 17, 1978, the albedo is significantly higher at all three sites than on any other day. During all of these overpasses meteorological measurements were being made at the Goldfield site. Rawinsonde data from the nearby Mercury, Nevada site are also available. Both field observations and the rawinsonde data indicate almost constant atmospheric conditions for the period July 17 through July 22. In Table 10 of Kahle et al. (1981) values of atmospheric transmission and radiance in the infrared, based on the rawinsonde data and the LOWTRAN model, are given for this period. At 3 p.m. on July 17, the transmission was 74.71% and the radiance was 19.97%. On July 22 these values were 74.69% and 20.05%. Field observers noted no significant haze on either day. Some small cumulus clouds were noted on July 22 for the first time in the entire period with one or two small clouds within the observer's field of view at the time of the HCMM overpass. Inspection of the July 22 HCMM images reveals perhaps four small clouds and cloud shadows across the entire 87,040-pixel test site. No clouds were noted in the July 17 images. The presence of a few isolated clouds

Table 7

Apparent Thermal Inertia from HCMM Satellite Data (cal $cm^{-2}sec^{-1/2}K^{-1}$)

Test Site	Pisgah	Goldfield	Death Valley
Date			
5/14/78	.038	-	-
5/30/78	.038	-	.044
7/6/78	.037	.039	.045
7/17/78	.044	.035	.046
7/22/78	-	.038	-
8/18/78	.043	.034	-
9/19/78	.047	.043	-
4/4/79	.038	-	-

and cloud shadows in the July 22 scene should raise the albedo slightly, if anything. Yet it is the July 17 scene which has the apparently anomalously high albedos. Thus because we can find no atmospheric variation we suggest a possible variability in the HCMR sensor itself over a period of a few days.

Also, in Table 5 we note the substantially lower albedo for Pisgah in April of 1979. Although the Goldfield and Death Valley scenes were not complete, they also showed lower average albedo over the portion measured. These lower values may represent a loss of sensitivity of the HCMR sensor as it neared the end of its life.

From Table 6 and Table 7 we see that the variability of the calculated values of TI and apparent TI over the test sites is much larger than the variability of the albedo values. This is to be expected because of the dependence of the surface temperature upon so many more variables than the albedo. No consistent patterns of change are noted among sites or with time. It is interesting that the TI values based upon the models, with local meteorological data included, are no more consistent with time than are the apparent TI values. In fact, for the Goldfield site on August 18, 1978, the modeled value is much farther from the average value than is the apparent TI. Both methods give lower TI on August 18 than for any other time period at Goldfield. Examination of the meteorological data indicates extremely windy conditions throughout the night prior to the measurements. Ordinarily, wind will increase the sensible heat transfer between the air and the ground, so that the ground temperature will more closely follow the air temperature. Usually the ground has a much larger diurnal temperature range than the air. Windy conditions should thus tend to lower the diurnal temperature range of the ground. The apparent TI, dependent upon $1/\Delta T$, should thus be larger. However, as noted, on August 18 it was smaller. On the other hand, the model should compensate for the wind and produce the correct TI. However, as noted above, the apparent TI was smaller during windy periods, and the modeled TI--reduced to compensate for wind--was even smaller. Apparently some other process must be at work. In this case, because the average albedo is not larger than usual, the day-night temperature difference must have been larger than usual for this time of year. Perhaps a different air mass, associated with the windy conditions, came into the area. This is only one example of the numerous variables that can affect the calculations. Other important factors are moisture related and include soil moisture, humidity, cloudiness, and rainfall.

E. Use of the Annual Heating Cycle for the Remote Sensing of Faults

The surface of the ground undergoes a diurnal and annual heating and cooling cycle. The amplitudes of the resulting surface temperature cycles are inversely proportional to the TI of the surface material. Generally, bedrock will have a significantly higher TI than alluvium and therefore will be subject to smaller fluctuations in temperature over the heating and cooling cycle. If the bedrock is overlain with a thin veneer of alluvium, the "effective thermal inertia" of the surface should be intermediate to that of the alluvium and of the bedrock. With increasing thickness of the alluvium veneer, the effective TI should be progressively closer to that of the alluvium than the bedrock until at some threshold depth of burial, the bedrock exerts no influence on the surface temperature and the "effective thermal inertia" of the veneered bedrock is identical to that of the alluvium alone. This threshold depth is a function of the depth to which the heating and cooling pulses penetrate into the ground. Because this depth of penetration is proportional to the square root of the cycle period, the depth of penetration should be 19.1 times greater over the annual rather than diurnal cycle. Buried bedrock should thus be detectable at much greater depths when observed over the annual rather than diurnal cycle.

A FORTRAN program was formulated to model the heat flow within an alluvium over granite system (Nash, 1983). The hourly air temperature and wind speed measured by NOAA at Las Vegas, Nevada, during 1978 were used in the model, on the assumption that this record would generally be representative for pediments in the Southern Basin and Range region. The latent heat flux is ignored in the model. The program was developed to investigate the feasibility of using HCMM thermal images to detect alluvium-buried, faulted pediment surfaces similar to that shown in Figure 25. Based on the preceding discussion, the surface temperature of the upthrown side, T_u, should be warmer during the cooling cycle and cooler during the warming cycle than the surface temperature of the downthrown side, T_d.

The results of the study are shown in Figure 26. For a fault with a 2 m vertical displacement in a granite pediment, the maximum positive (reached in the winter) and negative (reached in the summer) contrasts between T_u and T_d decrease rapidly with increasing depth of burial by the alluvium. When the depth of burial is 1 m, the contrast is about 0.15 K. The optimal times for detecting the contrast are February (the low point of the annual ground temperature cycle) and August (the high point of the annual ground temperature cycle).

Although the temperature and spatial resolution of HCMM are probably not sufficient to detect some buried bedrock faults, it appears that some aircraft-borne thermal scanners do have adequate resolution. A field study is underway.

F. In Situ Measurements of Thermal Inertia

Remote thermal sensing of terrestrial surfaces provides a means of

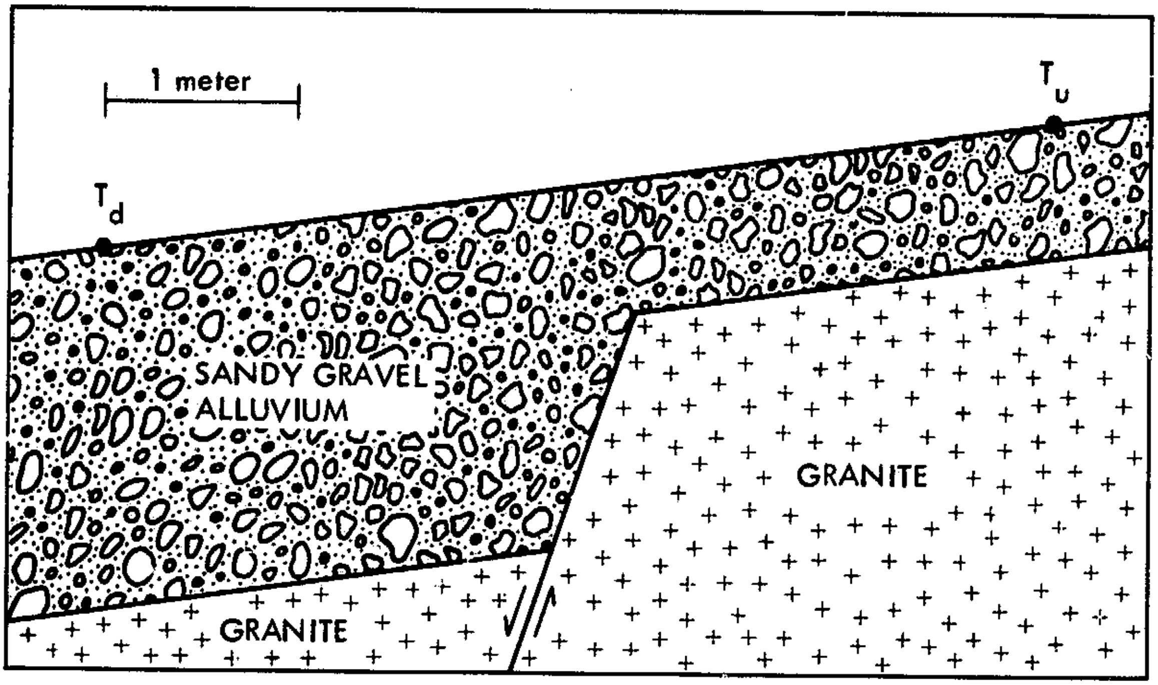

Figure 25. Idealized cross-section through an alluvium-veneered, faulted, granitic pediment surface. The depth to bedrock influences the surface temperature resulting in a contrast in the surface temperatures on the upthrown (T_u) and downthrown (T_d) sides of the fault.

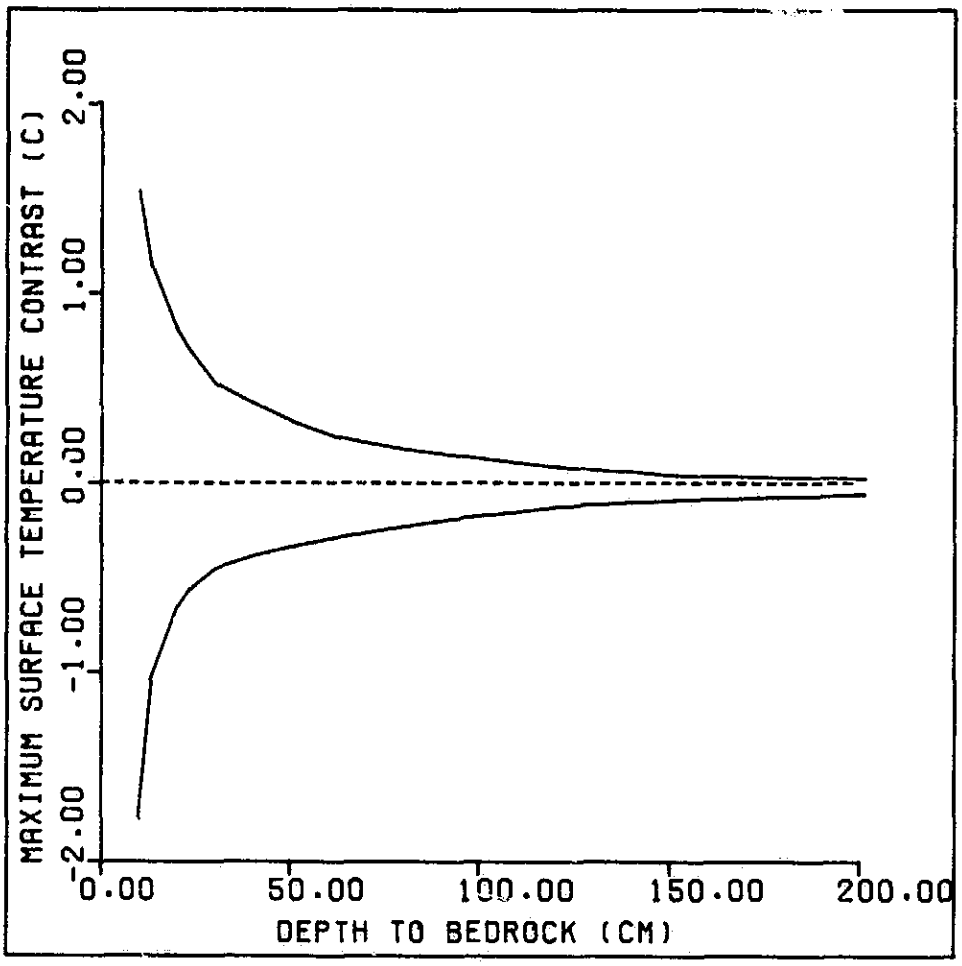

Figure 26. Predicted maximum temperature contrast (T_u-T_d) across the fault shown in Figure 25 during the winter (upper curve) and summer (lower curve).

determining the surface TI. The interpretation of thermal images depends on being able to associate the derived thermal properties with the material on the ground. Laboratory measurements of conductivity, K, specific heat, c, and density, ρ, provide some guidance but are generally inadequate for estimating the thermophysical properties of complex heterogeneous real surfaces. For this task an in situ technique is preferable.

Such a technique has been implemented at JPL with the Thermal Inertia Meter (TIM) and is discussed in Kahle et al. (1981) and Marsh et al. (1982). The method used introduces a short pulse (four minutes) of energy into two standards (K, ρ, c known from laboratory measurement) and a sample (unknown TI) and uses measurement of the temperature increase at the end of this heating to determine the TI of the sample. In application it was noticed that the calculated TI showed a systematic dependence on the reference standard (sand or dolomite). An attempt has been made to understand and remove the sources of this systematic difference.

We have identified three sources of error:

1. Timing. The low TI sand standard cools quickly. It is difficult in reading a meter by eye to correctly assess the peak temperature at the end of heating. Using rapid (0.3 sec) digital recording at the end of the heating period eliminates this problem and indicates the maximum temperature of the sand may have been underestimated by as much as 1 K.

2. Brightness temperature. The surface temperature of the standards and sample are measured using a radiometer operating in the 8 to 14 μm region. The quartz sand used as a standard has a much lower emissivity in the 8 to 10 μm region than the dolomite standard. This combined with the higher final temperature of the quartz leads to a 2 K differential error between the quartz and the dolomite.

3. Non-uniform heating across the standards and sample. Two-dimensional infrared images of the heated standards revealed a pattern of non-uniform heating from the lamp-reflector combination. Since the conductivity of the dolomite is more than an order of magnitude larger than that of the sand, lateral heat conduction in the dolomite is significant.

The three sources of error outlined above can either be eliminated through improvements in instrumentation or design (1 and 3) or accounted for in the computation (2). In addition, it is possible that coating both the standards and sample with a thin (10-100 μm) layer of high-emissivity material (e.g., lampblack) could remove any remaining uncertainty due to differences in emissivity and absorbance.

Investigating and identifying the sources of systematic error in this *in situ* measurement technique has greatly increased confidence that high-accuracy field measurements of TI can be made.

III. INTERPRETATION

A. Death Valley

The Death Valley salt pan and the surrounding alluvial fans, mountains, and valleys, have a wide range in TI, surface albedo, and surface relief at all size scales including the 0.5-km resolution of the HCMM. As such this area represents an ideal testing ground to demonstrate and improve the ability to interpret thermal images.

The initial JPL HCMM report (Kahle et al., 1981) presented aircraft scanner and HCMM thermal and albedo images in which the origin of a number of TI features could not be identified without additional field observation. Here we report the results of that effort, including use of images based on additional computations aimed at removing (to first order) the effect of atmospheric attenuation and emission on the raw HCMM brightness-temperature measurements.

The regional TI setting for Death Valley can be seen in the image presented as Figure 27. The areas of lowest TI (three shades of blue) are associated with the principal valleys of the region ranging from the Amargosa Desert on the right of Figure 27 through the Mesquite Flat area of Death Valley (arrow-shaped blue region in the upper middle of the image) and the Panamint Valley (linear blue feature in the lower left of the image). Significantly, Death Valley south of Mesquite Flat contains few low TI regions, and in the Devil's Golf Course area of Badwater Basin the TI reaches values nearly as high as the highest values in the rock outcrop areas of the surrounding mountains. In Figure 27 each color represents a range in TI. The numerical range of TI represented by each color can be obtained from the population histogram below the image. Although this form of image display lacks the subtle detail which can be found in continuous-tone color or black and white TI images, it has the significant advantage that quantitative comparison of TI values can be easily made throughout the image.

Field investigation of the Death Valley salt pan was carried out in December 1981 and May 1982. The principal focus of these field trips was the investigation of regions representing extremes in thermophysical properties (high and low albedo and TI), examples of which are shown in the albedo and TI images of the valley (Figures 28 through 31) acquired with NASA's Bendix 11-channel aircraft multispectral scanner (M^2S).

North of the Furnace Creek fan and ranch in Figure 30, in southeast Cotton Ball Basin, is a distinct high TI area (white) of irregular outline. On the corresponding albedo image (Figure 28) the area of high TI can be seen to be included in an area of high albedo. In contrast to this association of high TI

ORIGINAL PAGE
COLOR PHOTOGRAPH

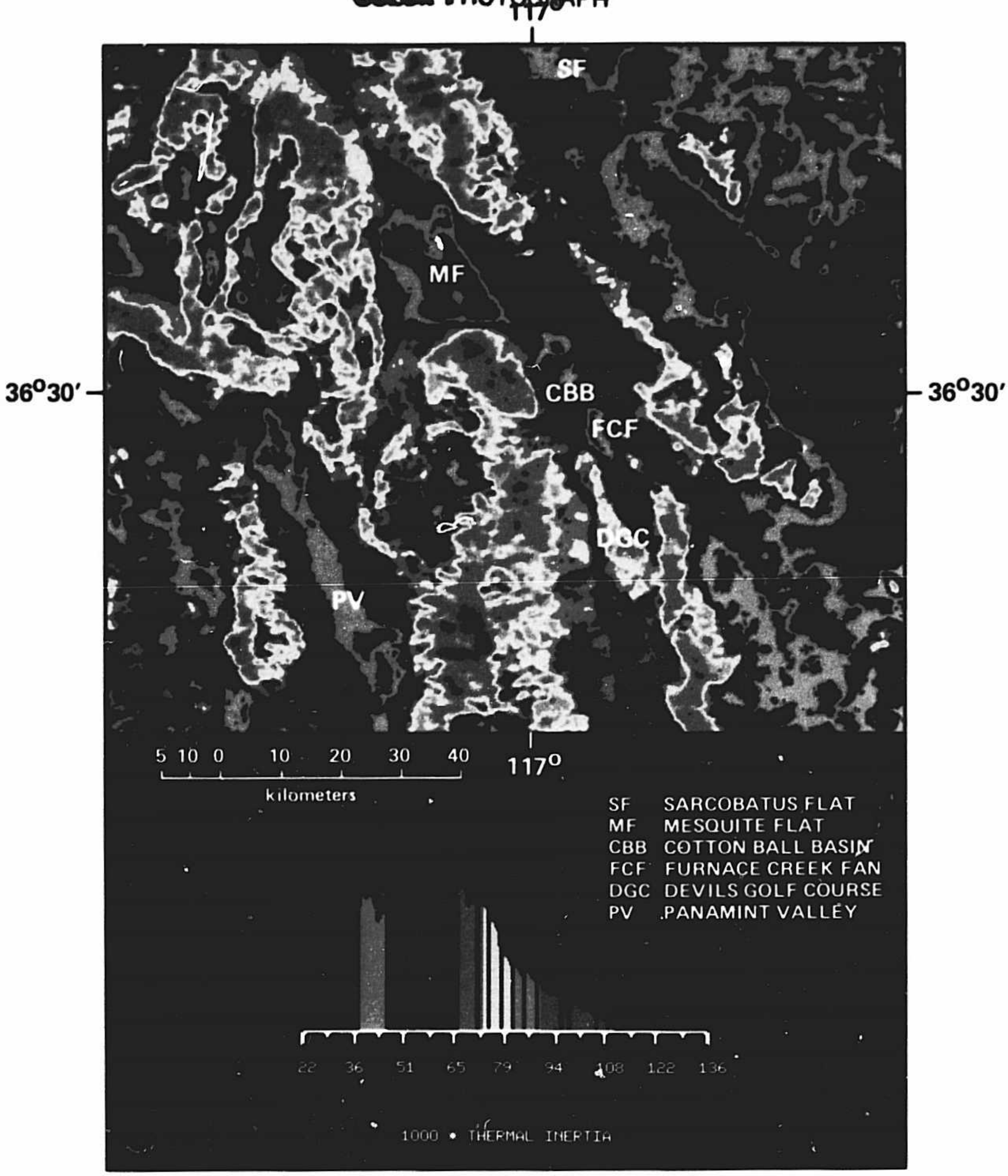

Figure 27. Color-sliced thermal inertia image of the Death Valley, CA, region constructed from HCMM data of July 6, 1978. The brightness temperatures used were corrected for atmospheric scattering, absorption and emission prior to thermal inertia computation. The thermal inertia range for each color slice may be read from the population histogram below the image in units of cal $cm^{-2}sec^{-1/2}$ K^{-1} x 10^3. Mesquite Flat northwest of the Death Valley salt pan is the blue arrow-shaped feature in the upper center of the image. The arrow points toward Cotton Ball Basin at the upper end of the salt pan.

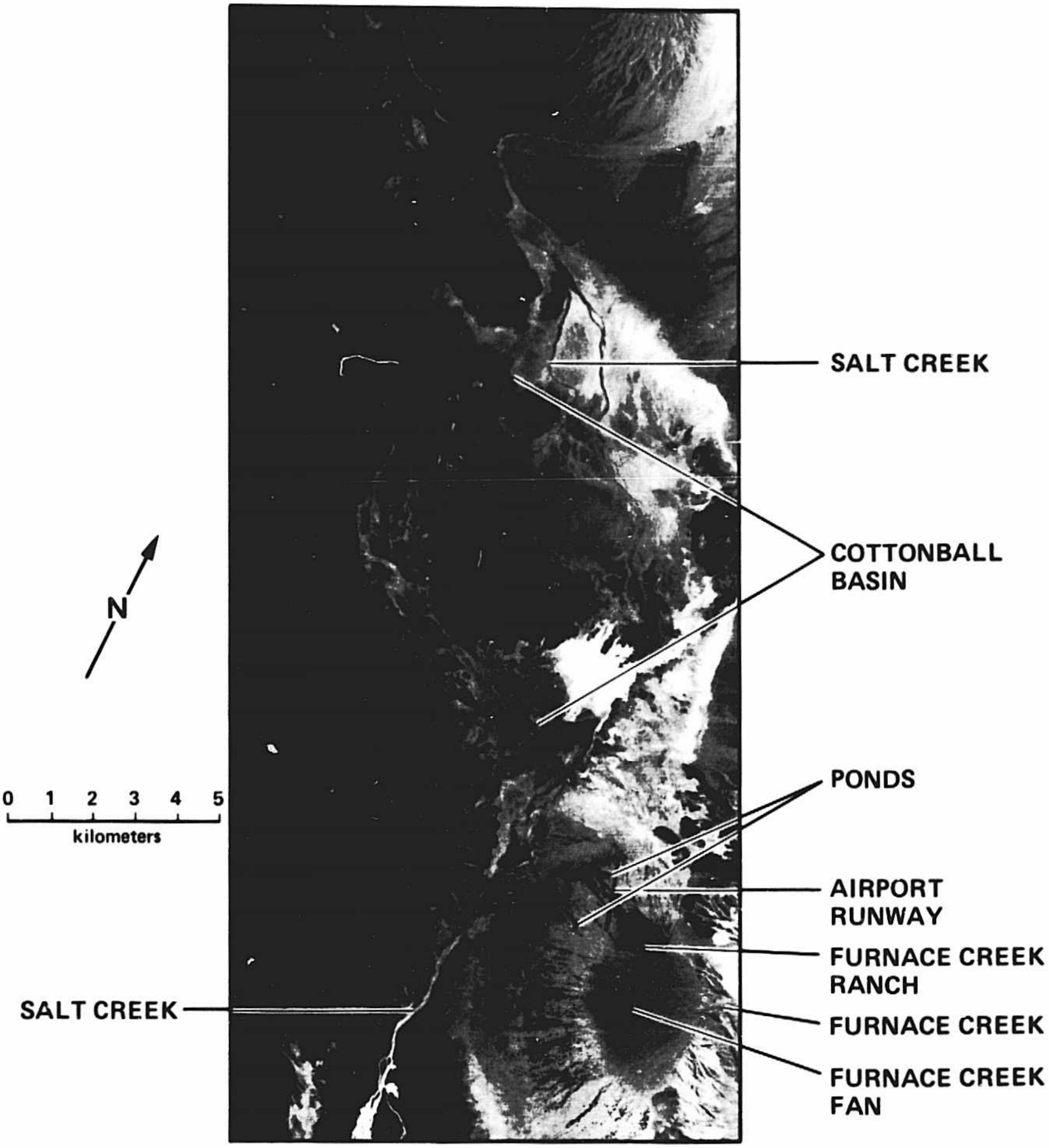

Figure 28. M^2S visible image of the northern half of Death Valley obtained from an aircraft flight on March 11, 1977.

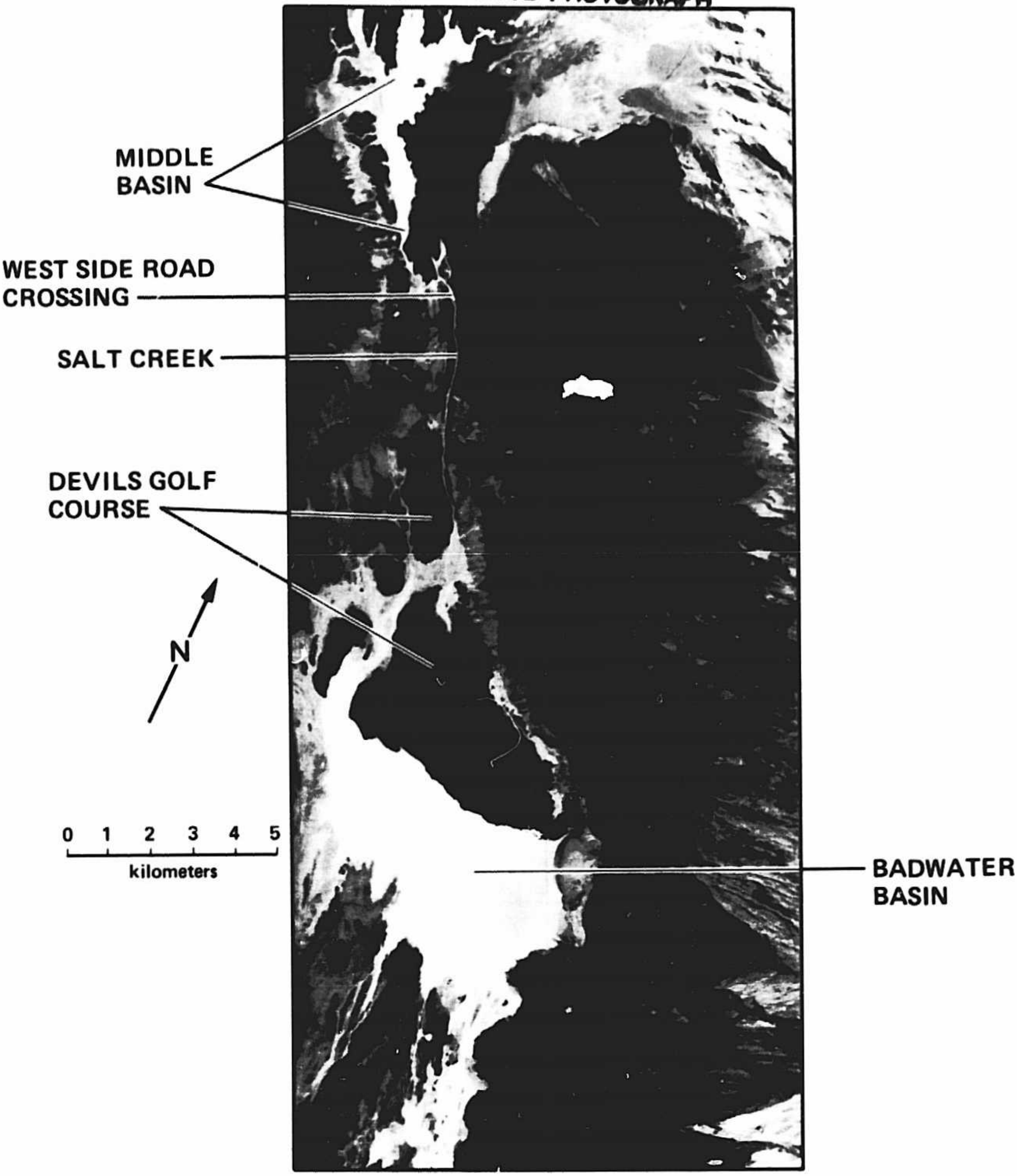

Figure 29. M^2S visible image of the southern half of Death Valley obtained from an aircraft flight on March 11, 1977.

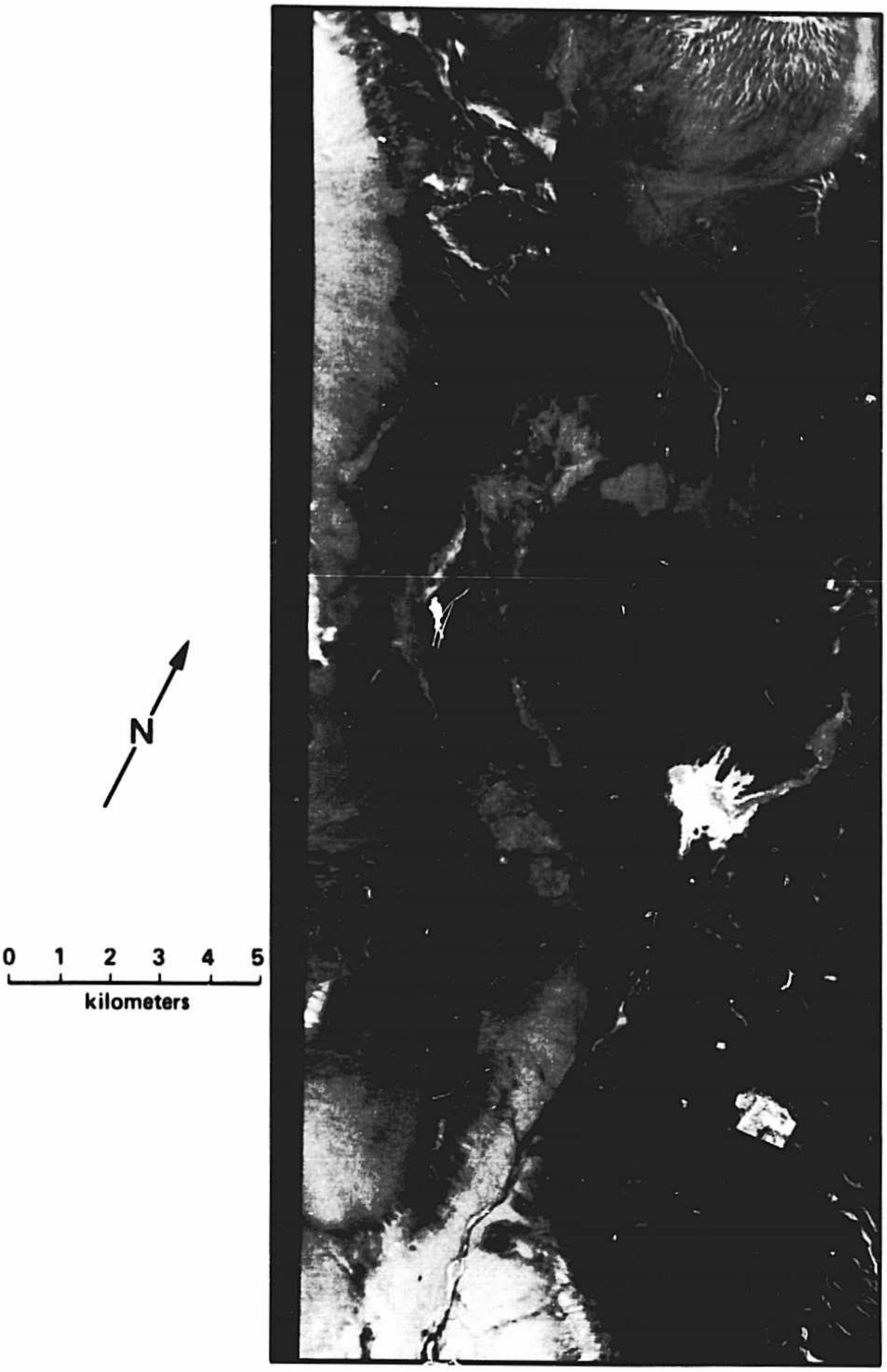

Figure 30. Thermal inertia image of the northern half of Death Valley derived from data acquired from aircraft flights on March 11, 1977.

ORIGINAL PAGE
BLACK AND WHITE PHOTOGRAPH

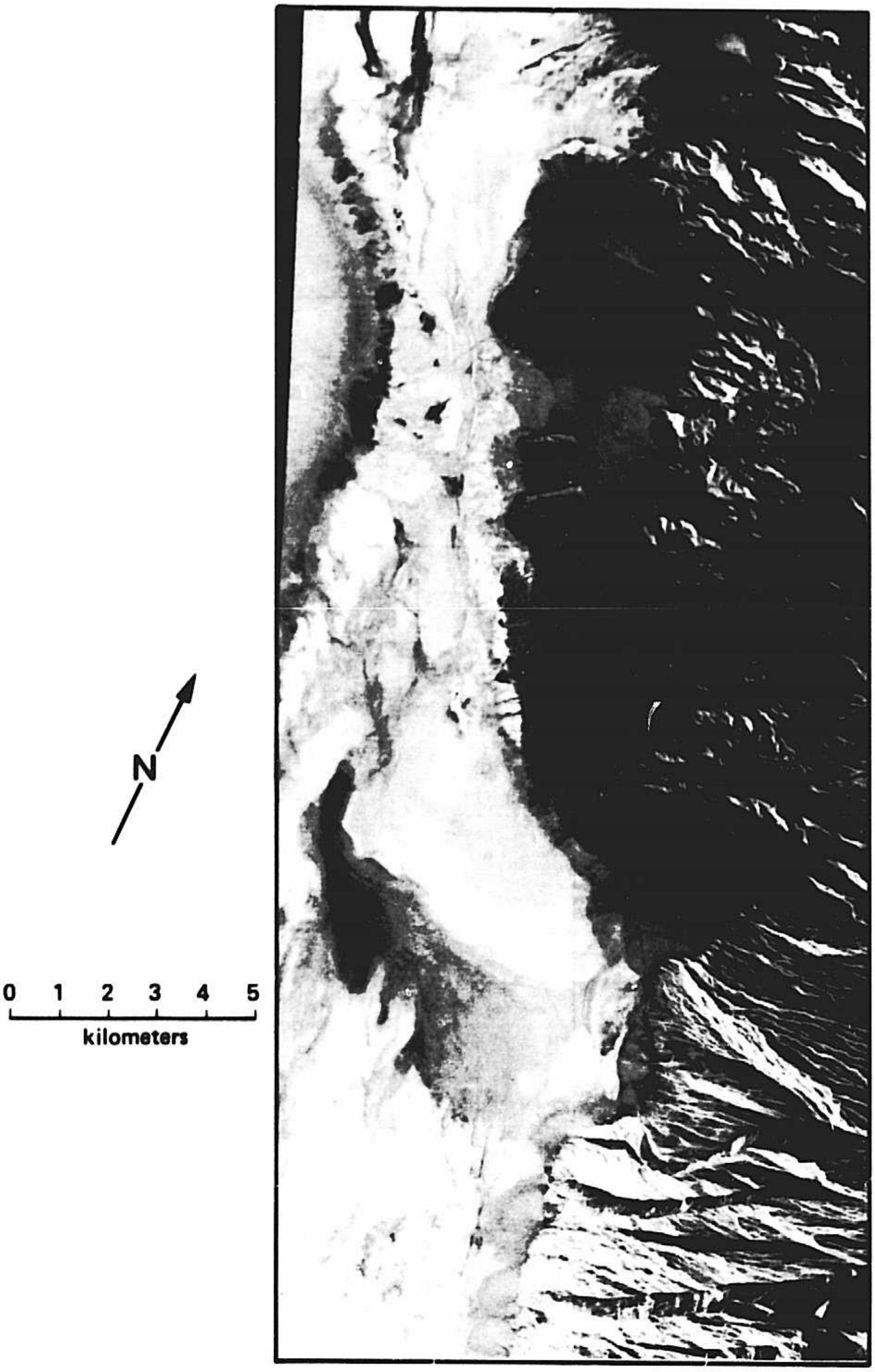

Figure 31. Thermal inertia image of the southern half of Death Valley derived from data acquired from aircraft flights on March 11, 1977.

and albedo is a region in the Middle Basin shown in the upper left of Figures 29 and 31. Here, in the albedo image of Figure 29, can be seen a Y-shaped feature, the right branch and stem corresponding to the widened channel of Salt Creek which can be traced to the south where it enters Badwater Basin. On the TI image (Figure 31), the left branch and portions of the right branch and upper stem appear to have a low TI, while a wide portion of the lower stem is of high TI, as is the extension of Salt Creek to the south (except for several interruptions by distinct low TI areas). In December 1981 when this area of Middle Basin was investigated by walking north up the course of Salt Creek from its intersection with the West Side Road, the high TI areas in the 1977 image within the flood plain of Salt Creek were found to correspond to areas covered with water ranging in depth from 0 to 3 or 4 cm. The high albedo results from the crust of salt, deposits of which are extensive on the flood plain. The low TI regions correspond to slightly elevated areas having a skin of salt deposited over a silt/clay base. Farther from the center of the salt pan toward the west-side fans, the rim of lowest TI material below the foot of the fans consists of extensive erosional bays in the thick elevated salt deposits that border Salt Creek in this area. The ponding of water in this section of Middle Basin is the consequence of recent uplift (45-50 cm) on the anticline separating Middle and Badwater Basins (Hunt et al., 1966). We cannot be certain that the extent and depth of water in 1977 was the same as that observed in 1981, but examination of the rainfall record from Furnace Creek, which is shown in Figure 32, does not indicate the occurrence of any unusual events in 1977. When we reexamined this lower portion of Middle Basin in May 1982, the standing water had largely disappeared, leaving in the lowest areas a salt slush or a thin (less than 1 cm) water layer with a salt skin.

When the high TI area in southeast Cotton Ball Basin (Figure 30) was

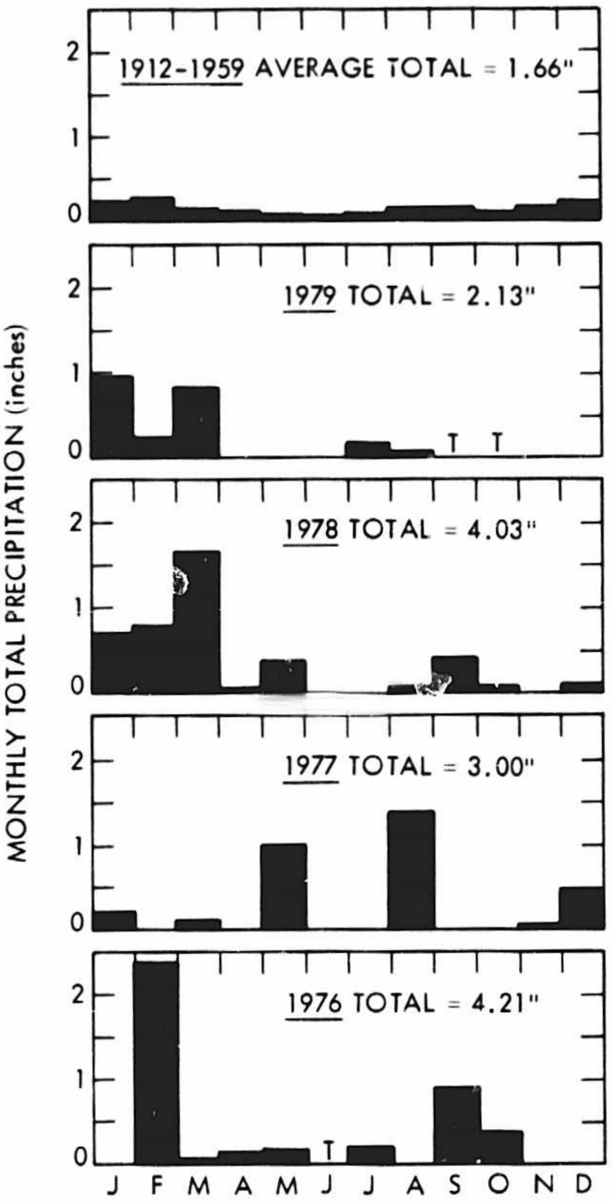

Figure 32. The average monthly rainfall record for Death Valley National Monument (Furnace Creek) for the years 1912 through 1959 (Hunt et al., 1966) and the monthly rainfall record for the years 1976 through 1979 (National Oceanic and Atmospheric Administration, 1976-1979). The symbol T implies a trace of rain (i.e., less than 0.01 in.).

investigated in December 1981, it too had a large thin sheet of surface water up to 7 cm deep underlain by a thin salt crust. To the west and south the surface consisted of salt crusts underlain by silt and clay. In the absence of surface water this surface dries out and has a lower TI than the water covered area. To the north and east of the water-covered area are extensive deposits of silty rock salt in various states of erosion. For the most part these surfaces are elevated (up to a meter or more above the valley floor) and contain a cap of silt. The contrast in TI between the silty rock salt deposits of the central region of Cotton Ball Basin (seen in Figure 27 as a core of low TI material) and the massive rock salt deposits of the Devil's Golf Course area of Badwater Basin (which Figure 27 shows as the highest TI in the salt pan) is due to the thicker silt capping of the salt deposit in Cotton Ball Basin, and the greater degree of subsurface saturation in the Devil's Golf Course area. In May 1982 surface water had disappeared from this area of Cotton Ball Basin, although in the formerly wet area water was present immediately below the surface.

Close examination of Figure 30 reveals a line of high TI material along the foot of the gravel fans in southwest Cotton Ball Basin. This corresponds to a series of springs and seeps. In May 1982 there was little surface water present but the ground was moist in these areas. This line of springs and seeps is contained within a band of low TI material which is distinctly different from the moderate TI of the fan gravels to the east and the high TI of the springs and seeps. This low TI material has at the surface a thin (0.2-0.5 cm), puffy, porous crust overlying loose dry silt and sand. The strong diurnal thermal fluctuation of this surface is a consequence of the low density of the crust and the loose bonding (interparticle contacts) of the material beneath the crust. This type of surface is common at the upper rim of the salt pan below

-73 m (-240 ft) elevation. This crust and the smooth silt and clay discussed in conjunction with Middle Basin are two surface types which exhibit low TI within the salt pan. Surfaces of these two types also produce the band of low TI along the west side of the salt pan (Figure 27).

South of Cotton Ball Basin on the east side of Death Valley a large area of low TI can be seen in Figure 27. This region corresponds to the lower 60% of the Furnace Creek fan. The TI variation on and around this fan can be seen in greater detail in Figure 30. This is the only low TI fan on either side of the Death Valley salt pan. All the other fans are covered with gravels of several ages and have an intermediate TI, as does the upper 40% of the Furnace Creek fan which is covered by the youngest (Recent) gravels mapped by Hunt and Mabey (1966). Their geologic map indicates that the lower portion of the Furnace Creek fan (below -61 m (-200 ft) elevation) contains large areas of carbonate-zone sand facies of late Pleistocene age, with younger carbonate salts impregnating sandy playa or lake deposits. The sand facies are separated by drainage channels along which grow honey mesquite (Prosopis juliflora) in association with sand dunes which the honey mesquite help to stabilize (Hunt, 1975). The transition to the low TI surface occurs in the vicinity of the -58 m (-190 ft) contour where the fan is undergoing a change in slope from greater than 2° on the upper gravel portion of the fan to approximately 0.7° near the foot of the fan, as shown in Figure 33. When the low TI surface was examined in May 1982 it was found to consist of a thin (0.3-0.7 mm), porous, friable upper crust over silt and sand. The surface had low relief with an irregular puffy appearance which compressed several centimeters underfoot. As for the similar material around the springs of east Cotton Ball Basin, it was the low density, dry, loose bonding of the fine particles which was responsible for the low TI.

The lower portion of the Furnace Creek fan is also unusual in another

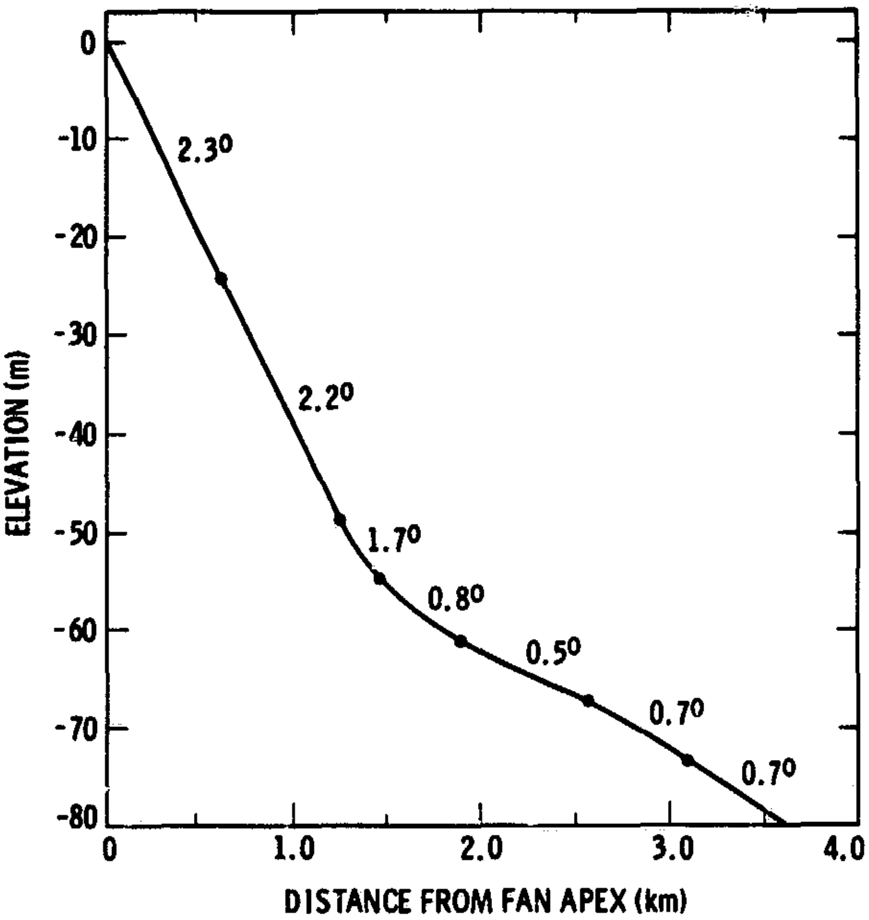

Figure 33. Radial profile of the Furnace Creek fan from near the fan apex at sea level. Drawn from the Furnace Creek Quadrangle U.S.G.S. topographic map. Fan slope, between elevation intervals marked by dots, is given in degrees.

respect in that it is the largest area bordering the salt pan which supports phreatophytes (Hunt, 1975). Such plants send their roots to the vicinity of the water table and thus depend on a year-round supply of water. The honey mesquite is one of the least salt tolerant of this group of plants, growing where the salinity is less than 0.5%. In their study of the hydrology of Death Valley, Hunt et al. (1966) estimated the total ground water discharge in the valley at 8,000 gallons per minute of which 2,000 gallons (25%) is through Travertine Springs and the underflow of Furnace Creek. Prior to its use by man, this water discharged into the Furnace Creek fan at its apex. A portion of this water currently supports the phreatophytes of the lower fan, and evaporation through the lower fan may be related to the development of the low TI surface.

The Furnace Creek fan also provides an example of how thermal measurements can aid in the interpretation of man-made features. At the north end of the fan (Figure 28) and northwest of the Furnace Creek Ranch, the airport runway can be seen as a gray linear bar, about 2 km in length, against the brighter surroundings. When the TI image of Figure 30 is compared with this albedo image (Figure 28), only the southern half of the runway has a significantly higher TI than its surroundings. When examined in 1982, the southern half of the runway was paved but the northern portion was not. The surface of the unpaved runway was soft and incompletely covered with pebbles smaller than 1 cm. The greater compaction of the unpaved surface resulting from its construction, and the presence of pebbles, are responsible for its having slightly higher TI than its surroundings. The fine-grained, dry, loose texture of the majority of the surface is responsible for its overall low TI.

West of the airport runway on the Furnace Creek fan are two sets of water treatment ponds. West of the northern end of the runway there is a triplet of rectangular ponds. The second triplet of ponds, west of the south end of the

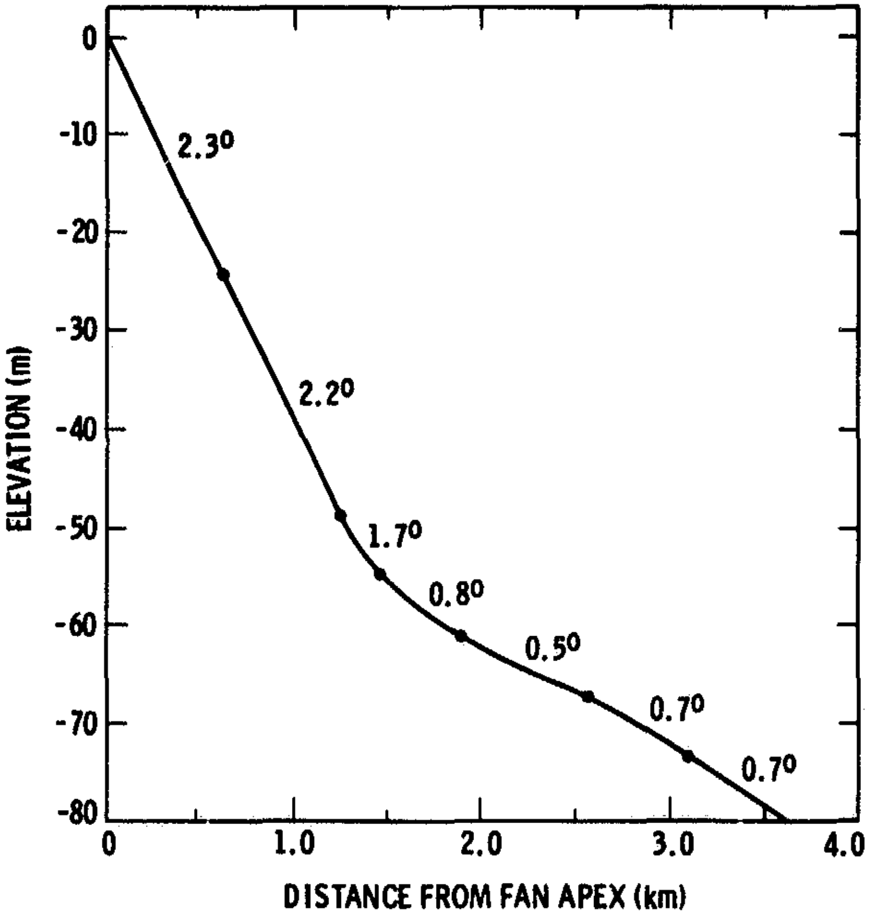

Figure 33. Radial profile of the Furnace Creek fan from near the fan apex at sea level. Drawn from the Furnace Creek Quadrangle U.S.G.S. topographic map. Fan slope, between elevation intervals marked by dots, is given in degrees.

runway, forms sectors of a circle. In March 1977 the ponds were unequally filled as is evident from the association of high albedo with moderate TI and low albedo with high TI. In May 1982 water was deeper in the high TI ponds of the 1977 TI image.

In summary, the low TI surfaces in Death Valley which we examined are of three types; all are dry and composed of fine material (sand, silt, and clay). Type 1 consists of a puffy friable crust over sand and silt and is found on the lower Furnace Creek fan and below the gravel fans at the edge of the salt pan on both sides of the valley. Type 2 consists of dry smooth clay and silt with a thin skin of salt. These surfaces are the salt pan where salt deposits have been completely removed by erosion. Type 3 consists of silt and clay capping massive salt deposits as are found in the central area of Cotton Ball Basin. The high TI areas consist of surfaces which contain standing water such as Badwater Basin south of Devil's Golf Course, Middle Basin and southeast Cotton Ball Basin; moist surfaces often associated with seeps and springs or rainfall runoff; and massive deposits of rock salt without thick caps of silt or clay, especially where the water table is near the surface such as Devil's Golf Course. The alluvial fans display an intermediate TI which depends on the size of gravel, the degree of cementing of the finer material, and the extent of desert pavement (large rock fragments, cementing and desert pavement all raise the TI). The development of all these surfaces is intimately related to the past or present influence of water. The years during which this study was performed (1976-1979) were considerably wetter than average as measured by the rainfall record from Furnace Creek shown in Figure 32. Nevertheless, the valley's ground water sources, and the lower evaporation on the salt pan of salt solutions versus fresh water, combine to make water an important factor in determining the TI of the valley in all years. This is true despite the fact that the long-term average rainfall indicates Furnace Creek is one of the driest areas in the United States.

In this study we have demonstrated the ability to detect the presence of thin sheets of water over bright salt crusts using TI, when the albedo signature alone is insufficient due to the thinness of the overlying surface water and the high albedo of the underlying salt. Multispectral images can also be used to monitor water volume on playa surfaces as demonstrated by Krinsley (1974) for several playas in Iran. Combining multispectral and thermal measurements would provide a powerful means of identifying thin sheets of surface water and moist areas.

B. Mojave Desert - Trona

In our first HCMM report (Kahle et al., 1981), we evaluated the geologic mapping capabilities of the HCMM data for small areas. We extracted 35 by 35 km areas and analyzed them at a scale of 1:100,000. At this scale, the individual pixels were readily apparent, indicating that the usable enlargement factor of the data had been reached or exceeded. While important information relating to lithologic composition was interpretable from the data, the coarse pixel size of 500 meters is considerably less than desirable for geologic investigations of small areas. This suggested that a better use of these data may be for regional geologic mapping. Therefore we have undertaken to examine an area in Southern California at a scale of 1:250,000. This scale is the one used for the state geologic map series; each map covers an area of 1° of latitude and 2° of longitude, or approximately 100 by 200 km.

The area studied is covered by the Trona Sheet of the Geologic Map of California series (California Division of Mines and Geology, 1963), located in southeastern California (Figure 34); the area is bounded by latitudes 35° and 36°N, and longitudes 116° and 118°W.

Most of the area is in the Mojave Desert, bounded on the north by the Garlock fault; the northwestern corner falls in the Tehachapi Mountains, while the northeastern part lies in southern Death Valley. The Mojave Desert is characterized by isolated mountain masses surrounded by pediments; but large parts consist of alluvium within which there are several large and small playas. The Tehachapi Mountains are characterized by a relatively flat upland surface which is often considered to be the southern extension of the Sierra Nevada. Death Valley is characterized by north-trending mountain ranges and deep, relatively narrow, alluviated valleys, many of which have playas at their lowest elevations.

The geology of the Trona area is complex, reflecting a long history of tectonism. For this report, only the distribution of rock types is of interest. A summary of lithologies exposed in the area is shown in Table 8; a simplified geologic map is found in Figure 35. The state geologic map depicts units based on age and, in some cases, composition. Quaternary units are separated into dune sand, playa lake deposits, salt deposits, and alluvium. Marine sediments, on the other hand, are mapped on the basis of age, rather than rock type; this unit therefore includes limestone, dolomite, sandstone, shale, chert, wacke, and quartzite. In some cases, volcanic rocks are subdivided by lithology, in others they are undifferentiated. The units chosen for the simplified map in this report group similar general rock types, regardless of age; for example, the metamorphic rock unit includes Mesozoic and Precambrian rocks which are now gneisses, schists, metasediments, and metavolcanics.

<u>Processing and interpretation techniques</u>. HCMM data from multiple dates were processed for the Trona area. The day-night pairs were coregistered, then

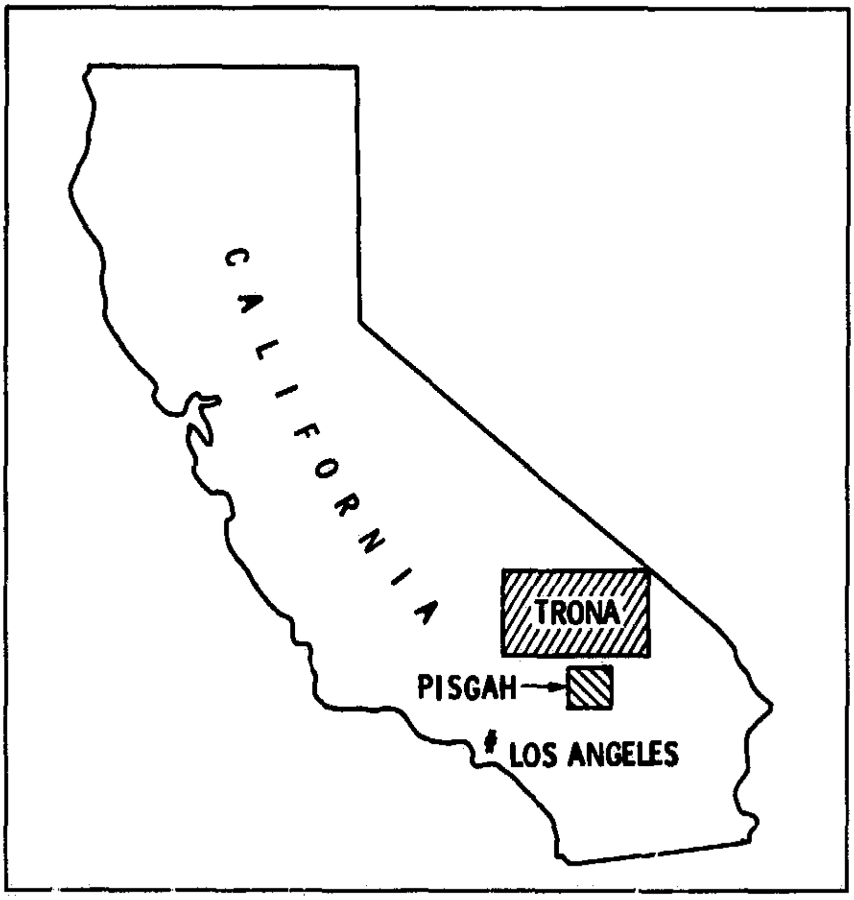

Figure 34. Location of Trona and Pisgah test areas in southern California.

Table 8

Geologic Units of Trona Area

Unit	Ages	Description
Alluvium	Quaternary	Alluvial fan deposits
Salt	Quaternary	Salt deposits on playas
Lake	Pleistocene-Quaternary	Playa deposits; mainly clay, silt, and salts
Sand	Quaternary	Dune sand
Nonmarine sediments	Tertiary	Older alluvium, sandstone, fanglomerate, conglomerate
Hypabyssal intrusives	Tertiary	Plutonic and intrusive rocks of rhyolitic, andesitic, and basaltic composition
Volcanics	Cenozoic, Mesozoic	Basalt, andesite, rhyolite extrusive rocks
Basic intrusive	Mesozoic	Diorite, gabbro, and amphibolite
Granite	Mesozoic	Granitic rocks ranging in composition from basic to acidic
Metamorphics	Mesozoic, Precambrian	Metasediments. metavolcanics, schists, gneisses
Marine sediments	Mesozoic, Paleozoic	Sandstone, shale, quartzite, limestone, dolomite

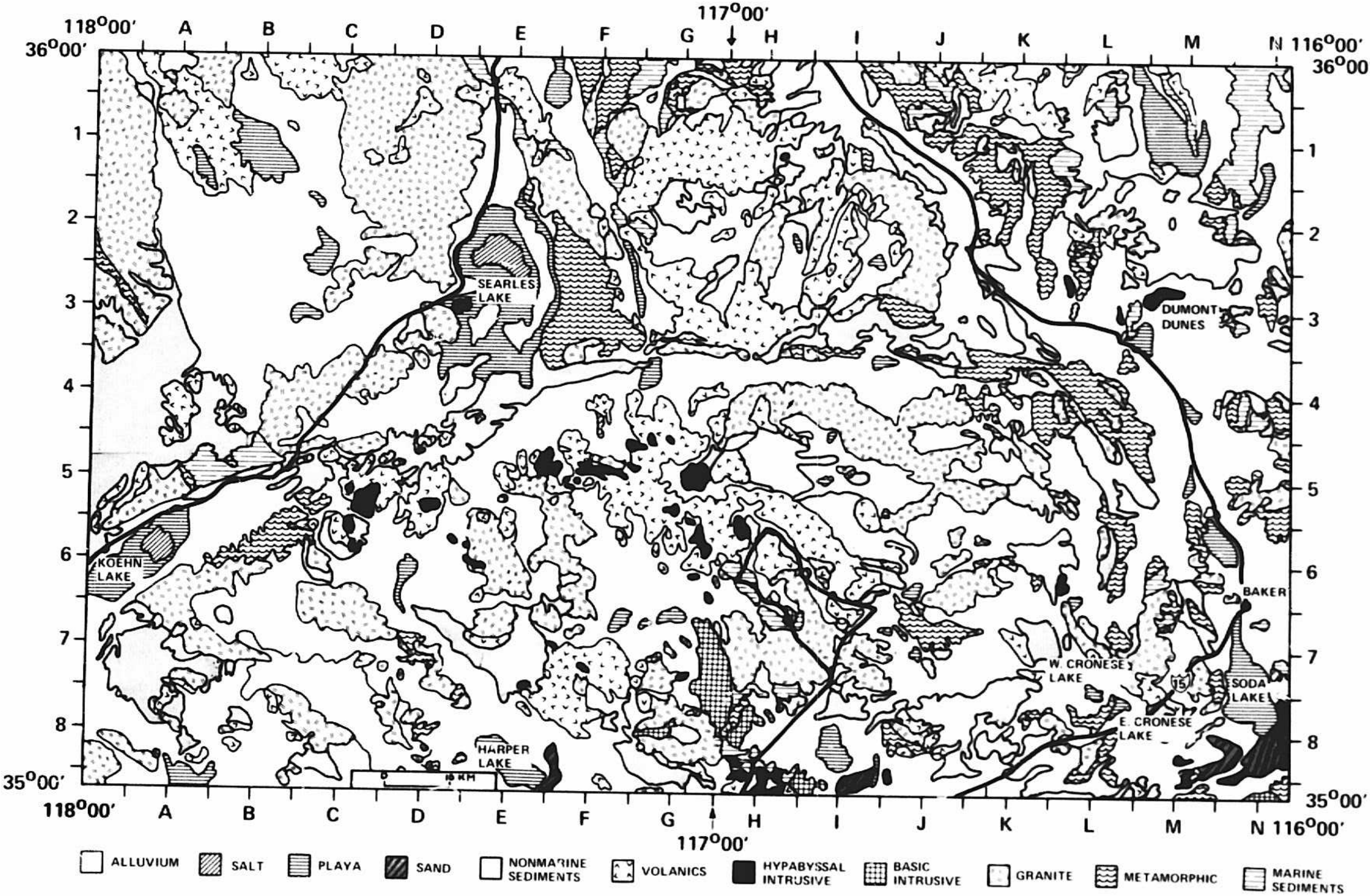

Figure 35. Simplified geologic map of Trona test area. (Modified from California Division of Mines and Geology, 1963.)

registered to a topographic base map. The day-night pairs, which consisted of the visible data, daytime infrared and nighttime infrared images, were examined on an interactive computer processing system to provide a suitable display for further evaluation. On this system we produced a color additive composite (CAC) for each day-night pair from the three images. This was done by displaying positive or negative images of the variables in blue, green, and red. After many combinations were examined, the May 30-31, 1978, day-night pair was selected for further analysis. A color composite was produced (Figure 36) by displaying the visible channel as red, the daytime infrared channel as blue, and the negative of the nighttime infrared channel as green. The data were also contrast stretched prior to production of the composite image. This compositing technique was described in our first HCMM report (Kahle et al., 1981). Strongly colored areas on the image are due to certain predictable combinations of physical properties: materials which have high albedo, high daytime temperature and/or low nighttime temperature will have strong red, blue and/or green color components. Playas, for example, which have high albedo and low thermal inertias, will be displayed with large red (high albedo), large green (cold at night), and small blue (cold during the day) color contributions. Playas thus appear yellow or orange in Figure 36.

A color print of this HCMM CAC image was produced at a scale of 1:250,000 to compare with the geologic map. Preliminary attempts to compare the two by physically overlaying one over the other proved unsatisfactory. Therefore, the geologic map was reproduced as a positive color transparency, which could be overlayed onto the HCMM image. This facilitated direct comparison of the two.

In the laboratory, the color variations in the HCMM CAC were systematically compared to the geologic map to determine which geologic units had consistent colors on the image, and which were displayed in different colors and were

ORIGINAL PAGE
COLOR PHOTOGRAPH

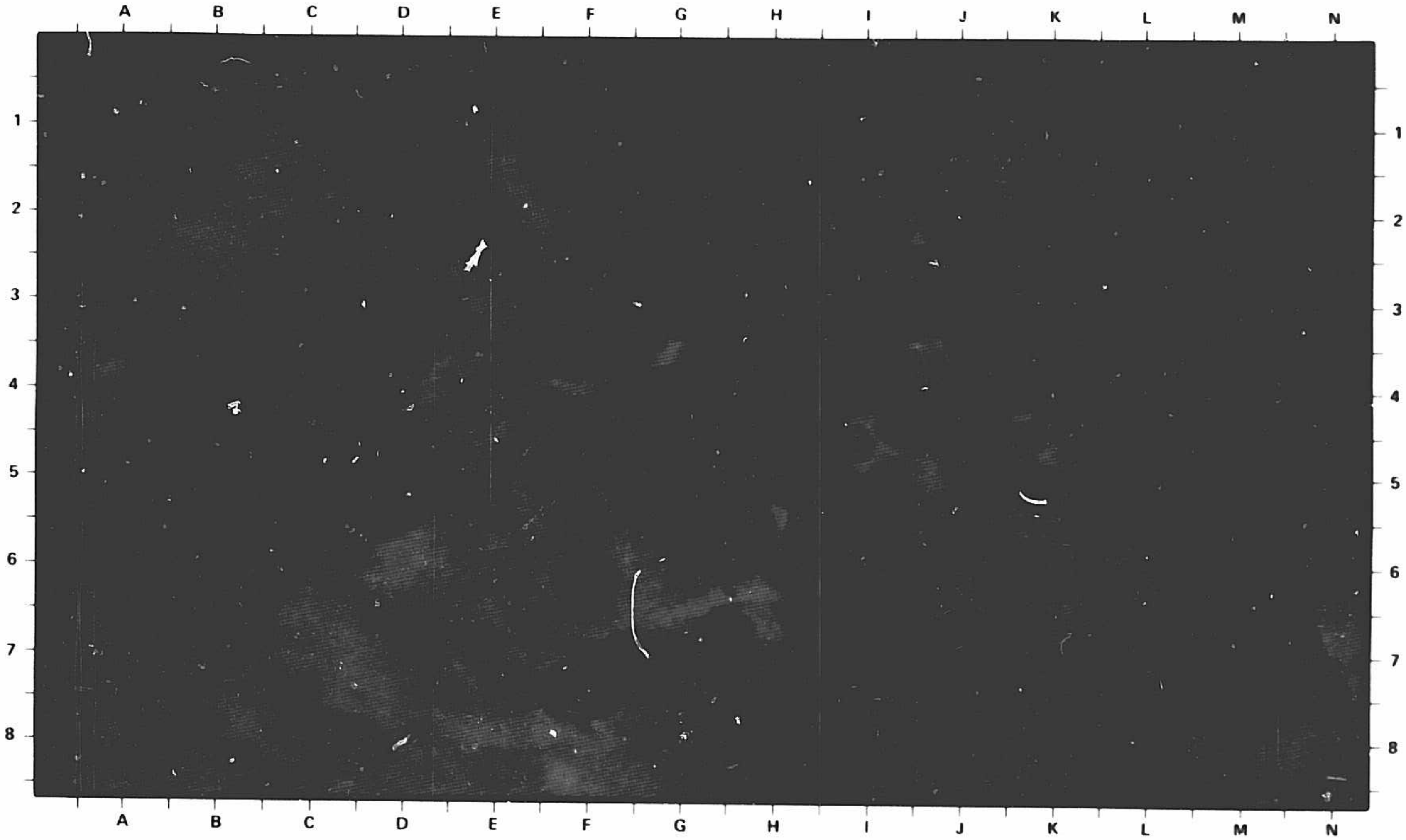

Figure 36. Color additive composite of May 30, 1978, HCMM data. The area covered is the same as the Trona geologic map (Figure 35). Visible, day infrared, and night infrared channels displayed as red, blue and green, respectively. The night infrared (green) channel is a negative: cold areas have large green contributions on the color image.

inconsistent. Those areas which seemed to be anomalous were delineated, and field investigations were undertaken in May, 1982, to examine the causes of their behavior.

Analysis and interpretation of data. Playas, or dry lakes, are common in the Trona test site. On the HCMM CAC image (Figure 36) most are displayed as yellow-orange. Examples include Coyote Lake (I-8), Silver Lake (M.5-5.5), Amargosa Lake (M-1), and West Cronese Lake (L-7.5). From the color, one can infer that the surfaces have high albedo (red component), low nighttime temperatures (green component), and low daytime temperatures (absence of blue). This is consistent with a composition of white clay/silt, which has a low TI. Several playas, however, appear distinctly different, in whole or in part. These include Soda Lake (N-7.5), Harper Lake (E-8.5), Searles Lake (E-2.5), Koehn Lake (A-6), and East Cronese Lake (L.5-7.5).

Soda Lake has a green crescent-shaped area at its south end (N-8). When this feature was examined in the field, a large corresponding area of very dense, one meter high dry bushes was found. The green color results from low albedo, low daytime temperature, and low nighttime temperature. Even though the ground under the vegetation is bright playa material, the bushes effectively shadow the ground and control the area's visible and thermal characteristics. The large green area at the west end of Koehn Lake (A-6) was found to be cultivated and highly vegetated. A similarly colored feature at the west end of Harper Lake (E-8) is assumed to have the same cause.

Searles Lake (E-2.5) appears to have a panoply of colors in the CAC. The perimeter is orange-yellow in color, similar to the other clay/silt playas. The geologic map shows a large elliptical area of salt deposits in the center of the playa. This correlates with the red area on the CAC. There is a smaller red area at the south end of the lake. A black patch and several blue-lavender areas within the playa can also be seen on the CAC. Examination in the field revealed that the black area corresponds to the lowest part of the playa, where standing water is often found. Black is produced by low albedo (little red), low daytime temperatures (little blue), and high nighttime temperatures (little green). These characteristics are consistent with the presence of standing water. Red color is produced by high albedo, low daytime temperatures, and high nighttime temperatures. The composition of the playa in this area is dominantly salt and silt. The material was found to be very bright, and moist just below the surface. The combination of higher density and moisture results in higher TI, producing the thermal variation seen on the CAC. The blue-lavender areas have moderate albedo, high daytime and nighttime temperatures. These areas in the field were composed of a light brown silt/clay surface with salt underneath, and are inferred to have been less moist.

East Cronese Lake (L.5-7.5) is dark red on the CAC. This is inferred to be due to lower albedo than West Cronese Lake (L-7.5), higher nighttime temperature, and about the same daytime temperature. In the field, both playas were found to be dry; however, their surfaces were distinctly different. The west playa was pale yellowish-brown with large polygonal cracking; the surface was undulating but smooth. The east lake was darker brown, with polygonal cracks extending to 30 cm depth; the surface had a popcorn texture with a frosting of salt. These field observations are inconsistent with the appearance on the CAC. Examination of the rainfall data for Death Valley for 1978 (Figure 32) indicates that a wet winter was followed by precipitation in May. In addition, the 15′ topographic map of the area shows that the Mojave River drains into East Cronese Lake. Water is prevented from flowing to West Cronese Lake by a drainage divide due to a spur of the Cronese Mountains. These two facts suggest that at the time of the HCMM data acquisition, standing water was present on East Cronese

Lake. The color on the CAC suggests that the water was quite shallow; the thermal variation is characteristic of water, but the moderate albedo suggests penetration and reflection of visible light from the lake bottom.

In the CAC image, rock outcrops were found to be displayed in a variety of colors: dark red, red, red-blue, dark blue, blue, dark green, green, dark orange, etc. Similarly colored areas were outlined from the CAC, then the outline map was superimposed on the geologic map to identify the units. Most of the red areas corresponded to granitic rocks (J-2, K.5-8, H.5-7, F-3); a few corresponded to marine sediments (N-4, M.5-1.5). The reverse comparison indicated that some areas mapped as granitic rocks appeared dark blue on the CAC (M-7, H.5-7.5); these areas were targeted for visiting in the field to determine the composition and characteristics of the materials responsible for the CAC colors.

Volcanic rocks appeared on the CAC as dark blue, blue, dark blue-green (F-7.5, E-5, H-3, A.5-1, for example) and dark orange (F-5). Basic intrusive rocks were dark green or blue (G.5-7); hypabyssal intrusive rocks were also dark green or blue (D-5.5, G.5-6).

Dune sands were not discernible on the HCMM image; nonmarine sediments were many different colors, reflecting the variety of compositions of the source rocks.

Metamorphic rocks were dark blue or green (M.5-7.5, J-6.5, for example). Large green areas on the CAC corresponded to mountain ranges with high elevations, such as the Avawatz Mountains (L-4.5) and the Argus Range (D-1). The green color indicated moderate to low albedo, cold daytime temperatures, and cold nighttime temperatures. This is consistent with the effects of lower temperatures as a function of increasing elevation, and the presence of substantial vegetation cover. These data were not corrected for the first effect, and the presence of vegetation would mask the underlying bedrock.

C-2

Field observations of granitic rocks at many locations revealed that those appearing red on the CAC were light colored, intermediate to acidic rocks; dark colored granitic rocks (really diorites, gabbros, etc.) were the ones appearing dark blue or red on the CAC. The same daytime and nighttime temperature behaviors combined with variable albedos (red component) to produce the different colors. Therefore, a useful feature of the HCMM data was the ability to subdivide mapped granitic rocks into mafic and felsic subunits.

Field examination of volcanic rocks indicated that blue areas on the CAC corresponded to outcrops of basalt; green and dark orange areas were pyroclastics, andesites, rhyolites, and tuffs. Basalt has very low albedo, high daytime temperatures and relatively high nighttime temperatures due to its high TI; these characteristics account for the blue color. The other volcanic rocks have higher albedos (rhyolites, K.5-.5, orange area) or lower thermal inertias (green areas). Therefore, the HCMM data provide some compositional information related to physical characteristics of the rock types.

A sharp boundary on the HCMM data was seen in the Owlshead Mountains (J-2.5), juxtaposing a red area to the north with a dark red-blue area to the south. The geologic map shows a contact between granitic rocks to the north and metamorphic rocks to the south. The HCMM boundary, however, is displaced 6 km to the south relative to the geologic map. In the field, the HCMM boundary was located from a distance and appeared to correlate with a sharp change in rock albedo. Access to the area was too difficult for us to examine the rock types; either the geologic map depicts the position of the boundary incorrectly, or a mafic facies of the granite at the south end produces an appearance similar to the metamorphic rocks on the CAC, so that the HCMM boundary is separating felsic granitic rocks from mafic granitic rocks and metamorphic rocks.

In summary, HCMM data from consecutive day-night passes were coregistered, then registered to a topographic base. An area corresponding to 1° by 2° was extracted, covering the Trona, California geologic map. The HCMM data were used to produce a color additive composite picture, using the visible, day infrared and night infrared data as the three color components. The color picture was enlarged to a scale of 1:250,000, and a photographic transparency of the geologic map was overlayed onto the HCMM image to evaluate the geologic separations interpretable from the HCMM image.

Playas were found to be displayed in a variety of colors. In all cases, the colors could be related to physical characteristics related to the playas' composition, moisture content, presence of standing water, and vegetation cover. Granitic rocks were depicted in two colors. Field work revealed that this division corresponded to differences in composition: felsic rocks could be distinguished from mafic rocks. This distinction was not portrayed on the state geologic map.

Volcanic rocks were displayed in a variety of colors, dependent on the albedo and thermal inertias of the materials. Basalts, for example, were distinguished by low albedo, high daytime temperature and high nighttime temperature; less dense pyroclastics and tuffs were distinguishable by their higher albedo, and lower daytime and nighttime temperatures.

Unconsolidated and consolidated Tertiary nonmarine sediments were not separable on the HCMM images from Recent alluvial fans, due to lack of contrasting physical properties. Similarly, areas of dune sands were not distinguishable; though in this case the coarse HCMM resolution (500 m) may have played a significant factor, as the dunes are quite small.

We found spatial resolution to be a major limiting characteristic of the HCMM data for regional geologic mapping. In the field it was often difficult or impossible to determine one's location accurately, particularly in areas of little topographic relief. At a scale of 1:250,000, the HCMM data could not be used to reproduce the detail shown on the state geologic map.

C. Pisgah

In Kahle et al. (1981) only a limited amount of work with the aircraft scanner data was done. This section presents some further results of processing and analysis of data over the Pisgah lava flow, Mojave Desert, California.

The area is located in southeastern California (Figure 34), in the arid, sparsely vegetated Mojave Desert province, 60 km east of the town of Barstow. The test site covers a 15 by 20 km region centered on the Quaternary Pisgah lava flows. Geologic units exposed in the area consist of Recent to Pleistocene alluvial fans, the Lavic Lake playa, Quaternary and late Tertiary basalt flows, a series of interbedded Tertiary volcanic and sedimentary rocks, and a dacite porphyry intrusive body.

Principal components analysis. Principal components analysis (PCA) has been used in statistical processing of data for a considerable time (Hotelling, 1933) and is well illustrated in many texts (Davis, 1973, for example). The method produces new variables (components) which are uncorrelated with each other and which are linear combinations of the original variables. The new axes for the variables are computed with the first axis or component containing the greatest proportion of the scene variance, followed by later components which contain successively less of the scene variance. In this fashion, it is often possible to ignore the later components because they contain little or no useful information to the analyst. Geometrically, a PCA can be viewed as a rotation and translation of the original coordinate axes to new axes passing through the data. PCA is also a method for reducing the dimensionality of data by removing intervariable correlation and compressing it onto new axes, usually less than the number of original data axes.

Data processing. For the Pisgah test site, aircraft multispectral scanner data acquired July 13-14, 1977, with NASA's Bendix 11-channel instrument (M^2S) were used. The data were acquired at an altitude of 9 km, with an instantaneous field of view of about 18 m. Ten channels of visible data and one daytime thermal infrared channel were acquired simultaneously near noon. The same area was reflown before sunrise, and only thermal data were obtained. These two data sets were coregistered, and a TI image was calculated using the Kahle model (Kahle et al., 1981). Twelve variables were selected for PCA analysis (Table 9); M^2S channel 7 was not used due to a limit of twelve variables in the computer program. Twelve components (eigenvectors) were output from the program, with weightings and percent of scene variance shown in Table 10. It can be seen that the first three components account for 99.2% of the scene variance, with the first component accounting for 94.8%.

Analysis of principal component images. The twelve eigenvector pictures (V1-V12) are shown in Figure 37. V1 is essentially an average of the visible and near-infrared channels, or albedo. The basalts are the darkest materials in the scene, the playa is the brightest. V2 is basically the difference between thermal inertia (TI) and day infrared (DIR). Bright areas are those with high thermal inertias and low daytime temperatures; these include the volcanic and sedimentary rocks in the northeast corner, and the dacite porphyry in the southwest corner.

V3 is heavily negatively weighted on channels 1, 2, DIR, and night infrared (NIR). Materials that have low reflectances and low temperatures in these channels will be bright on the image. These include playas, alluvial fans in the northern part of the area, and the dacite prophyry. It is surprising to

Table 9

Variables Used for Principal Components Analysis, Pisgah Test Site

Variable	Channel or value
1	M^2S 1, 0.38-0.44 µm
2	M^2S 2, 0.44-0.49
3	M^2S 3, 0.49-0.54
4	M^2S 4, 0.54-0.58
5	M^2S 5, 0.58-0.62
6	M^2S 6, 0.62-0.66
7	M^2S 8, 0.70-0.74
8	M^2S 9, 0.76-0.86
9	M^2S 10, 0.97-1.06
10	Day infrared, 8.05-13.7 µm
11	Night infrared, 8.05-13.7 µm
12	Thermal inertia

Table 10

Loadings for Eigenvectors, Pisgah Test Site

	M^2S Channel												
Component	1	2	3	4	5	6	8	9	10	DIR	NIR	TI	% of Variance
V1	0.30	0.36	0.33	0.28	0.28	0.31	0.36	0.36	0.38	0.01	-0.04	-0.16	94.8
V2	0.19	0.08	0.02	0.0	0.0	0.0	0.0	0.03	0.07	-0.64	0.11	0.73	3.0
V3	-0.72	-0.32	0.0	0.13	0.14	0.13	0.13	0.17	0.24	-0.32	-0.33	-0.04	1.4
V4	0.01	-0.29	-0.37	0.28	-0.13	0.0	0.17	0.26	0.57	0.25	0.42	0.13	0.4
V5	-0.40	0.03	0.28	0.29	0.22	0.14	0.02	-0.04	-0.28	0.28	0.63	0.27	0.2
V6	0.11	-0.16	-0.33	-0.18	0.13	0.35	0.52	0.23	-0.59	-0.06	0.01	0.01	0.1
V7	0.15	-0.17	-0.21	0.06	0.34	0.44	-0.02	-0.71	0.22	-0.11	0.08	-0.11	<0.1
V8	0.36	-0.61	-0.02	0.47	0.22	-0.06	-0.35	0.30	-0.08	0.06	-0.05	0.03	<0.1
V9	-0.02	0.04	-0.03	-0.01	0.07	0.14	0.04	-0.10	0.06	0.57	-0.54	0.58	<0.1
V10	0.24	-0.14	0.40	-0.41	-0.11	0.22	0.34	-0.60	0.33	-0.02	-0.02	-0.02	<0.1
V11	0.17	0.07	-0.29	0.58	-0.52	-0.15	0.46	-0.25	0.09	-0.01	0.0	0.0	<0.1
V12	0.11	-0.01	0.02	-0.13	0.45	-0.76	0.45	-0.01	-0.02	0.0	0.0	0.0	<0.1

Largest weightings underlined

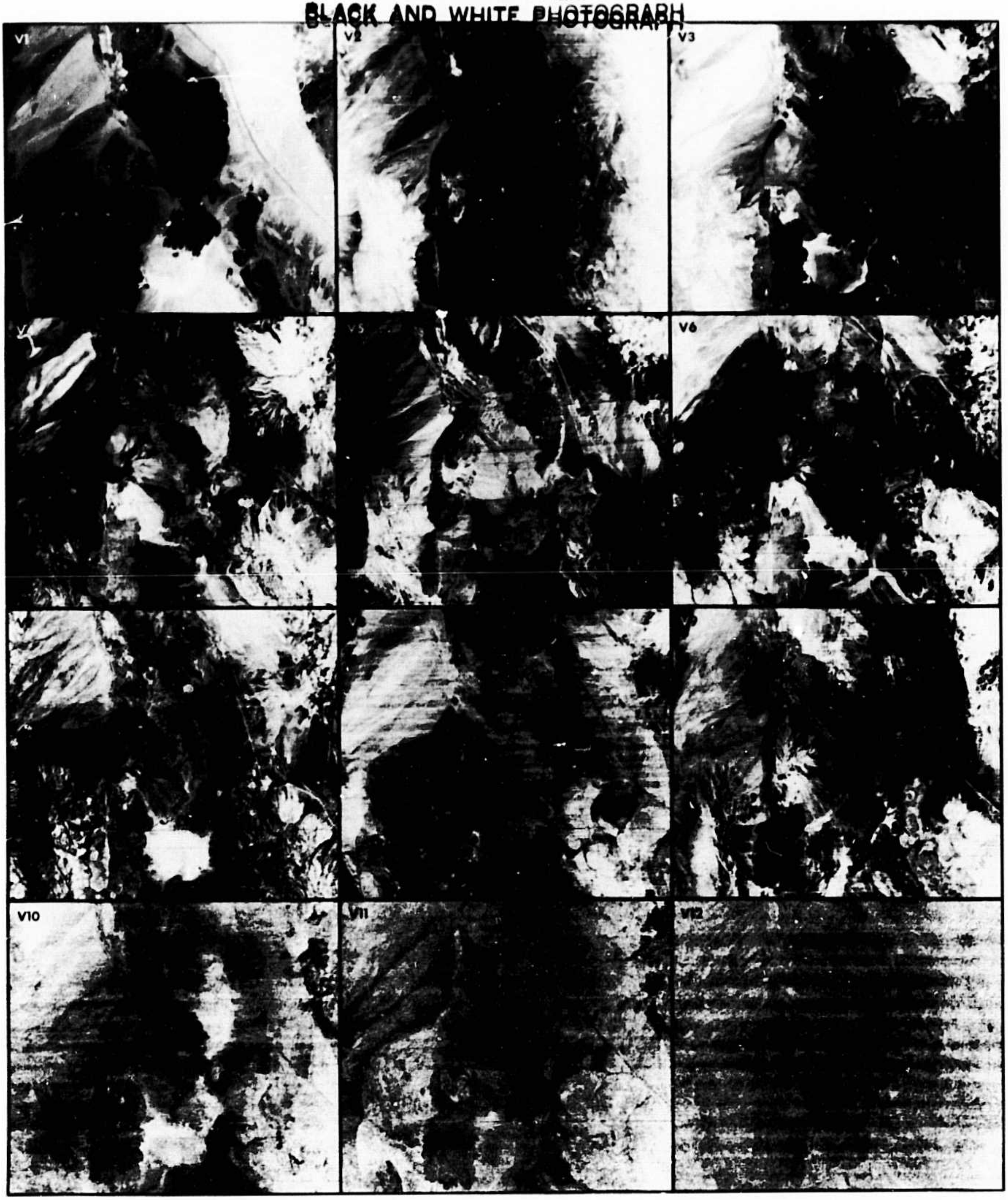

Figure 37. Twelve eigenvector pictures (principal components) of Pisgah test site computed from 11-channel M^2S multispectral scanner data and thermal inertia data. Data acquired July 13-14, 1977. Area covered is 17 by 19 km; direction of flight line is N28°W.

have a component weighted on both visible-near infrared channels and thermal channels. In the past, when we have tried PC analysis, the two data types fell almost entirely onto separate components. Probably the large areas of very dark rocks caused a high correlation between the thermal and reflectance channels. V4 is positively weighted on channel 10 and NIR, and negatively weighted on channel 3. On the Pisgah flows, aa has higher V4 values than pahoehoe. The small white dots on the pahoehoe surfaces are pockets of aeolian sand. The volcanic and sedimentary rocks on the eastern side of the area are all bright. V5 is strongly weighted on the NIR. Bright areas are those warmer at night. The dacite porphyry, and hydrothermally leached andesite porphyry in the upper right corner are two prominent areas which stand out. There is also good separation of the pahoehoe and aa flows. V9 is weighted positively on DIR and TI, negatively on NIR. Some topographic features are visible due to solar heating anisotropies, particularly in the dacite porphyry. V10, V11, and V12 have very little information and contain mostly noise.

Based on examination of the individual black-and-white component pictures, several triplets were selected to produce color composites. One of those is shown in Figure 38. This image displays V3, V6, and V7 as blue, green, and red, respectively.

The amount of geologic information displayed in this image greatly surpasses that interpreted from the HCMM data for the same area we described earlier (Kahle et al., 1981). In fact, more separations can be made from an analysis of this image than are shown even on the detailed 15′ published geologic map of the area (Dibblee, 1966). The Pisgah flows (see sketch map, Figure 39) are clearly separable into two subunits, corresponding to aa and pahoehoe; Pisgah Crater, composed of cinders, is a different color than the surrounding flows. The geologic map does not distinguish the two flow units.

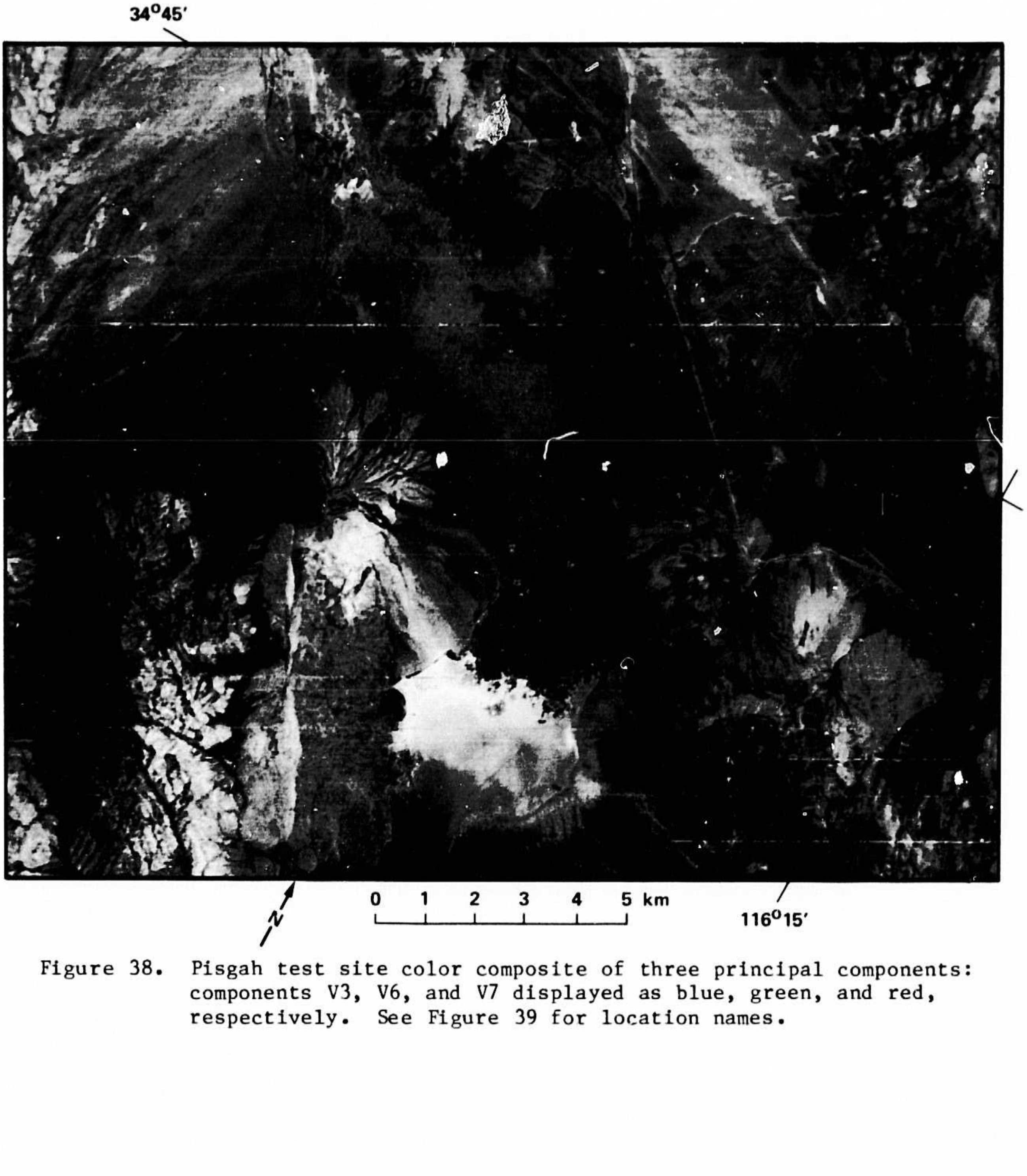

Figure 38. Pisgah test site color composite of three principal components: components V3, V6, and V7 displayed as blue, green, and red, respectively. See Figure 39 for location names.

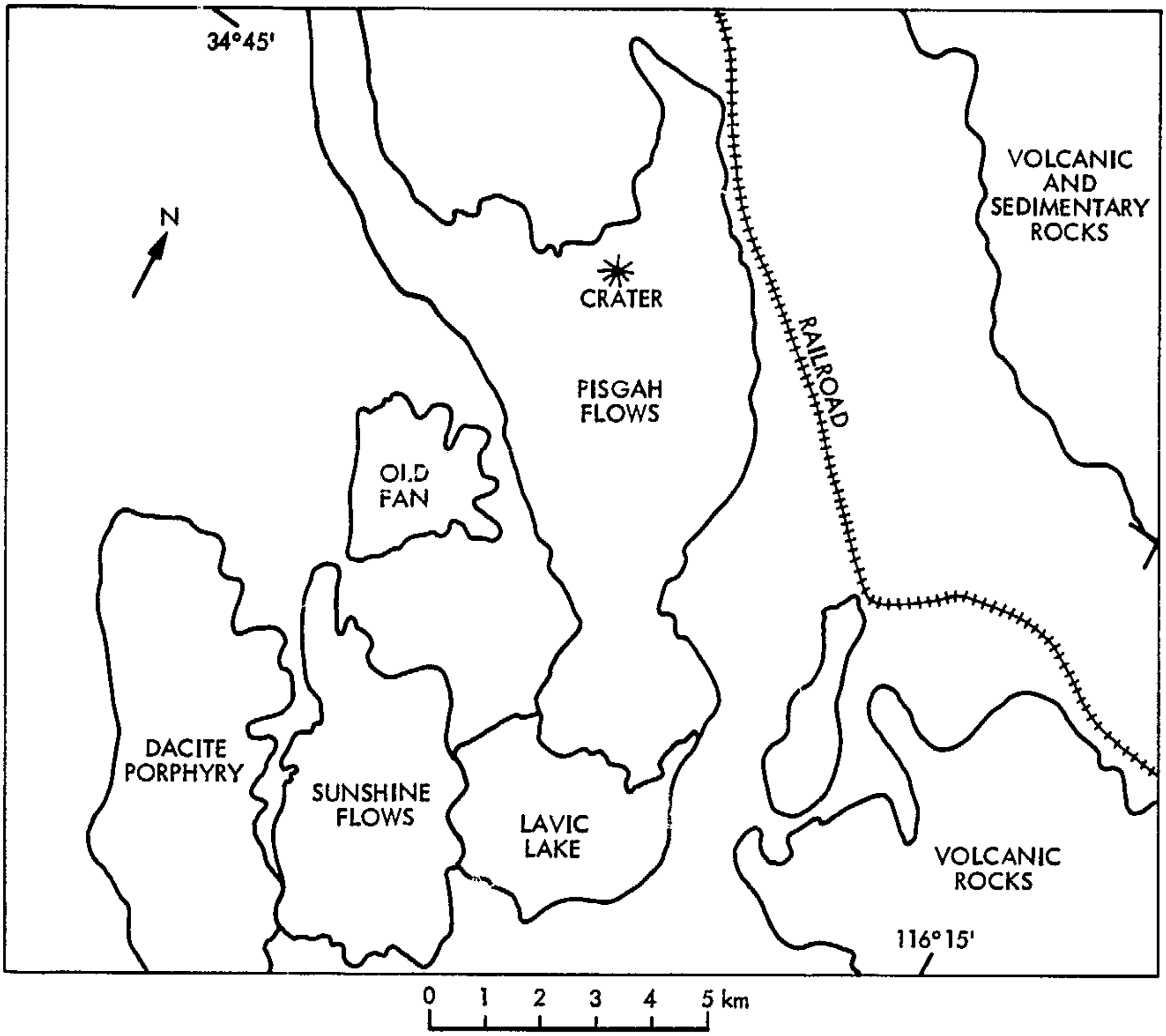

Figure 39. Sketch map of Pisgah test site, showing major features depicted in Figure 38.

The separation of units in the volcanic rocks (lower right corner), and volcanic and sedimentary rocks (upper right corner) is as good as that depicted on the geologic map. The varied colors of Lavic Lake (a clay playa) reflect differences in composition and moisture. The ability to portray these factors has important implications for engineering geology and hydrology (road planning, search for irrigation water, etc.). Finally, the vivid portrayal of alluvial fans, ranging in age from Recent to Pleistocene, would gladden the heart of Quaternary geomorphologists.

This improvement in mapping is attributed to two factors: the 40 times increase in IFOV from M^2S compared to HCMM data (12 m versus 500 m), and the merging of reflectance and thermal data. The technique of using principal components analysis is an effective method to combine disparate data sets (like reflectance and thermal data) when the data types are correlated. For totally uncorrelated data, this approach produces images which do not combine the original variables; instead, the variables reappear in their original form.

IV. SUMMARY AND CONCLUSIONS

We have directed much of the effort of the present study toward a more accurate determination of the values of TI derived from HCMM data. Sensitivity studies using our thermal models have indicated the size of errors that can be introduced into the calculation by errors in any of the numerous input variables. Some of the largest sources of error are effects due to partial vegetation cover and intermittent cloudiness. The most important effect, causing errors of as much as 10-15% in calculated TI, is due to the error introduced into the measurement of surface temperature if atmospheric transmission and emission are ignored. Surface topography also affects the calculation of TI through slope, slope azimuth, and elevation effects.

We have investigated the use of digital topographic information and atmospheric models to correct for some of these effects. The results are informative and do allow us to calculate much more realistic values of TI of surface materials. However, it is impossible to model and calculate some effects such as the local micrometeorology which is of importance in the sensible heat calculation. Microtopography, while shown to be important, would require "roughness" measurements or much better digital topography than is routinely available. In addition, the cost of the atmospheric and topographic corrections made here, while worthwhile for research purposes,would be prohibitive in any operational sense We suggest that apparent TI, with only simple atmospheric radiance corrections to the measured surface temperature, will be the preferred product for most operational requirements for surface TI. Calculations of more accurate TI values such as we have made here will be of value primarily in research problems.

The other aspect of our study was the further evaluation of HCMM and aircraft thermal data for geologic problems. We have found that at our test sites the thermal data does add information about the nature of the surface material that is not available in the visible and near-IR reflectance data. At Death Valley, areas of moisture and standing water were more easily and unambiguously delineated with the use of the thermal data. At Pisgah, using aircraft data, and in the larger Mojave Desert area using HCMM data, some rock units were found to be separable only when the thermal data were combined with visible data. These were typically units which had similar visible and near-infrared reflectance characteristics, yet had different thermal properties. Using these data, it was further demonstrated that color composites of daytime temperature, nighttime temperature, and albedo were often more useful than TI images alone for discrimination of lithologic boundaries. Granitic rocks could be separated into felsic and mafic rocks, several types of volcanic rocks were separable, and the colors of playas could be related to their physical properties, such as composition, moisture content, and the presence of standing water or vegetation.

Also, principal component analyses were found to be very useful in increasing the separability of units, particularly when multispectral visible and near-IR aircraft scanner data were used in combination with thermal data.

A modeling study indicated the feasibility of looking for geologic features buried under a meter or so of alluvial material, using the annual heating cycle. The spatial resolution of HCMM precluded using these data for a demonstration, but a promising field study is underway using aircraft thermal data.

At all test sites, the spatial resolution of HCMM data was the major limiting factor in the usefulness of the data. We feel that future thermal infrared satellite sensors need to provide spatial resolution comparable to that of the Landsat data. In a trade-off situation, this increased spatial resolution would be much more important for geologic studies than increased thermal resolution.

Our study of HCMM data has confirmed that thermal data add a new dimension to geologic remote sensing. We have concerned ourselves in this study only with the broadband thermal infrared data which leads to information about the thermal properties of the surface materials. Multispectral thermal infrared data provide a different type or information which is also useful. Both types of information could, in principle, be acquired from a single multispectral thermal infrared sensor. We strongly recommend that future satellite missions be undertaken to allow the continued development of the thermal infrared data for geology.

V. ACKNOWLEDGMENTS

Alan Gillespie and Helen Paley of JPL reviewed the draft version of this report, and contributed useful criticism to improve the quality.

VI. REFERENCES

Barnes, W. L. and J. C. Price, Calibration of a satellite infrared radiometer, *Applied Optics*, *19*, 13, pp. 2153-2161, 1980.

Bohse, J. R., M. Bewtra, and W. L. Barnes, Heat Capacity Mapping Radiometer (HCMR) data processing algorithm, calibration, and flight performance evaluation, *NASA Technical Memorandum 80258*, Goddard Space Flight Center, Greenbelt, Maryland, 162 pp., 1979.

Brunt, D., Notes on radiation in the atmosphere, *Quart. J. Roy. Meteorol. Soc.*, *58*, pp. 389-420, 1932.

California Division of Mines and Geology, Geologic Map of California, Trona Sheet, Sacramento, CA, 1963.

Davis, J., *Statistics and Data Analysis in Geology*, New York: John Wiley and Sons, 1973.

Dibblee, T., Geologic map of the Lavic Quadrangle, San Bernardino County, California, *Miscellaneous Geologic Investigations Map I-472*, U.S. Geological Survey, Washington, D.C., 1966.

Gillespie, A. R. and A. B. Kahle, The construction and interpretation of a digital thermal inertia image, *Photogrammetric Engineering and Remote Sensing*, *43*, 8, pp. 983-1000, August 1977.

Hotelling, M., Analysis of a complex of statistical variables into principal components, *J. Educ. Psych.*, *24*, pp. 417-441, 498-520, 1933.

Hummer-Miller, S., Estimation of surface temperature variations due to changes in sky and solar flux with elevation, *Geophysical Research Letters*, *8*, 6, pp. 595-598, June 1981.

Hunt, C. B., *Death Valley: Geology, Ecology, Archaeology*, University of California Press, Berkeley, 234 pp., 1975.

Hunt, C. B. and D. R. Mabey, Stratigraphy and Structure, Death Valley, California, U.S. Geological Survey Professional Paper 494-A, 162 pp., 1966.

Hunt, C. B., T. W. Robinson, W. A. Bowles, and A. L. Washburn, Hydrologic Basin, Death Valley, California, U.S. Geological Survey Professional Paper 494-B, 138 pp., 1966.

Jakosky, B., The effects of non-ideal surfaces on the derived thermal properties of Mars, Journal of Geophysical Research, 84, pp. 8252-8262, 1979.

Kahle, A. B., A simple thermal model of the earth's surface for geologic mapping by remote sensing, Journal of Geophysical Research, 82, 11, pp. 1673-1680, 1977.

Kahle, A. B., A. R. Gillespie, and A. F. H. Goetz, Thermal inertia imaging: a new geologic mapping tool, Geophys. Res. Lett., 3, pp. 26-28, January 1976.

Kahle, A. B., J. P. Schieldge, M. J. Abrams, R. E. Alley, and C. J. LeVine, Geologic applications of thermal inertia imaging using HCMM data, JPL Publication 81-55, Jet Propulsion Laboratory, Pasadena, CA, September 1981.

Kahle, A. B., J. P. Schieldge, and R. E. Alley, Sensitivity of thermal inertia calculations to variations in environmental factors, submitted to International Journal of Remote Sensing, 1983.

Kneizys, F. X., E. P. Shettle, W. O. Gallery, J. H. Chetwynd, Jr., L. W. Abreu, J. E. A. Selby, R. W. Fenn, and R. A. McClatchey, Atmospheric transmittance radiance: Computer code LOWTRAN 5, Rpt. #AFGL-TR-80-0067, Air Force Geophysics Laboratory, Hanscom AFB, MA, 1980.

Kondratyev, K. Ya, Radiation in the atmosphere, p. 562, Academic Press, NY, 1969.

Krinsley, D. B., The utilization of ERTS-1 generated images in the evaluation of some Iranian playas as sites for economic and engineering development, U.S. Geological Survey, Reston, Virginia, Part I, 41 pp., Part II, 73 pp, 1974.

Marsh, S. E., J. P. Schieldge, and A. B. Kahle, An instrument for measuring thermal inertia in the field, *Photogrammetric Engineering and Remote Sensing*, *48*, 4, pp. 605-607, April 1982.

Nash, D. B., Thermal remote sensing of faulted bedrock buried by alluvium, submitted to *Photogrammetric Engineering and Remote Sensing*, 1983.

National Oceanic and Atmospheric Administration, *Climatological Data, California*, *80-83*, January 1976 - December 1979.

Schieldge, J. P., A. B. Kahle, and R. E. Alley, A numerical simulation of soil temperature and moisture variations for a bare field, *Soil Science*, *133*, 4, pp. 197-207, April 1982.

Sellers, W., *Physical Climatology*, University of Chicago Press, Chicago, IL, 1965.

Swinbank, W. C., Long-wave radiation from clear skies, *Quart J. Roy. Meteorol. S[illegible]* *89*, pp. 339-348, 1963.

Wolfe, W. L. and G. J. Zissis, eds., *The Infrared Handbook*, Office of Naval Research, Department of the Navy, Washington, D.C., pp. 3-35, 3-37, 1978.